



ANALYTICAL SOLUTIONS OF SHALLOW-WATER WAVE EQUATIONS

A THESIS SUBMITTED TO  
THE GRADUATE SCHOOL OF NATURAL AND APPLIED SCIENCES  
OF  
MIDDLE EAST TECHNICAL UNIVERSITY

BY

BARAN AYDIN

IN PARTIAL FULFILLMENT OF THE REQUIREMENTS  
FOR  
THE DEGREE OF DOCTOR OF PHILOSOPHY  
IN  
ENGINEERING SCIENCES

JUNE 2011

Approval of the thesis:

**ANALYTICAL SOLUTIONS OF SHALLOW-WATER WAVE EQUATIONS**

submitted by **BARAN AYDIN** in partial fulfillment of the requirements for the degree of **Doctor of Philosophy in Engineering Sciences Department, Middle East Technical University** by,

Prof. Dr. Canan Özgen  
Dean, Graduate School of **Natural and Applied Sciences**

\_\_\_\_\_

Prof. Dr. Turgut Tokdemir  
Head of Department, **Engineering Sciences**

\_\_\_\_\_

Assoc. Prof. Dr. Utku Kânoğlu  
Supervisor, **Engineering Sciences Department, METU**

\_\_\_\_\_

**Examining Committee Members:**

Prof. Dr. Ayşen Ergin  
Civil Engineering Department, METU

\_\_\_\_\_

Assoc. Prof. Dr. Utku Kânoğlu  
Engineering Sciences Department, METU

\_\_\_\_\_

Assoc. Prof. Dr. Hakan I. Tarman  
Engineering Sciences Department, METU

\_\_\_\_\_

Prof. Dr. Ahmet C. Yalçiner  
Civil Engineering Department, METU

\_\_\_\_\_

Prof. Dr. Can E. Balas  
Civil Engineering Department, Gazi University

\_\_\_\_\_

**Date:**

\_\_\_\_\_

**I hereby declare that all information in this document has been obtained and presented in accordance with academic rules and ethical conduct. I also declare that, as required by these rules and conduct, I have fully cited and referenced all material and results that are not original to this work.**

Name, Last Name: BARAN AYDIN

Signature :

# ABSTRACT

## ANALYTICAL SOLUTIONS OF SHALLOW-WATER WAVE EQUATIONS

Aydın, Baran

Ph.D., Department of Engineering Sciences

Supervisor : Assoc. Prof. Dr. Utku Kânoğlu

June 2011, 94 pages

Analytical solutions for the linear and nonlinear shallow-water wave equations are developed for evolution and runup of tsunamis –long waves– over one- and two-dimensional bathymetries. In one-dimensional case, the nonlinear equations are solved for a plane beach using the hodograph transformation with eigenfunction expansion or integral transform methods under different initial conditions, i.e., earthquake-generated waves, wind set-down relaxation, and landslide-generated waves. In two-dimensional case, the linear shallow-water wave equation is solved for a flat ocean bottom for initial waves having finite-crest length. Analytical verification of source focusing is presented. The role of focusing in unexpectedly high tsunami runup observations for the 17 July 1998 Papua New Guinea and 17 July 2006 Java Island, Indonesia tsunamis are investigated. Analytical models developed here can serve as benchmark solutions for numerical studies.

Keywords: long waves, tsunamis, shallow-water wave equations, hodograph transformation, analytical solution, wave runup/rundown, tsunami focusing

# ÖZ

## SİĞ-SU DALGA DENKLEMLERİNİN ANALİTİK ÇÖZÜMLERİ

Aydın, Baran

Doktora, Mühendislik Bilimleri Bölümü

Tez Yöneticisi : Doç. Dr. Utku Kânoğlu

Haziran 2011, 94 sayfa

Sığ-su dalga denklemleri bir ve iki boyutta analitik olarak çözülmüştür. Bir boyutta, sabit eğimli deniz tabanı üzerinde, deprem, uzun ve dar bir körfezde rüzgarın etkisi ve deniz altı toprak kayması sonucu oluşan dalga hareketleri doğrusal olmayan denklemlerle, hodograf dönüşümü ve özfonksiyon açılımı ile integral dönüşüm yöntemleri kullanılarak elde edilmiştir. İki boyutta ise, doğrusal sığ-su dalga denklemi, sabit derinlikteki deniz tabanı üzerinde ana yayılım eksenine paralel olan eksen boyunca sonlu uzunluktaki ilk dalga için çözülmüştür. Tsunami odaklanması olayı analitik olarak gösterilmiş ve 17 Temmuz 1998 Papua Yeni Gine ile 17 Temmuz 2006 Java Adası (Endonezya) tsunamileri sırasında gözlemlenen beklenmedik büyüklükteki dalga tırmanmalarına olası etkisi araştırılmıştır. Geliştirilen analitik çözümler sayısal yöntemlerin doğrulanmasında kıstas problemler olarak kullanılabilecektir.

Anahtar Kelimeler: sığ-su dalgaları, tsunamiler, sığ-su dalga denklemleri, hodograf dönüşümü, analitik çözüm, dalga tırmanması, tsunami odaklanması

To my mother Nilüfer and my father Sait

*They offered me unconditional love and support, not only throughout the course of  
this thesis, but throughout whole my life...*

## ACKNOWLEDGMENTS

First and foremost, I offer my deepest gratitude to my supervisor, Assoc. Prof. Dr. Utku Kânoğlu, for his insight, guidance as well as his enthusiasm and patience throughout this study. He has been a continuous source of new ideas and a good mentor whenever I needed help and motivation.

I would like to thank the Progress Committee members, Assoc. Prof. Dr. Hakan I. Tarman and Prof. Dr. Ahmet C. Yalçiner, for the seminal discussions and for their encouragement throughout the course of this thesis. I would like to extend my thanks to the additional Examining Committee members, Prof. Dr. Ayşen Ergin and Prof. Dr. Can E. Balas, for the valuable comments and suggestions.

I would also like to thank Prof. Dr. Patrick Lynett of Texas A&M University (USA) for his collaboration during my research visit.

I express my appreciation to the great teachers, Yamin İldeş, Mesude Güney, and Prof. Dr. Varga Kalantarov, who made me love Mathematics more and more.

Many friends have been supportive during this long journey. In particular, I am grateful to Durmuş Yarımpabuç, Cihan Yıldırım, Eray Arslan, and Yeliz and Serkan Okur.

My parents, Nilüfer and Sait, and my brothers, Barış and Behzat: you always believed in me and you made available your support in every way. This thesis would not have been possible without your support. Thank you all...

Last but not the least, my wife, Sibel: we have met three years ago and since then I always kept saying you “I am graduating at the end of this semester.” We had to wait so long until that semester could come. Now, finally, I am on the way to Antalya, where you are waiting for me. Thank you for your love and patience...

This study is financially supported by the State Planning Organization with grant no. BAP-08-11-DPT2002K120510.



## TABLE OF CONTENTS

ABSTRACT . . . . .	iv
ÖZ . . . . .	v
ACKNOWLEDGMENTS . . . . .	vii
TABLE OF CONTENTS . . . . .	viii
LIST OF TABLES . . . . .	x
LIST OF FIGURES . . . . .	xi
CHAPTERS	
1 INTRODUCTION . . . . .	1
2 AN INITIAL-BOUNDARY VALUE PROBLEM FOR THE NON- LINEAR SHALLOW-WATER WAVE EQUATIONS . . . . .	14
2.1 Mathematical Formulation . . . . .	15
2.2 Applications . . . . .	20
2.2.1 Gaussian wave . . . . .	20
2.2.2 Solitary wave . . . . .	28
2.2.3 Isosceles $N$ -wave . . . . .	28
2.2.4 Generalized $N$ -wave . . . . .	29
2.2.5 Application to near-shore earthquakes . . . . .	31
2.3 Conclusions . . . . .	32
3 WIND SET-DOWN RELAXATION . . . . .	37
3.1 Mathematical Model . . . . .	38
3.1.1 The steady-state phase . . . . .	38
3.1.2 Wind set-down relaxation . . . . .	41
3.2 Results and Discussions . . . . .	44

3.3	Conclusions . . . . .	45
4	PROPAGATION OF A FINITE SOURCE OVER A FLAT BASIN . .	49
4.1	General Analytical Solution . . . . .	51
4.2	Solution for Finite-crested Initial Waves . . . . .	54
4.3	Results and Discussions . . . . .	56
4.3.1	Comparison with Carrier and Yeh (2005) solution .	56
4.3.2	Propagation of an $N$ -wave over a constant depth . .	59
4.3.3	The 17 July 1998 Papua New Guinea Tsunami . .	63
4.3.4	The 17 July 2006 Java Island Tsunami . . . . .	67
4.4	Conclusions . . . . .	72
5	CONCLUSIONS . . . . .	75
	REFERENCES . . . . .	77
	APPENDICES	
A	FOURIER TRANSFORM OF THE FUNCTION $\tanh$ . . . . .	84
B	AN APPROXIMATE SOLUTION FOR THE FORCED NONLIN- EAR SHALLOW-WATER WAVE EQUATIONS . . . . .	85
B.1	Mathematical Analysis . . . . .	85
B.2	Results and Discussions . . . . .	90
B.3	Conclusions . . . . .	91
VITA	. . . . .	92

## LIST OF TABLES

### TABLES

Table 2.1	The corresponding parameters for the initial wave profiles presented in Eqs. (2.25) and (2.27) as in Carrier et al. (2003). The extreme wave height values –maximum runup and minimum rundown– for the cases with/without initial velocity are also tabulated. The exact initial velocity relation is considered in the calculations. . . . .	21
Table 2.2	The corresponding parameters of Eqs. (2.32), (2.34), and (2.36) for which calculations are performed. The extreme wave height values for the cases with/without initial velocity are also tabulated. The exact initial velocity relation is considered in the calculations. . . . .	31
Table 2.3	The corresponding parameters of Eq. (2.38) for which calculations are performed. The parameter set is taken from Tinti and Tonini (2005). . .	32

# LIST OF FIGURES

## FIGURES

- Figure 1.1 Definition sketch for the so-called canonical bathymetry (not to scale). The bathymetry consists of a plane beach connected to a constant depth basin. . . . . 5
- Figure 2.1 Definition sketch (not to scale). The variables with tilde show dimensional quantities. . . . . 15
- Figure 2.2 The initial wave profiles suggested by Carrier et al. (2003). (a) and (b) show the positive and negative Gaussian initial waves defined by Eq. (2.25) while (c) and (d) show the leading depression  $N$ -wave initial profile defined by Eq. (2.27) given for two different sets of parameters. The respective wave parameters are tabulated in Table 2.1. . . . . 22
- Figure 2.3 Time variations of (a) – (d) the shoreline positions  $\eta_s$ , and (e) – (h) the shoreline velocities  $u_s$  for the initial waves given in Figure 2.2. Dashed and solid lines represent the present solution with and without initial velocity, respectively, while dots represent results of Kânoğlu (2004) without velocity. The initial wave parameters and the maximum runoff/minimum rundown heights are tabulated in Table 2.1. . . . . 24
- Figure 2.4 Comparison of the variation of (a) – (d) the shoreline wave heights, and (e) – (h) the shoreline wave velocities for the three different initial velocity relations. Solid lines represent results for the exact nonlinear value, Eq. (2.29), while dots and dashed lines stand for the results of the linear and the asymptotic velocity approximations, i.e., Eqs. (2.30) and (2.31), respectively. The initial wave parameters are presented in Table 2.1. 25

Figure 2.5 Spatial variations of the free-surface elevation of the Gaussian wave given in the case 1 of Table 2.1 (Figure 2.2(a)). Dashed and solid lines represent the solution with and without initial velocity, respectively, and thick lines represent the linearly sloping beach. In the absence of initial velocity, splitted wave propagates away from the shore as seen, for example, in inset (b). The seaward boundary is at  $X_L = 50$  so that the reflected wave does not reach the shoreline. . . . . 26

Figure 2.6 Continued from Figure 2.5. . . . . 27

Figure 2.7 (a) The solitary wave with initial height  $H = 0.03$  located at  $x_1 = 30$ ; (b) the associated initial velocity distribution,  $u_0(x)$ . The corresponding temporal variations of the shoreline wave height  $\eta_s$  and the shoreline wave velocity  $u_s$  are presented in insets (c) and (d), respectively. Solid and dashed lines represent the cases  $u_0(x) \equiv 0$  and  $u_0(x) = 2\sqrt{x} - 2\sqrt{x + \eta_0(x)}$ , respectively. . . . . 29

Figure 2.8 (a) The isosceles  $N$ -wave profile with  $H = 0.03$  and  $x_1 = 30$ ; (b) the associated initial velocity distribution,  $u_0(x)$ . The corresponding temporal variations of the shoreline wave height  $\eta_s$  and the shoreline wave velocity  $u_s$  are presented in insets (e) and (f), respectively. (c) The generalized  $N$ -wave profile with  $H = 0.06$ ,  $x_1 = 30$ , and  $x_2 = 29$ . The scaling parameter is chosen as  $\varepsilon = 0.1827$  so that the wave has a maximum initial height of 0.03. (d) The associated initial velocity distribution,  $u_0(x)$ . The corresponding temporal variations for  $\eta_s$  and  $u_s$  are presented in insets (g) and (h), respectively. Solid and dashed lines represent the cases  $u_0(x) \equiv 0$  and  $u_0(x) = 2\sqrt{x} - 2\sqrt{x + \eta_0(x)}$ , respectively. . . . . 30

Figure 2.9 (a)-(f) Spatial variations of wave height for the case 1 of Tinti and Tonini (2005) at times  $\tilde{t} = 0, 1, 3, 4, 6$ , and 10 minutes. (g) Time variations of the shoreline position (solid line) and shoreline velocity (dashed line). Markers represent results of Tinti and Tonini (2005). Dimensional quantities are calculated and plotted using a characteristic length of  $l^* = 50 \text{ km}$  and a beach slope of  $\tan\beta = 1/25$  as in Tinti and Tonini (2005), so that the characteristic depth becomes  $l^* \tan\beta = 2000 \text{ m}$ . . . . . 33

Figure 2.10 (a)-(f) Spatial variations of wave height for the case 2 of Tinti and Tonini (2005) at times $\tilde{t} = 0, 1, 2, 4, 6$ , and 10 minutes. (g) Time variations of the shoreline position (solid line) and shoreline velocity (dashed line). Markers represent results of Tinti and Tonini (2005). Dimensional quantities are calculated and plotted using a characteristic length of $l^* = 50 \text{ km}$ and a beach slope of $\tan\beta = 1/25$ as in Tinti and Tonini (2005), so that the characteristic depth becomes $l^* \tan\beta = 2000 \text{ m}$ . . . . .	34
Figure 2.11 (a)-(f) Spatial variations of wave height for the case 3 of Tinti and Tonini (2005) at times $\tilde{t} = 0, 1, 2, 4, 6$ , and 10 minutes. (g) Time variations of the shoreline position (solid line) and shoreline velocity (dashed line). Markers represent results of Tinti and Tonini (2005). Dimensional quantities are calculated and plotted using a characteristic length of $l^* = 50 \text{ km}$ and a beach slope of $\tan\beta = 1/25$ as in Tinti and Tonini (2005), so that the characteristic depth becomes $l^* \tan\beta = 2000 \text{ m}$ . . . . .	35
Figure 2.12 (a)-(f) Spatial variations of wave height for the case 4 of Tinti and Tonini (2005) at times $\tilde{t} = 0, 1, 2, 3, 6$ , and 10 minutes. (g) Time variations of the shoreline position (solid line) and shoreline velocity (dashed line). Markers represent results of Tinti and Tonini (2005). Dimensional quantities are calculated and plotted using a characteristic length of $l^* = 50 \text{ km}$ and a beach slope of $\tan\beta = 1/25$ as in Tinti and Tonini (2005), so that the characteristic depth becomes $l^* \tan\beta = 2000 \text{ m}$ . . . . .	36
Figure 3.1 Definition sketch for a long-narrow ( $\tilde{W}/\tilde{L} \ll 1$ ) and shallow ( $\tilde{D}/\tilde{L} \ll 1$ ) basin: (a) cross section, (b) top view. . . . .	39
Figure 3.2 The steady-state wind set-down solution for $\gamma = 0.01$ . . . . .	41
Figure 3.3 Spatial variations of the free-surface elevation and the velocity for $\gamma = 0.01$ at times $t^* = 0, 10, 40$ . . . . .	46
Figure 3.4 (a) Temporal variation and (b) power spectral density of the shoreline position $x_s$ for $\gamma = 0.01$ . Note that $x_s = -\eta_s$ . Insets (a) and (b) correspond to the Figures 3 and 4 of Gelb et al. (1997), respectively. . . .	47
Figure 4.1 Definition sketch (not to scale): two-dimensional view (left inset) and top view (right inset). . . . .	53

Figure 4.2 (a) The Gaussian hump defined by Eq. (4.25). (b) Evolution of the Gaussian hump at times  $t = 0.5, 1, 2, 5, 10, 20, 30, 40$ , and  $50$ . The self-similarity ( $t \sim r$ ) of the solution (4.35) can be observed for  $t > 5$ . . . . . 59

Figure 4.3 Temporal variations of the water surface elevation of the elongated Gaussian source, Eq. (4.30), with crest length  $L = 20$  are evaluated through Eq. (4.37) at distances  $r = 20, 60$ , and  $100$  along the directions (a)  $\theta = 0^\circ$ , (b)  $\theta = 45^\circ$ , and (c)  $\theta = 90^\circ$ . Solid lines show the present analytical solution while dots show Carrier and Yeh (2005)'s solution. The initial source Eq. (4.30) is located at  $(x_0, y_0) = (-L/2, 0)$  to have one-to-one comparison with the Figure 7 of Carrier and Yeh (2005). . . . . 60

Figure 4.4 Time histories of the water surface elevation are evaluated through Eq. (4.37) for different source lengths ( $L = 10, 20, 40$ , and  $60$ ) along the directions normal ( $\theta = 0^\circ$ ) and parallel ( $\theta = 90^\circ$ ) to the major axis ( $x$ -axis) of the source. The source is initially located at  $(x_0, y_0) = (0, 0)$  and the water surface variations are recorded at the distance  $r = 100$ . This figure is a reproduction of the Figure 8 of Carrier and Yeh (2005). . . . . 61

Figure 4.5 Propagation of a plus-minus source over a constant ocean basin showing focusing. (Lower right inset) Overall maximum amplitude for each grid point having extreme maximum wave height (focusing point) on the leading depression side of the propagation (Moore, personal communication). . . . . 62

Figure 4.6 Evolution of the PNG wave over a constant depth at (a)  $t = 0$ , (b)  $t = 2$ , (c)  $t = 5$ , and (d)  $t = 15$ . PNG initial wave is defined as  $\eta_n(x, y) = f(x)g_n(y) = \frac{1}{2}\varepsilon H[\tanh \gamma_n(x-x_0)-\tanh \gamma_n(x-(x_0+L))](y-y_2)\text{sech}^2 \gamma_n(y-y_1)$  with parameters  $H = 0.01$ ,  $p_0 = 15$ ,  $L = 1$ ,  $\gamma_n = 0.34$ ,  $y_1 = 50$ ,  $y_2 = y_1 + 0.2 = 50.2$ ,  $x_0 = 49.5$ , and  $\varepsilon = 4.93$ . (e) Overall maximum wave height at each grid point computed through the numerical model MOST (from Kânoğlu et al., in preparation). . . . . 64

Figure 4.7 Two-dimensional  $N$ -wave surface profile  $\eta_n(x, y) = f(x)g_n(y)$  (solid line) is compared with one-dimensional  $N$ -wave defined by  $\eta_n(y) = \epsilon H (y - y_2) \operatorname{sech}^2 \gamma_n (y - y_1)$  (dashed line) at (a)  $t = 0$ , (b)  $t = 2$ , (c)  $t = 5$ , and (d)  $t = 15$ . Note that the slice of the two-dimensional surface is plotted along the bisector line in  $x$ -direction. The scaling parameter  $\epsilon$  for one dimensional  $N$ -wave is  $\epsilon = 0.82$ . Refer to the caption of Figure 4.6 for the other parameters. . . . . 65

Figure 4.8 Spatial variations of water surface elevations (solid line) are plotted at (a)  $t = 0$ , (b)  $t = 5$ , (c)  $t = 25$ , and (d)  $t = 40$  including maximum wave height envelope (dash-dotted line). The dashed line in inset (a) is the initial wave profile with steepness  $p_0 = 5$ . Refer to the caption of Figure 4.6 for the other parameters. . . . . 66

Figure 4.9 The effect of (a) the source length ( $L$ ), (b) the wave steepness ( $p_0$ ) on the location of the focusing point for the PNG initial wave. The maximum wave heights are recorded along the bisector line, i.e., line perpendicular to the source strip. The steepness parameter is  $p_0 = 15$  for inset (a) and the source length is  $L = 1$  for inset (b). Parameters other than  $p_0$  and  $L$  are the same as in the caption of Figure 4.6. . . . . 68

Figure 4.10 (a) Maximum wave amplitude variations along different directions ( $\beta$ -lines) are plotted over a distance  $r$  from the nondimensional point  $(x, y) = (50, 52.5)$ , which is the approximate location of the PNG initial source proposed by Synolakis et al. (2002). The nondimensional wave height  $H = 0.01$  corresponds to a dimensional 16 m for the reference depth  $d = 1600$  m. (b) The maximum wave amplitudes along each  $\beta$ -line (black dots) are plotted on the contours of the PNG initial source. The  $r = 25$  km radius circle shows the approximate location of the Sissano area over the  $\beta = 45^\circ$  line. Triangles show the maximum wave amplitude locations for the initial wave with  $p_0 = 5$ , which is plotted in Figure 4.8(a). (c) Three-dimensional view of the maximum wave amplitude variation of the PNG source along different directions  $\beta$ . Refer to the caption of Figure 4.6 for the parameters. . . . . 69



Figure 4.11 Reverse tsunami travel time (RTTT) contours are shown for Per- misan (red filled square; Spillane, personal communication). Magenta grid represents the NCTR's $100\text{ km} \times 50\text{ km}$ unit sources. Considering tsunami travel time and focusing, the source configuration including three unit sources (red rectangles) are proposed as a possible source mecha- nism of the 17 July 2006 Java tsunami (Moore, personal communication). Black rectangle is the USGS source for the event. Red dot shows the earthquake epicenter location. . . . .	71
Figure 4.12 Propagation of the proposed source of the Java event (Figure 4.11) over a constant depth using the numerical model MOST at times (a) $t =$ 10.6 minute, (b) $t = 13.8$ minute, and (c) $t = 17.0$ minute. (d) Overall maximum amplitude for each grid point (from Kânoğlu et al., in prepara- tion). . . . .	72
Figure 4.13 Propagation of the proposed source over the real bathymetry off Java, Indonesia. Maximum wave amplitude contours for the propagation over the constant depth are also incorporated to point out potentially dan- gerous locations because of focusing (from Kânoğlu et al., in preparation).	73
Figure B.1 Definition sketch. The undisturbed water depth is defined to be $h_0(x) = x \tan \beta / \mu$ and the time-dependent bottom perturbation is repre- sented by $h(x, t)$ . . . . .	86
Figure B.2 Spatial distribution of the free-surface for $\beta = 10^\circ$ , $\mu = 0.05$ , ( $\tan \beta / \mu = 3.53$ ). Solid lines show the approximate nonlinear model re- sults while dashed lines show the linear analytical solution of Liu et al. (2003). Black and gray regions represent the sliding mass and the sloping beach, respectively, and dots represent the undisturbed water level. . . . .	90

# CHAPTER 1

## INTRODUCTION

Long waves, also known as shallow-water waves, are sea surface gravity waves which propagate over the sea with the wavelength  $L$  much larger than the depth of the sea  $d$ , i.e.,  $L \gg d$ . Typical example of long waves are tsunamis.<sup>1</sup> A tsunami is a sequence of waves formed on an ocean surface usually after sudden geophysical disturbances such as underwater earthquakes, submarine or subaerial landslides. Even though they are rare, volcanic eruptions or meteoroid impacts might also cause tsunami. The waves usually travel over long distances, and as they reach the target coast, their wavelength gets smaller and their height increases. When they run up over a shore, they mostly result in heavy damage on coastal structures and human casualties.

The deadliest tsunami event in recorded history is the 26 December 2004 Indian Ocean tsunami. After a  $M_w$  9.3 (Stein and Okal, 2005) earthquake occurred at 00:58 UTC with epicenter 250 *km* south-southeast of Banda Aceh, Sumatra, Indonesia, and hypocenter at a depth of approximately 30 *km*, the resulting tsunami inundated fourteen countries across the Indian Ocean with waves reaching as far as 2 *km* inland in some places. The maximum local runup was reported to be as high as 30 *m*. The number of fatalities is reported to be more than 228,000 and the economic impact of the natural hazard is estimated as 10 billion US dollars (Bernard and Robinson, 2009).

The most recent destructive tsunami hit the north east coasts of Japan on 11 March 2011 after a  $M_w$  9.0 earthquake occurred at 05:46 UTC with epicenter location 130 *km* east of Sendai, Honshu, Japan and hypocenter at an underwater depth of approxi-

---

<sup>1</sup> Tsunami is a Japanese word meaning harbor (tsu) wave (nami).

mately 32 *km*. It was the most powerful earthquake to have hit Japan, damaging or destroying over 125,000 buildings. Although Japanese people are well-educated against earthquake and tsunami disasters, there has been more than 15,000 victims, more than 5,000 people are injured and 8,000 more are reported to be missing by the end of May 2011. Moreover, the tsunami caused nuclear disaster. The cooling system of the Fukushima I Nuclear Power Plant, which is established in the towns of Okuma and Futaba of Fukushima Prefecture, is heavily damaged during the earthquake and tsunami. Consequently, residents within a 20 *km* radius of the power plant were evacuated and more than four million households in northeastern Japan were left without electricity. The total economical impact of the 2011 Tohoku earthquake and tsunami is estimated to raise up to 300 billion US dollars.

A tsunami can be analyzed in three main phases: generation, propagation, and runup (inundation). The generation phase describes the ocean surface response of the parent geophysical activity. Classification of historically recorded tsunamis over the source type by Gusiakov (2009) suggests that 75% of them are tectonic, i.e., earthquake-generated tsunamis. The second most frequent source of tsunamis with 10% share is submarine/subaerial landslides. Other rare sources of tsunamis (3%) are subaerial slides resulting from volcanic eruptions and meteoroid impacts (Gusiakov, 2009).

While major tsunamis are produced by large shallow-focus earthquakes (having magnitude greater than 7 on the Richter scale and depth less than 30 *km* in the earth), a submarine landslide triggered by a smaller earthquake can also generate a destructive tsunami, which was the case for the 17 July 1998 Papua New Guinea event (Synolakis et al., 2002; Bernard and Robinson, 2009).

Tectonic and landslide-generated tsunamis have different generation mechanisms. Since rupture velocity of earthquakes is much greater than the wave velocity in water, the common practice in most modeling for tectonic tsunamis is to directly translate the shape of bottom deformation to the ocean surface as an initial wave profile. This approach is often referred to as the passive generation mechanism. In case of underwater landslides, on the other hand, the time scale of the bottom dislocation should be taken into account as the velocity of the sliding mass is comparable with the wave velocity in water (Todorovska and Trifunac, 2001; Trifunac and Todorovska, 2002);

the resulting generation model is now referred to as the active generation mechanism. Comparisons of the two generation approaches are presented in several studies in connection with linear and nonlinear long wave propagation models (Dutykh and Dias, 2007; Kervella et al., 2007).

Source models for tectonic tsunamis are studied extensively. Dutykh and Dias (2007) reviewed the subject including dislocations in an entire elastic space (Volterra's dislocation theory) and elastic half-space (the so-called Okada's solution; Okada, 1985), and deformations by rectangular and curvilinear faults.

On the other hand, a comprehensive landslide wave generation theory still needs to be established. As Synolakis and K  no  lu (2009) state, "... the calculation of the initial wave from a submarine landslide remains an art and is still shrouded with controversy." One exception is Ward (2001)'s model for production, propagation and shoaling of landslide tsunamis using the Green's function method. Ward tested his theory with several real and hypothetical landslides and also included landslide tsunami hazard assessment in his analysis.

After determining the appropriate generation model for long waves (tsunamis), according to the geophysical source type of the sea-floor deformation, the next stage for an accurate modeling is selection of a proper propagation model.

Formulation of water wave problems can be done in several ways, leading to different level of approximations of the Navier-Stokes (NS) equations<sup>2</sup> such as the Korteweg-de Vries (KdV), Boussinesq, potential, or shallow-water wave equations, depending if, and how, features of the flow such as dissipation, (frequency) dispersion and/or nonlinearity are preserved. This study deals with solutions of wave flows dictated by the shallow-water wave theory, which is a nondispersive depth-averaged approximation of the NS equations. This theory has proven to be an adequate model for long wave propagation as the ocean medium is generally assumed to be nondispersive at that scale. It should be noted here that flow in the swash zone and related concepts such as formation of bores and wave breaking are beyond the scope of this thesis.<sup>3</sup>

---

<sup>2</sup> The Navier-Stokes equations, which arise from Newton's second law, are the most general equations that govern motion of any Newtonian fluid.

<sup>3</sup> For reference, the reader is referred to Whitham (1958) and also a series of pioneering studies by D. H. Peregrine and colleagues, e. g. Peregrine (1966, 1967), Brocchini and Peregrine (1996), and the references therein.

The conventional form of the (nonlinear) shallow-water wave (SW) equations is reformulated by Stoker (1948) although the original derivation is credited to Adhémar Jean Claude Barré de Saint-Venant (Saint-Venant equations). There are documents that trace the derivation even back to Joseph Louis Lagrange, who also derived the exact linear theory (Stoker, 1948). In the most general two-dimensional (2-D) case,<sup>4</sup> they consist of three first order nonlinear partial differential equations (PDEs) derived from the NS equations by first dropping the viscous terms and then averaging the velocity terms over the flow depth, using the shallow-water approximation. The averaging process together with the hydrostatic pressure assumption reduces the pressure term from the NS equations and introduces the water elevation as a dependent variable, along with the two horizontal velocity components. The resulting equations are coupled and they form a hyperbolic set of differential equations.

The long wave propagation phenomenon in one space dimension is first analyzed through experiments. Before late 1950's, the main focus was to develop formulas for a single long wave propagating over a linearly sloping beach. In their chronological tsunami hydrodynamics review, Synolakis and Bernard (2006) cite two significant experimental studies. The first belongs to Hall and Watts (1953), who introduced the canonical problem, i.e., a flat basin connected to a linear slope, resembling the deep ocean basin connected to the continental shelf (Figure 1.1). They generated in the laboratory solitary waves on the constant depth segment and allowed them to propagate through the sloping beach. They were able to relate the maximum wave runup to the offshore wave height ( $H$ ) and the beach slope ( $\beta$ ), hence, define an empirical runup relation. In another study, Wiegel (1955) performed experiments with a solid box sliding down a plane beach. He did not calculate the shoreline water elevation but he set the standard for landslide experiments.

The first, and arguably the most remarkable, analytical contribution came from Carrier and Greenspan (1958). They suggested an initial-value problem (IVP) solution for the nonlinear shallow-water wave (NSW) equations by means of the so-called hodograph transformation, now known as the Carrier-Greenspan (CG) transformation. This transformation consists of a pair of nonlinear relations introducing two new

---

<sup>4</sup> In the 2-D case, both space variables are preserved in the equations together with the temporal variable, while only one spatial variable is retained in addition to the time variable in the one-dimensional (1-D) case.

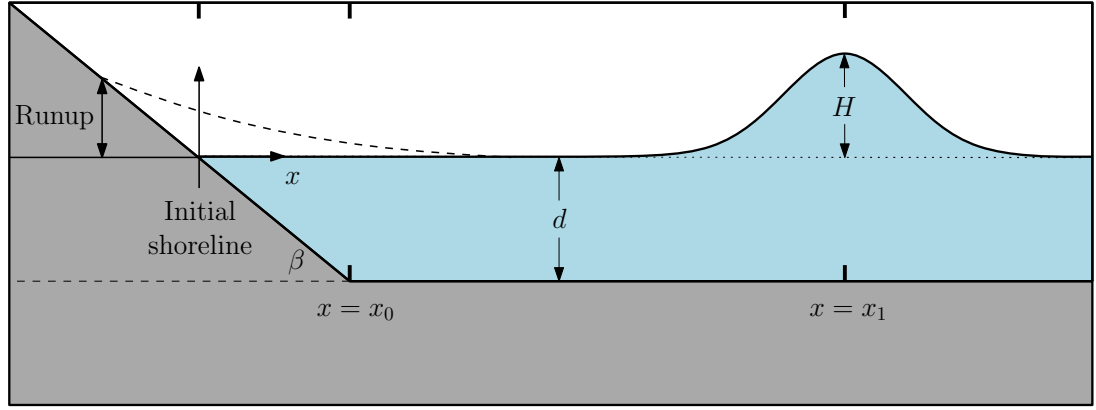


Figure 1.1: Definition sketch for the so-called canonical bathymetry (not to scale). The bathymetry consists of a plane beach connected to a constant depth basin.

auxiliary variables to replace the independent variables of the problem, i.e., the space ( $x$ ) and the time ( $t$ ) variables. Carrier and Greenspan (1958) were able to transform the two first order nonlinear PDEs into a single second order linear one. Furthermore, under this transformation, the ever changing location of the shoreline tip was mapped onto a fixed point. The solution in the hodograph plane was also straightforward. The resulting PDE was analogous to the classical wave equation written in polar coordinates, for which a solution could be given in terms of Bessel functions after applying the Fourier-Bessel (also known as Hankel) integral transform. However, despite the advantages listed above, Carrier and Greenspan (1958)'s study could not be benefited for a long time because of the difficulty in defining geophysically realistic initial wave profiles in the transform space.

Carrier (1966) extended the CG transformation to more general bottom configurations, including underwater ridges, and has drawn several important conclusions related to the physics of tectonic tsunamis. First, he argued that far from the initial shoreline the nonlinear effects are small. Second, he showed that effects of dissipation and the remaining bottom topography are minimal on tsunami runup, compared to the angle of the sloping beach. Third, he presented another justification of the fact that the first wave of a tsunami is not the largest wave in amplitude. These results were promising, but Carrier (1966)'s analysis did not include an important feature of wave propagation, namely reflection off the beach.

Meanwhile, the evolution of periodic waves propagating over the canonical bathymetry was modeled by Keller and Keller (1964) with the linear shallow-water wave (LSW) equations. By matching the respective solutions at the toe of the beach (point  $x = x_0$  in Figure 1.1), Keller and Keller (1964) was able to define the amplification of waves on the slope in terms of the initial height ( $H$ ) of the waves on the flat region.

These results have provided significant progress but they lacked geophysics as they were disjointed to the dynamics of the source event. Ben-Menahem and Rosenman (1972) provided the connection. They managed to calculate, using the linear theory, the two-dimensional radiation of the tsunami energy from a deforming source. Their calculations showed that the associated wave energy follows a path that is perpendicular to the rupturing fault. In another study, Tuck and Hwang (1972) calculated the state of the free-surface resulted by a deforming sea-floor by proposing a solution for the forced NSW equations; the time-dependent bottom deformation was implemented into the continuity equation as a forcing term. Although their aim was to capture offshore wave evolution and there were no results for shoreline motion, the solution of Tuck and Hwang (1972) constructed a basis for analytical models of underwater landslides.

Refined nonlinear analytical solution including reflection has been achieved by Synolakis (1986). He solved the NSW equations over the canonical bathymetry as a boundary-value problem (BVP) by using the Carrier-Greenspan transformation. In order to circumvent the previously mentioned difficulty experienced by Carrier and Greenspan (1958), Synolakis (1986) proceeded with the solution as Keller and Keller (1964) did, i.e., by imposing the linear solution as boundary data at the toe of the beach ( $x = x_0$ , see Figure 1.1). He justified this approach using the argument proposed by Carrier (1966), i.e., the negligibly small nonlinear effects far from the shore. In this way, he calculated the evolution of a solitary wave over the slope during both the runup and rundown phases. He compared his analytical results with non-breaking and breaking solitary waves created in the laboratory and he derived a breaking criterion. Furthermore, performing an asymptotic analysis and utilizing contour integration techniques, Synolakis (1986) derived analytical formula for the runup of a solitary wave over a sloping beach, known as the runup law. The form of the relation he found analytically is quite similar to the one proposed by Hall and Watts (1953)

from experimental data. This relation is now accepted as a standard analytical benchmark for numerical long wave propagation models (Synolakis et al., 2008). Synolakis (1986) was also able to show the runup invariance between the linear and nonlinear theories. This invariance affirms that, although linear and nonlinear waves evolve quite differently through the flow field, both will assume the same maximum runup.

Consequently, the ultimate goal until the end of 1980's was determination of the flow field and the runup characteristics of a solitary wave, initially placed on the constant depth, as it climbs onto the linear slope and reflects back. By the end of 1980's all aspects of solitary wave propagation were identified. Experimental (Hall and Watts, 1953; Synolakis, 1986), numerical (Pedersen and Gjevik, 1983), and analytical (Synolakis, 1986) solutions were available, and associated runup law and breaking criterion were defined. However, a series of tsunamis occurred in early 1990's challenged the solitary wave paradigm. The decade 1990-2000 was the tsunami decade, as named by Synolakis and Bernard (2006), due to high number of events. Only during the period 1992-1994, at least six major tsunamis occurred, i.e., 1 September 1992 Nicaragua, 12 December 1992 Flores Island (Indonesia), 12 July 1993 Hokkaido-Nansei-Oki (Japan), 2 June 1994 East Java (Indonesia), 2 October 1994 Kuril Islands (Russia), and 11 November 1994 Mindoro Island (Philippines) tsunamis. After each of these events, International Tsunami Survey Teams (ITSTs) surveyed the regions affected by the tsunamis. During these surveys, almost all eyewitnesses reported withdrawal of the shoreline before wave attacks, which questioned the convenience of the solitary wave as an initial condition.

Tadepalli and Synolakis (1994) responded this paradigm change by introducing a certain class of dipolar waves, called *N*-waves, to serve as more realistic initial form of tsunamis. They defined two particular waveforms: a wave with a trough followed by a crest, called leading depression *N*-wave (LDN), and a wave having a crest followed by a trough, called leading elevation *N*-wave (LEN). Using the solution methodology of Synolakis (1986), Tadepalli and Synolakis (1994) were able to obtain the evolution of LDN and LEN over the canonical bathymetry, and to define analogous runup laws, by performing asymptotic analysis. They showed that LDNs produce higher runup values than equivalent LENs, and LENs produce higher runup values than equivalent solitary waves. Tadepalli and Synolakis (1996) later proved the stability of *N*-waves,



which had been interrogated while they first suggested. So, Tadepalli and Synolakis (1994, 1996) settled the *N*-wave model as a geophysically realistic model for long wave propagation.

A more realistic model than the canonical bathymetry in terms of ocean basin profile is suggested by Kânoğlu (1998). He modeled the continental shelf and slope regions by piecewise linear slopes. Kânoğlu (1998)'s analytical formulation involves a matrix multiplication method inferred from optics, through which he eliminated the coefficients of the periodic wave solution at slope interfaces; hence, Kânoğlu (1998) was able to relate the wave reflection coefficient at the shoreline directly to the height of the initial wave defined over the constant depth. He then extended his solution to calculate the maximum runup of solitary waves over composite beaches. His asymptotic analysis revealed that the runup depends only on the slope closest to the shoreline for a composite beach and, if there is a vertical wall at the shoreline, runup primarily depends on the depth at the wall. Kânoğlu (1998) confirmed his analytical results through comparisons with laboratory data. The solution procedure is described by Kânoğlu and Synolakis (1998) in detail.

The new challenge is soon brought with the 17 July 1998 Papua New Guinea tsunami. At first, it appeared to be a minor tsunami event triggered by a relatively small earthquake. But it was realized after the field survey that there were extraordinary runup measurements, reaching as high as 15 *m*, i.e., the initial tectonic tsunami assumption was not enough to explain the high runup values in most of the influenced areas. The event is discussed in detail by Synolakis et al. (2002). Okal (2003b) proposed that the earthquake triggered a submarine landslide, with an argument based on hydroacoustic signals recorded in the region. Indeed, several hydrographic surveys identified a slump located 25 *km* offshore (Synolakis and Bernard, 2006). The landslide is now accepted as the real cause of the PNG tsunami. Numerical simulations of the event, together with results from the field survey, is presented in Lynett et al. (2003). The later events of the tsunami decade, namely the 17 August 1999 İzmit (Turkey), 13 September 1999 Fatu Hiva (Marquesas, French Polynesia) and 26 November 1999 Vanuatu tsunamis are all initiated from landslides and they have motivated further investigation of landslide tsunamis.

Liu et al. (2003) proposed an analytical model for landslide-generated long waves. They modeled a time-dependent bottom disturbance by the so-called Gaussian (bell-shaped) volume sliding over a linear slope. They applied a change of variables to the LSW equation and solved the resulting IVP by Hankel integral transform. They compared their solution with a nonlinear numerical solution and identified the runup distribution for different beach slope and sliding mass parameters.

Carrier et al. (2003) revisited the hodograph transformation solution of Carrier and Greenspan (1958). They formulated an IVP and proposed a solution for the NSW equations in terms of the Green's function. They presented maximum runup/minimum rundown results for Gaussian initial profiles. However, their solution has drawbacks such as evaluation of elliptic integrals, known to be highly singular, or unnecessary linearizations of dependent variables such as the initial velocity.

These issues are soon addressed by Kânoğlu (2004). He devised a method for defining the initial data in the hodograph plane. He first linearized the transformation at initial time ( $t = 0$ ) in the absence of initial velocity, without affecting the nonlinearity of the subsequent waves. This approach led to nonsingular integral solutions for the entire flow field as well as for the shoreline quantities. Kânoğlu (2004) also extended his analysis beyond the idealized Gaussian wave, incorporating solitary wave and isosceles and generalized  $N$ -wave profiles into his analysis, and presenting the associated runup and shoreline velocity distributions. Later, Kânoğlu and Synolakis (2006) complemented Kânoğlu (2004) by solving the general IVP with nonzero initial velocity condition.

Tinti and Tonini (2005) contributed to the one-dimensional shallow-water wave theory by analyzing in detail the runup of long waves caused by near-shore earthquakes. Considering a generic initial wave which accounts for different tectonic configurations, they identified the parameters those have significant effect on tsunami runup. They introduced a parameter called amplification factor, defined as the ratio of the maximum vertical excursion of the wave measured at the coast and the initial wave height. Tinti and Tonini (2005) exposed that the amplification factor, which ranges between one and two, increases as the epicenter of the earthquake moves from inland towards the sea bed. In other words, they showed that tsunamis induced by

earthquakes occurring under the sea amplify more than those induced by earthquakes having an epicenter inland.

Antuono and Brocchini (2007) solved the BVP for the NSW equations. They assigned appropriate boundary conditions, transformed them to the hodograph space together with the governing equations, and sought an approximate solution via perturbation methods. They assumed periodic and Gaussian shaped data with small height at the seaward boundary and successfully compared their solution with existing laboratory measurements. Their solution is advantageous as it is possible to monitor the interaction of incoming and outgoing waves at the seaward boundary.

Later, Antuono and Brocchini (2010) applied the same solution technique, namely the perturbation expansion, to the original equations, i.e., equations in the physical space. Besides comparing with their previous benchmark boundary profiles, they presented results for the solitary wave and derived analytical breaking conditions. Their results reveal that the first order perturbation solution in the physical space is comparable to the second order solution evaluated in the hodograph space.

The number of analytical models for the shallow-water wave equations involving two space dimensions, on the other hand, is quite few compared to the one-dimensional case. Carrier and Noiseux (1983) calculated the reflection of obliquely-incident waves from a plane beach using the LSW theory. They defined a relation which combines the temporal variable, the longshore<sup>5</sup> space variable, and the angle of wave incidence. They treated this relation as an independent variable, i.e., as a coordinate, and Carrier and Noiseux (1983) were consequently able to reduce the number of independent variables by one. Using the Fourier integral transform method, they solved the resulting one-dimensional equation over the canonical bathymetry and they matched the two solutions to obtain the reflection coefficient.

In an attempt to obtain flow properties in the swash zone, Brocchini and Peregrine (1996) presented a weak solution for the two-dimensional NSW equations as an extension of the CG transformation for the 1-D equations, again for waves propagating towards a plane beach with a small angle of incidence, as in Carrier and Noiseux

---

<sup>5</sup> In the terminology of the two-dimensional propagation, the onshore variable refers to the space variable that is normal to the shoreline, which is considered as the main propagation direction, and the longshore variable is the horizontal space variable that is assumed to be parallel to the shoreline.

(1983). Following a similar strategy, they defined a new variable which they call pseudo-time, by combining the temporal and longshore spatial variables, which led to two decoupled problems for onshore and longshore propagation. They were able to solve the onshore problem with the CG transformation and represent the solution of the longshore problem in terms of the onshore solution. The two solutions, computed for the same value of the temporal variable, construct the 2-D flow field.

Kânoğlu and Synolakis (1998) computed the runup of solitary wave around a conical island. They started with the 2-D LSW equation. Using the rotational invariance of the bathymetry, they reduced the dimension of the governing equation, and solved the reduced equation for cylindrical sills, with which they approximated the bathymetry around the island. They matched the solutions at each sill interface using the matrix method introduced by Kânoğlu (1998) and they obtained the maximum runup of a solitary wave around the conical island. They also compared their analytical solution with results of several laboratory experiments.

Carrier and Yeh (2005) developed an analytical solution based on a methodology previously defined by Carrier (1990) to evaluate propagation of finite-crest length sources over a flat bathymetry. Carrier and Yeh (2005) made use of the unidirectionality of the bathymetry, as in Kânoğlu and Synolakis (1998), and converted the 2-D LSW equations into the wave equation written in cylindrical coordinates. They called this problem the axisymmetric problem, for which they formulated a Green's function solution using the IVP approach of Carrier et al. (2003). They obtained solution for a 2-D Gaussian initial wave having finite-crest length in the longshore direction. However, their analytical solution is not exact as it has drawbacks<sup>6</sup> similar to the Carrier et al. (2003) solution, briefly mentioned above. Nonetheless, their solution still allowed here for discussion of the directivity of finite-crested initial tsunami sources.

Sammarco and Renzi (2008) provided an analytical solution for two-dimensional landslide-generated tsunamis propagating along a plane beach. They assumed Gaussian sea-floor disturbance and they were able to express the solution in terms of Laguerre polynomials after transforming the forced NSW equations with the Fourier cosine transform. They also validated their solution by comparing with experimental

---

<sup>6</sup> A detailed analysis of Carrier and Yeh (2005) solution is presented in Section 4.3.1.

data.

Renzi and Sammarco (2010) solved the landslide problem around a conical island. They analyzed the problem via the separation of variables and Laplace transform methods and expressed the solution, again for a Gaussian landslide, in terms of special functions, namely the confluent Heun functions. They discussed the differences in the physical features of subsequent waves propagating around an island and along a straight coast in view of their previous model (Sammarco and Renzi, 2008).

The shortly summarized achievements in analytical modeling of the shallow-water wave theory over more than last fifty years, along with the ones that are not mentioned here because they are beyond the scope of this study, has definitely been vital in better understanding of the physics of long waves (tsunamis), besides their indispensable role in validation of the state-of-the-art numerical models (Synolakis et al., 2008). In this study, new solutions of linear and nonlinear shallow-water wave equations are developed.

A basic solution technique utilizing the CG transformation is developed for calculation of the shoreline velocity and the maximum runup of a wide class of initial waveforms having zero and nonzero initial velocity distributions. This technique is then used to calculate the wind-triggered nonlinear oscillations in a gulf, in an effort to exhibit the applicability of the hodograph-type transformations to practical coastal engineering problems.

In two space dimensions, propagation of a finite-crest length initial source over a flat ocean is obtained by using the LSW theory. The idea was to model the initial wave resulting from a finite fault rupture. The Fourier integral transform over space variables is used as the solution method. Different initial source configurations including solitary and  $N$ -wave profiles are analyzed. The focusing of plus-minus sources (sources having a crest-trough configuration, i.e.,  $N$ -waves), first suggested by Marchuk and Titov (1989) in a numerical study, is shown analytically. The unexpected localized maximum runup values observed during several recent tsunami events are also re-examined in view of the source focusing phenomenon.

Flow field generated by a sliding mass on ocean bottom is also modeled with the NSW

equations together with the hodograph transformation and presented in Appendix B. For this purpose, a Gaussian bottom profile perturbing over a linearly sloping beach is considered. This problem has nonhomogeneous governing differential equations (the forced NSW equations) due to the bottom forcing; hence, the solution is given as the sum of two components, a particular solution obtained by using the approach of Liu et al. (2003), and a homogeneous solution obtained through the Fourier-Bessel (Hankel) integral transform technique.

## CHAPTER 2

### AN INITIAL-BOUNDARY VALUE PROBLEM FOR THE NONLINEAR SHALLOW-WATER WAVE EQUATIONS

Majority of the hodograph transformation solutions of the one-dimensional nonlinear shallow-water wave (NSW) equations described in Chapter 1 are obtained through integral transform techniques such as Fourier or Fourier-Bessel (Hankel) transforms. However, as already summarized in the previous chapter, the original formulation of Carrier and Greenspan (1958) and its variant Carrier et al. (2003) involve evaluation of elliptic integrals. Since elliptic integrals are highly singular, this solution methodology requires either approximation of the associated integrands by smooth functions or selection of regular initial/boundary data. It should be noted that Kânoğlu (2004) partly resolves this issue by simplifying the resulting integrals in closed form.

In this section, the hodograph transform approach is coupled with the classical eigenfunction expansion method rather than integral transform techniques and a new analytical model for nonlinear long wave propagation over a plane beach is derived. In contrast to classical initial- or boundary-value problem solutions, here, the NSW equations are formulated to yield an initial-boundary value problem (IBVP) solution. In general, initial wave profile with nonzero initial velocity distribution is assumed and the flow variables are given in the form of Fourier-Bessel series. The results reveal that the developed method allows accurate estimation of the spatial and temporal variation of the flow quantities, i.e., free-surface height and depth-averaged velocity, with much less computational effort compared to the integral transform techniques such as Carrier et al. (2003) and Kânoğlu (2004).

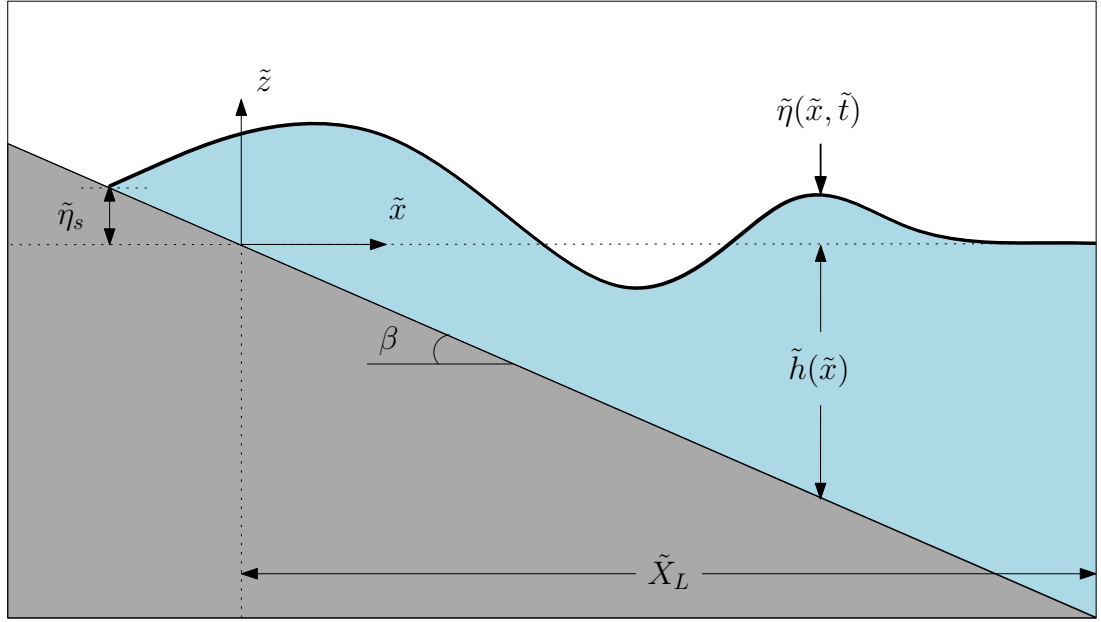


Figure 2.1: Definition sketch (not to scale). The variables with tilde show dimensional quantities.

## 2.1 Mathematical Formulation

The one-dimensional NSW equations in nondimensional form can be written as

$$\eta_t + [(h + \eta) u]_x = 0, \quad (2.1a)$$

$$u_t + u u_x + \eta_x = 0, \quad (2.1b)$$

where  $0 \leq x \leq X_L$ ,  $0 \leq t$ , and  $\eta(x, t)$ ,  $u(x, t)$ , and  $h(x) = x$  represent the free-surface elevation, the depth-averaged velocity, and the undisturbed water depth, respectively (Figure 2.1). The subscripts denote derivative with respect to that variable. Here, the nondimensional variables are defined as

$$x = \frac{\tilde{x}}{l_0}, \quad (h, \eta) = \frac{(\tilde{h}, \tilde{\eta})}{l_0 \tan \beta}, \quad u = \frac{\tilde{u}}{\sqrt{g l_0 \tan \beta}}, \quad t = \frac{\tilde{t}}{\sqrt{l_0/(g \tan \beta)}}, \quad (2.2)$$

where  $l_0$ ,  $g$ , and  $\beta$  represent the characteristic length scale, the gravitational acceleration, and the beach angle with horizontal, respectively. Here,  $X_L$  is specified in such a way that initial wave profile could entirely be defined in the interval  $0 \leq x \leq X_L$  and reflected wave<sup>1</sup> from the boundary  $x = X_L$  will not reach the shoreline to contaminate

<sup>1</sup> The solution method described below results in wave reflection from the seaward boundary as explained in detail later in this section.



the solution.

The general initial conditions are a prescribed initial wave profile with a corresponding nonzero velocity distribution,

$$\eta(x, t = 0) = \eta_0(x), \quad (2.3a)$$

$$u(x, t = 0) = u_0(x) \neq 0. \quad (2.3b)$$

The hodograph transformation

$$\sigma = \sqrt{x + \eta}, \quad (2.4a)$$

$$\lambda = t - u, \quad (2.4b)$$

is introduced following Carrier and Greenspan (1958). These two relations replace the independent variables of the problem  $(x, t)$  with the respective auxiliary variables  $(\sigma, \lambda)$ . The advantages of the hodograph transformation are two-fold. First, the governing differential equations can be linearized with the help of Eqs. (2.4). Second, the instantaneous shoreline tip  $(x = -\eta)$  in the physical coordinates is mapped onto a fixed point  $(\sigma = 0)$  in the hodograph space through Eq. (2.4a). Eqs. (2.4) transform Eqs. (2.1) into

$$(\sigma^2 u)_\sigma + 2\sigma \left(\eta + \frac{u^2}{2}\right)_\lambda = 0, \quad (2.5a)$$

$$2\sigma u_\lambda + \left(\eta + \frac{u^2}{2}\right)_\sigma = 0, \quad (2.5b)$$

in the hodograph  $(\sigma, \lambda)$ -space. Further defining a potential function as

$$\varphi = \eta + \frac{u^2}{2}, \quad (2.6)$$

the velocity  $u$  can be eliminated in between Eqs. (2.5) after some algebra. The resulting equation is a second-order linear differential equation expressed in terms of  $\varphi$ , i.e.,

$$4\varphi_{\lambda\lambda} - \frac{1}{\sigma}(\sigma\varphi_\sigma)_\sigma = 0. \quad (2.7)$$

The next step is to define the initial conditions in the hodograph space, which is achieved by substituting the linearized form of Eq. (2.4a), i.e.,  $x \approx \sigma^2$ , into the physical initial conditions (2.3), as in Kânoğlu (2004). So, the interval  $0 \leq x \leq X_L$  is

mapped onto  $0 \leq \sigma \leq \sigma_L = \sqrt{X_L}$  and the initial conditions in the hodograph space are given as

$$\eta(x, t = 0) \approx \eta(\sigma, \lambda = \lambda_0) \equiv \eta_0(\sigma), \quad (2.8a)$$

$$u(x, t = 0) \approx u(\sigma, \lambda = \lambda_0) \equiv u_0(\sigma). \quad (2.8b)$$

At this point, it should be noted that a nonzero initial velocity, Eq. (2.3b), implies from Eq. (2.4b) that  $\lambda = \lambda_0 \neq 0$  at  $t = 0$ . In the absence of initial velocity, i.e.,  $u \equiv 0$ , this relation simply gives  $\lambda = 0$  corresponding to  $t = 0$ . This is discussed in Kânoğlu and Synolakis (2006) in detail. The initial conditions (2.8) can be rewritten in terms of  $\varphi$  as

$$\varphi(\sigma, \lambda = \lambda_0) = \eta_0(\sigma) + \frac{u_0^2(\sigma)}{2} \equiv P(\sigma), \quad (2.9a)$$

$$\varphi_\lambda(\sigma, \lambda = \lambda_0) = -u_0(\sigma) - \frac{\sigma}{2} u_0'(\sigma) \equiv F(\sigma), \quad (2.9b)$$

from Eqs. (2.6) and (2.5a), respectively.

In terms of boundary conditions, the solution at the shoreline tip ( $\sigma = 0$ ) is required to be bounded. A well-posed IBVP in the hodograph space requires a boundary condition in terms of the potential function  $\varphi$  at the seaward boundary,  $\sigma = \sigma_L$  (corresponding to  $x = X_L$  in the physical space). Since  $\varphi$  is defined as  $\varphi = \eta + u^2/2$ , this condition will involve both  $\eta$  and  $u$  in the physical space. An absorbing boundary at  $x = X_L$  requires

$$\eta(x = X_L, t) = 0 \quad \text{and} \quad u(x = X_L, t) = 0, \quad (2.10)$$

derived from the characteristics (Riemann invariants) of the NSW equations (Gustafsson and Kreiss, 1979). Titov (1997) used this condition in the numerical solution of the NSW equations, i.e., Eqs. (2.1). In terms  $\varphi$ , Eqs. (2.10) yield through Eq. (2.6) the condition  $\varphi(\sigma = \sigma_L, \lambda) = 0$ . Therefore, the necessary boundary conditions in the hodograph space are

$$\varphi(\sigma = 0, \lambda) = \text{finite}, \quad (2.11a)$$

$$\varphi(\sigma = \sigma_L, \lambda) = 0. \quad (2.11b)$$

Even if Eq. (2.10) is an absorption condition, calculations performed in the next section suggest that the right-going wave reflects from the boundary  $x = X_L$ , as also explained by Antuono and Brocchini (2007). Nevertheless, the aim of providing basic

formulas that explain properties of waves at the shoreline only requires the calculations carried out up to a threshold time; so, appropriate choice of  $X_L$  can prevent the reflected wave from reaching the shoreline, i.e., Eq. (2.11b) can be used as an open sea boundary condition.

The IBVP formulated above is suitable for a solution with the classical separation of variables method. Writing  $\varphi(\sigma, \lambda) = F(\sigma) G(\lambda)$ , Eq. (2.7) gives

$$\frac{4}{G} \frac{d^2 G}{d\lambda^2} = \frac{1}{F} \left( \frac{d^2 F}{d\sigma^2} + \frac{1}{\sigma} \frac{dF}{d\sigma} \right) = -\kappa^2, \quad (2.12)$$

with a real constant  $\kappa$ . Eq. (2.12) yields the ordinary differential equations

$$\sigma^2 F'' + \sigma F' + \kappa^2 \sigma^2 F = 0, \quad (2.13a)$$

$$G'' + \frac{\kappa^2}{4} G = 0. \quad (2.13b)$$

The differential equation for  $F(\sigma)$  is the Bessel's equation of order zero and it has the general solution

$$F(\sigma) = c_1 J_0(\kappa\sigma) + c_2 Y_0(\kappa\sigma), \quad (2.14)$$

where  $J_0(z)$  and  $Y_0(z)$  are the Bessel functions of the first and the second kind of order zero, respectively, and  $c_1$  and  $c_2$  are arbitrary constants. Boundness condition at the shoreline, Eq. (2.11a), requires  $c_2 = 0$ . The open sea condition  $\varphi(\sigma = \sigma_L, \lambda) = 0$  implies  $F(L) = 0$ . The eigenvalues of the problem are determined from this condition as the positive zeros of  $J_0(z)$ .

The general solution of the differential equation given in Eq. (2.13b) is

$$G(\lambda) = c_3 \cos \frac{\kappa}{2} \lambda + c_4 \sin \frac{\kappa}{2} \lambda, \quad (2.15)$$

and the solution of the IBVP can be constructed by the superposition of Eq. (2.14) and Eq. (2.15) as

$$\varphi(\sigma, \lambda) = \sum_{n=1}^{\infty} J_0(2\alpha_n \sigma) [A_n \cos \alpha_n \lambda + B_n \sin \alpha_n \lambda], \quad (2.16)$$

denoting  $\alpha_n = z_n/2\sigma_L$  where  $z_n$  are the zeros of  $J_0(z)$ , following from Eq. (2.11b)<sup>2</sup>. In order to calculate the unknown coefficients  $A_n$  and  $B_n$  ( $n \geq 1$ ), the initial conditions given in Eqs. (2.9) are considered. The final formulas for  $A_n$  and  $B_n$  are,

$$A_n = \frac{2}{\alpha_n \sigma_L J_1^2(z_n)} [\alpha_n P_n \cos \alpha_n \lambda_0 - F_n \sin \alpha_n \lambda_0], \quad (2.17a)$$

---

<sup>2</sup> The first few zeros of the function  $J_0(z)$  are:  $z_1 = 2.405$ ,  $z_2 = 5.520$ ,  $z_3 = 8.654$ , ...

$$B_n = \frac{2}{\alpha_n \sigma_L J_1^2(z_n)} [\alpha_n P_n \sin \alpha_n \lambda_0 + F_n \cos \alpha_n \lambda_0], \quad (2.17b)$$

where  $\lambda_0 = -u_0(\sigma)$  and

$$\begin{Bmatrix} P_n \\ F_n \end{Bmatrix} = \int_0^{\sigma_L} \sigma \begin{Bmatrix} P(\sigma) \\ F(\sigma) \end{Bmatrix} J_0(z_n \sigma) d\sigma. \quad (2.18)$$

Here,  $P(\sigma)$  and  $F(\sigma)$  are given by Eqs. (2.9a) and (2.9b), respectively. This completes the solution (2.16) of the IBVP defined for the potential function  $\varphi$ .

The depth-averaged velocity  $u(\sigma, \lambda)$  follows from Eq. (2.5b) as

$$u(\sigma, \lambda) = \frac{1}{\sigma} \sum_{n=1}^{\infty} J_1(2\alpha_n \sigma) [A_n \sin \alpha_n \lambda - B_n \cos \alpha_n \lambda]. \quad (2.19)$$

Given  $\varphi(\sigma, \lambda)$  and  $u(\sigma, \lambda)$  in the hodograph space, the necessary information to invert the hodograph solution to the physical space is now available. The solution in  $(x, t)$ -space can be calculated through the inversion algorithm

$$\eta(\sigma, \lambda) = \varphi(\sigma, \lambda) - \frac{u^2(\sigma, \lambda)}{2}, \quad (2.20a)$$

$$x(\sigma, \lambda) = \sigma^2 - \eta(\sigma, \lambda), \quad t(\sigma, \lambda) = \lambda + u(\sigma, \lambda), \quad (2.20b,c)$$

following directly from Eqs. (2.6) and (2.4), respectively. Spatial distribution of the wave height at any time  $t = t^*$  or temporal variation at any location  $x = x^*$  can be evaluated through the Newton-Raphson iteration scheme (Synolakis, 1987; Kânoğlu, 2004).

The wave dynamics at the shoreline is obtained by substituting  $\sigma = 0$  in Eqs. (2.16), (2.19) and (2.20). The singularity of Eq. (2.19) at  $\sigma = 0$  can easily be handled with the use of

$$\lim_{z \rightarrow 0} \frac{J_1(\xi z)}{z} = \frac{\xi}{2}, \quad (2.21)$$

and the shoreline velocity becomes

$$u_s(\lambda) = \sum_{n=1}^{\infty} \alpha_n [A_n \sin \alpha_n \lambda - B_n \cos \alpha_n \lambda]. \quad (2.22)$$

So, the temporal variation of the shoreline position is obtained from Eqs. (2.20b,c) as

$$x_s(\lambda) = u_s^2(\lambda)/2 - \varphi(0, \lambda), \quad (2.23)$$

corresponding to

$$t_s(\lambda) = \lambda + u_s(\lambda). \quad (2.24)$$

## 2.2 Applications

In this section, the solution method described in the previous section is applied to a number of initial wave profiles and the results are compared with existing solutions given by Carrier et al. (2003) and Kânoğlu (2004). Comparison with the solution given by Tinti and Tonini (2005) for initial waveforms resulting from near-shore earthquakes is also performed. In summary, it is shown that the method presented here is flexible in terms of initial conditions and it is possible to obtain the shoreline motion details of physically realistic initial waveforms with much less computational effort.

### 2.2.1 Gaussian wave

A Gaussian wave (single hump) is defined by

$$\eta(x, t = 0) = \eta_0(x) = h_1 e^{-c_1(x-x_1)^2}. \quad (2.25)$$

The parameters  $h_1$ ,  $x_1$ , and  $c_1$  determine the initial height, the location, and the steepness of the profile, respectively. Using the Hankel integral transform, time evolution of shoreline wave heights and velocities are computed by Carrier et al. (2003) and Kânoğlu (2004) for positive ( $h_1 > 0$ ) and negative ( $h_1 < 0$ ) initial waves (Figures 2.2(a,b)), with parameters taken from Carrier et al. (2003) (Table 2.1, cases 1 and 2). The translation of the Gaussian wave to the hodograph space is achieved by using the approach of Kânoğlu (2004), i.e., Eq. (2.4a) is linearized by neglecting  $\eta$ , so that  $x \approx \sigma^2$ . This relation is then substituted into Eq. (2.25) and the initial condition in the hodograph space is obtained as

$$\eta_0(\sigma) = h_1 e^{-c_1(\sigma^2-\sigma_1^2)^2}, \quad (2.26)$$

where  $\sigma_1 = \sqrt{x_1}$ .

A waveform having depression followed by elevation, also called leading depression *N*-wave, can also be constructed by combining two Gaussian waves as

$$\eta_0(x) = h_1 e^{-c_1(x-x_1)^2} - h_2 e^{-c_2(x-x_2)^2}. \quad (2.27)$$

Table 2.1: The corresponding parameters for the initial wave profiles presented in Eqs. (2.25) and (2.27) as in Carrier et al. (2003). The extreme wave height values –maximum runup and minimum rundown– for the cases with/without initial velocity are also tabulated. The exact initial velocity relation is considered in the calculations.

		Maximum runup / minimum rundown									
		Wave parameters						without velocity			
Case		$h_1$	$h_2$	$c_1$	$c_2$	$x_1$	$x_2$	$\eta_{max}$	$\eta_{min}$	$\eta_{max}$	$\eta_{min}$
1	Figure 2.3(a)	0.017	-	4.0	-	1.69	-	0.0470	-0.0268	0.0977	-0.0499
2	Figure 2.3(b)	-0.017	-	4.0	-	1.69	-	0.0268	-0.0464	0.0497	-0.0847
3	Figure 2.3(c)	0.020	0.010	3.5	3.5	1.5625	1.0	0.0583	-0.0231	0.1184	-0.0446
4	Figure 2.3(d)	0.006	0.018	0.4444	4.0	4.1209	1.6384	0.0328	-0.0470	0.0618	-0.0971

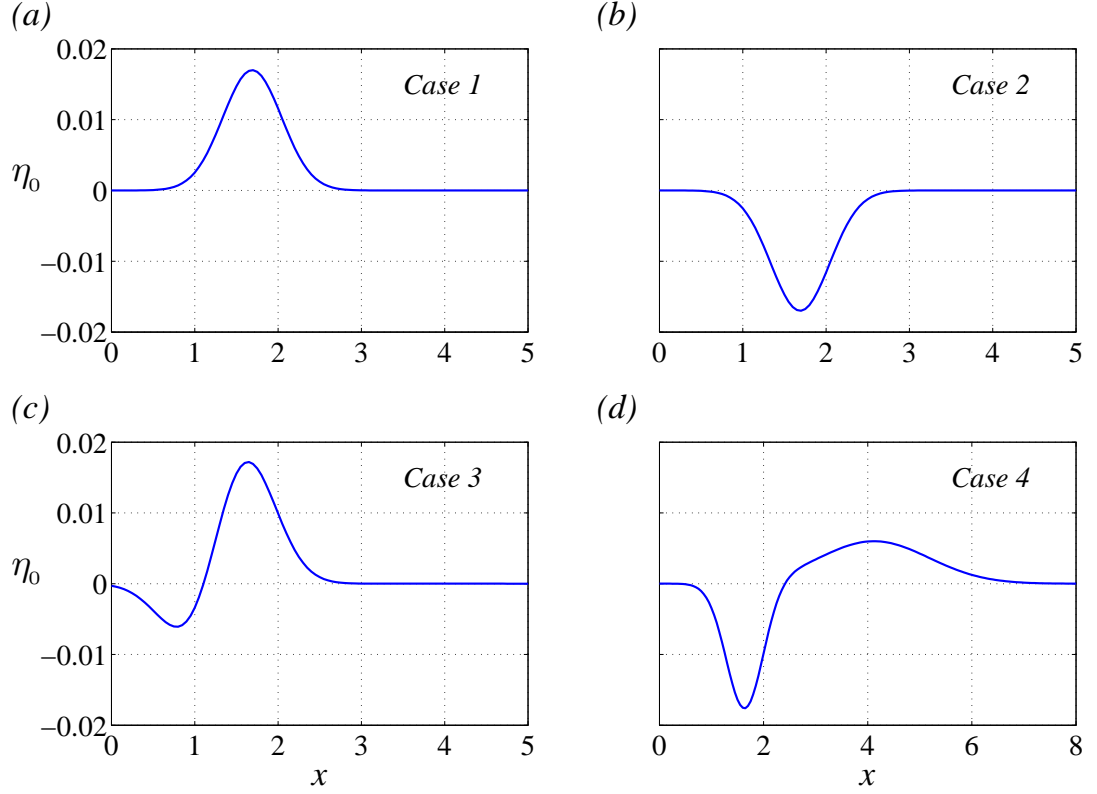


Figure 2.2: The initial wave profiles suggested by Carrier et al. (2003). (a) and (b) show the positive and negative Gaussian initial waves defined by Eq. (2.25) while (c) and (d) show the leading depression  $N$ -wave initial profile defined by Eq. (2.27) given for two different sets of parameters. The respective wave parameters are tabulated in Table 2.1.

Again, the parameters used by Carrier et al. (2003) is employed (Table 2.1, cases 3 and 4, and Figures 2.2(c,d)). This leading depression  $N$ -wave is translated into hodograph space as

$$\eta_0(\sigma) = h_1 e^{-c_1 (\sigma^2 - \sigma_1^2)^2} - h_2 e^{-c_2 (\sigma^2 - \sigma_2^2)^2}, \quad (2.28)$$

where, again,  $\sigma_1 = \sqrt{x_1}$  and  $\sigma_2 = \sqrt{x_2}$ . The shoreline wave height  $\eta_s(\lambda)$  and the shoreline velocity  $u_s(\lambda)$  for the waves defined in Eqs. (2.25) and (2.27) under zero initial velocity assumption, i.e.,  $u_0 \equiv 0$ , are successfully compared in Figure 2.3 with those of Kânoğlu (2004).

The wave dynamics at the shoreline is obtained under nonzero initial velocity condition as well. An exact nonlinear initial velocity relation, Eq. (2.29), can be derived

from the NSW equations (Kânoğlu and Synolakis, 2006).<sup>3</sup> It is observed that, if the initial velocity distribution for the Gaussian wave, i.e., Eq. (2.25) or Eq. (2.27), is assumed as in Eq. (2.29), then the maximum wave runup increases more than 85% compared to the zero initial velocity case (Table 2.1). Similarly, the lowest increase for the minimum rundown is 82%.

The effect of different initial velocity assumptions on wave height is also investigated. Three initial velocity assumptions are considered. The first one is the exact nonlinear relation

$$u_0(x) = 2\sqrt{x} - 2\sqrt{x + \eta_0(x)}. \quad (2.29)$$

Due to difficulties encountered in computations, Carrier et al. (2003) replaced the exact relation with the linear velocity approximation given by

$$u_0(x) \approx -\frac{\eta_0(x)}{\sqrt{x}}. \quad (2.30)$$

On the other hand, Prichard and Dickinson (2007) has suggested

$$u_0(x) \approx -\eta_0(x), \quad (2.31)$$

in their asymptotic near-shore analysis of the problem. In Figure 2.4 the shoreline wave heights (left insets) and the shoreline velocities (right insets) are compared for the three different approximations of initial velocity. It is observed that, while the exact and the linear velocity assumptions produce almost identical results, also identified by Kânoğlu and Synolakis (2006), the asymptotic relation used by Prichard and Dickinson (2007) produces slightly higher runup values.

In Figures 2.5 and 2.6, spatial variations of the free-surface elevation  $\eta$  for the positive Gaussian initial wave given in Figure 2.2(a) under the exact initial velocity condition (2.29) are compared with spatial variations of the same wave having zero initial velocity. Initial wave is splitted into two waves –shoreward and offshore going waves– in the absence of initial velocity (Figure 2.5(b)), as expected. In the calculations, the seaward boundary  $X_L$  is chosen at enough distance so that the reflection does not contaminate the solution near the shoreline.

---

<sup>3</sup> Comparison of the cases with and without initial velocity is also discussed in Kânoğlu and Synolakis (2006).



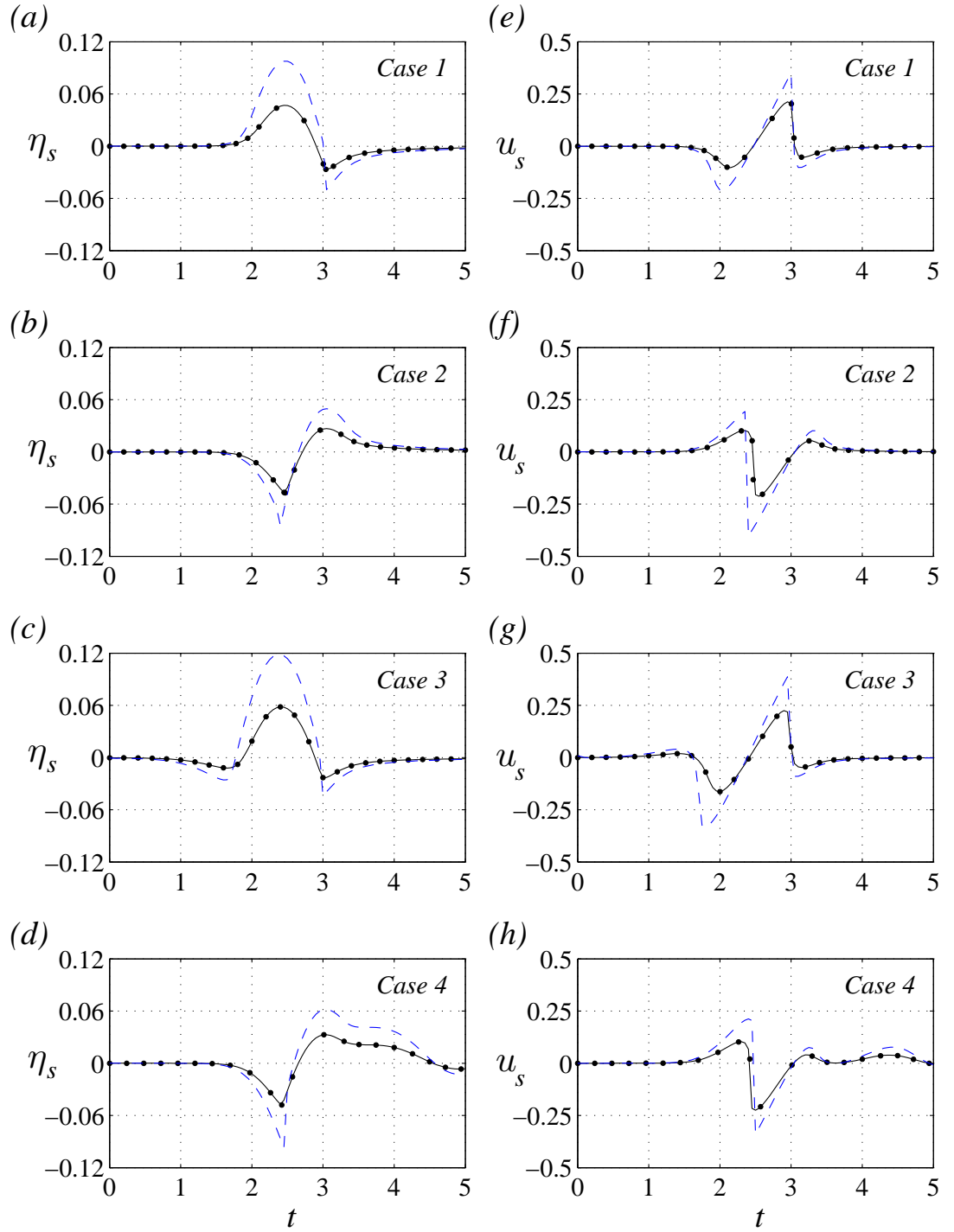


Figure 2.3: Time variations of (a) – (d) the shoreline positions  $\eta_s$ , and (e) – (h) the shoreline velocities  $u_s$  for the initial waves given in Figure 2.2. Dashed and solid lines represent the present solution with and without initial velocity, respectively, while dots represent results of Kânoğlu (2004) without velocity. The initial wave parameters and the maximum runup/minimum rundown heights are tabulated in Table 2.1.

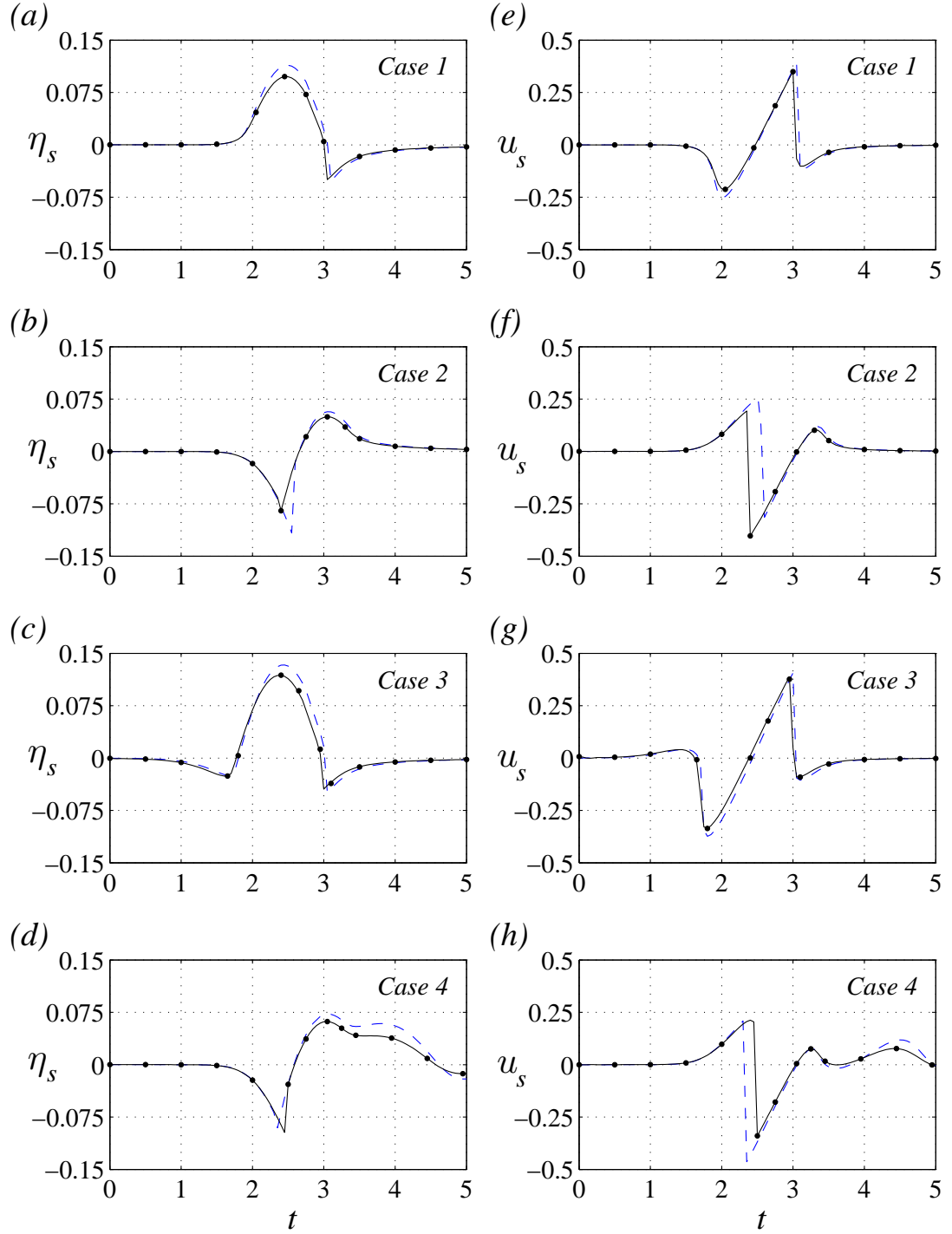


Figure 2.4: Comparison of the variation of (a) – (d) the shoreline wave heights, and (e) – (h) the shoreline wave velocities for the three different initial velocity relations. Solid lines represent results for the exact nonlinear value, Eq. (2.29), while dots and dashed lines stand for the results of the linear and the asymptotic velocity approximations, i.e., Eqs. (2.30) and (2.31), respectively. The initial wave parameters are presented in Table 2.1.

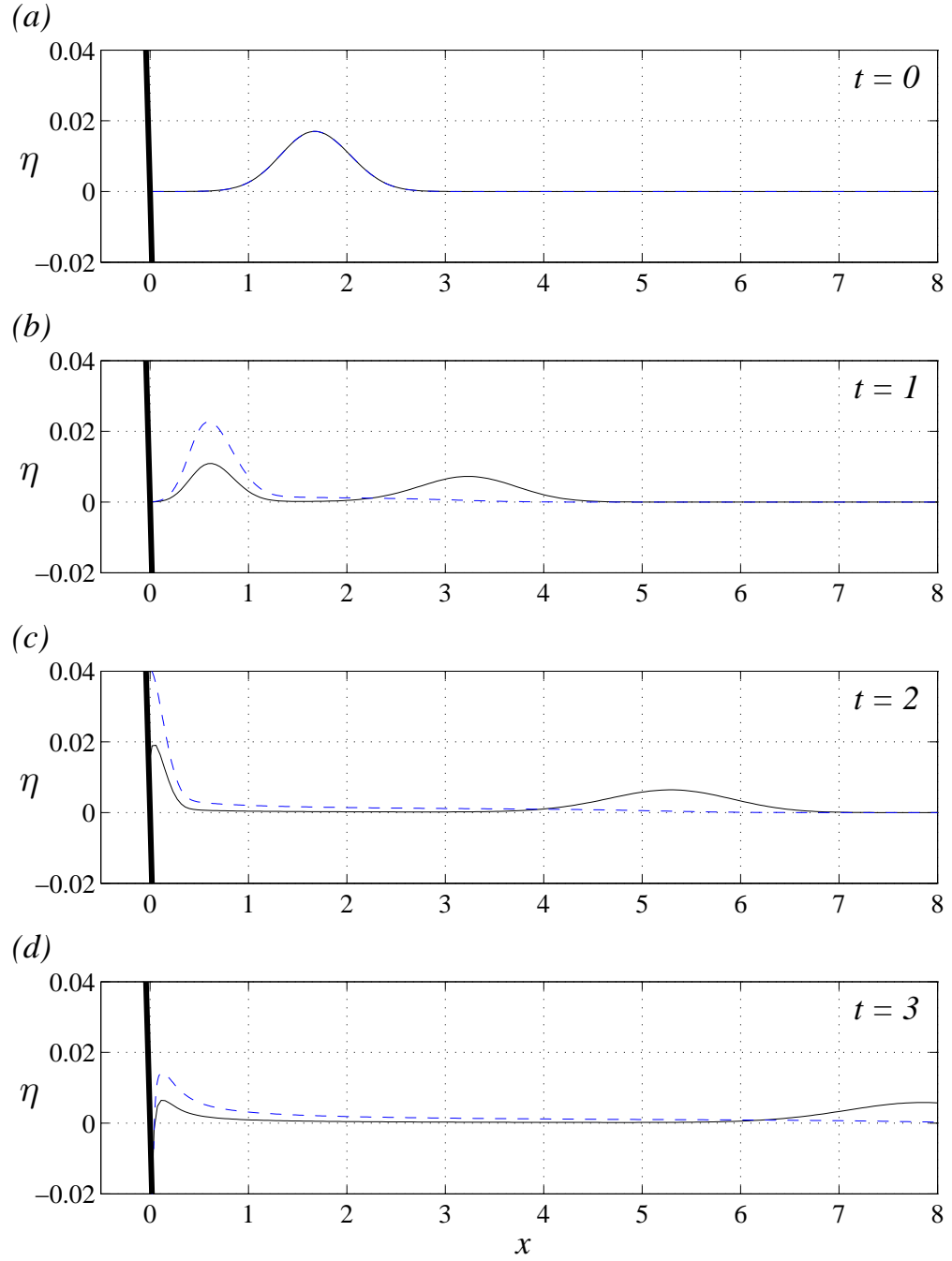


Figure 2.5: Spatial variations of the free-surface elevation of the Gaussian wave given in the case 1 of Table 2.1 (Figure 2.2(a)). Dashed and solid lines represent the solution with and without initial velocity, respectively, and thick lines represent the linearly sloping beach. In the absence of initial velocity, splitted wave propagates away from the shore as seen, for example, in inset (b). The seaward boundary is at  $X_L = 50$  so that the reflected wave does not reach the shoreline.

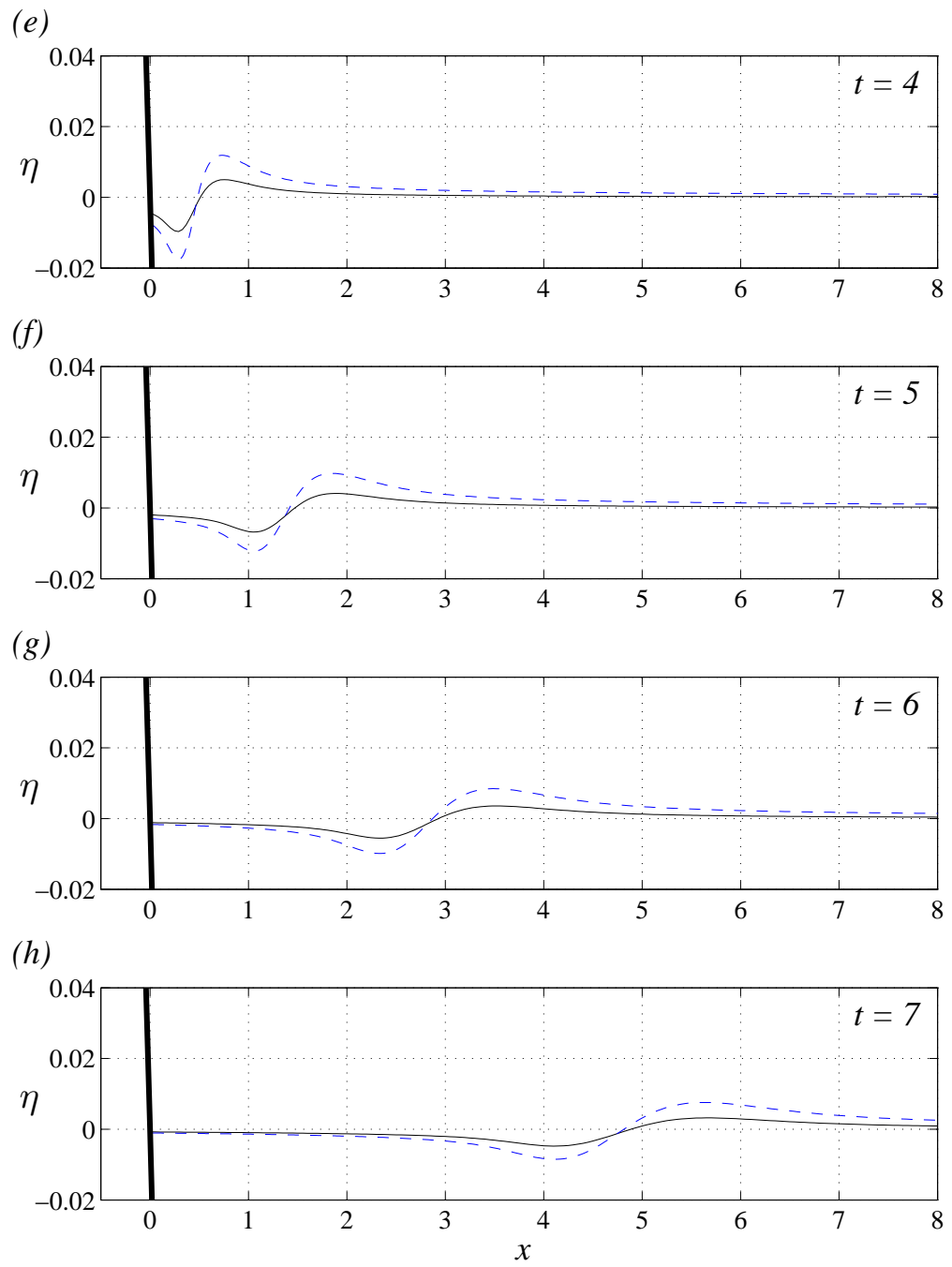


Figure 2.6: Continued from Figure 2.5.

### 2.2.2 Solitary wave

A solitary wave with initial height  $H$  located at  $x = x_1$  is defined as

$$\eta_0(x) = H \operatorname{sech}^2 \gamma_s (x - x_1), \quad (2.32)$$

where  $\gamma_s = \sqrt{3H/4}$ . This wave transforms to

$$\eta_0(\sigma) = H \operatorname{sech}^2 \gamma_s (\sigma^2 - \sigma_1^2), \quad (2.33)$$

in the hodograph space. Evolution of a solitary wave with  $H = 0.03$  and  $x_1 = 30$  is given in Figure 2.7. The initial wave is plotted in Figure 2.7(a) and the corresponding nonlinear initial velocity obtained from Eq. (2.29) is shown in Figure 2.7(b). The temporal variations of the shoreline wave height and the velocity of the solitary wave are given in Figures 2.7(c,d), respectively. The maximum runoff and minimum rundown values for the cases with and without velocity are tabulated in Table 2.2 (case 1). It is observed that the presence of the initial velocity results in approximately twice the shoreline wave height compared to the no initial velocity case.

### 2.2.3 Isosceles $N$ -wave

Tadepalli and Synolakis (1994) introduced two dipolar waveforms as more realistic initial profiles for the initial surface response of seafloor displacements. The first one is the isosceles  $N$ -wave profile is defined as

$$\eta_0(x) = \frac{3\sqrt{3}}{2} H \operatorname{sech}^2 \gamma_i (x - x_1) \tanh \gamma_i (x - x_1), \quad (2.34)$$

with  $\gamma_i = (3/2) \sqrt{H \sqrt{3/4}}$ . This profile, given in Figure 2.8(a) for  $H = 0.03$  and center point  $x_1 = 30$ , is a leading-depression  $N$ -wave (LDN) with identical depression and elevation heights. When translated to the hodograph space, Eq. (2.34) becomes

$$\eta_0(\sigma) = \frac{3\sqrt{3}}{2} H \operatorname{sech}^2 \gamma_i (\sigma^2 - \sigma_1^2) \tanh \gamma_i (\sigma^2 - \sigma_1^2). \quad (2.35)$$

The temporal variations of the shoreline wave height and the wave velocity of the isosceles  $N$ -wave are plotted in Figures 2.8(e,f), respectively. As seen from Table 2.2 (case 2), the initial wave having velocity creates approximately two times the maximum shoreline wave height compared to the wave without initial velocity.

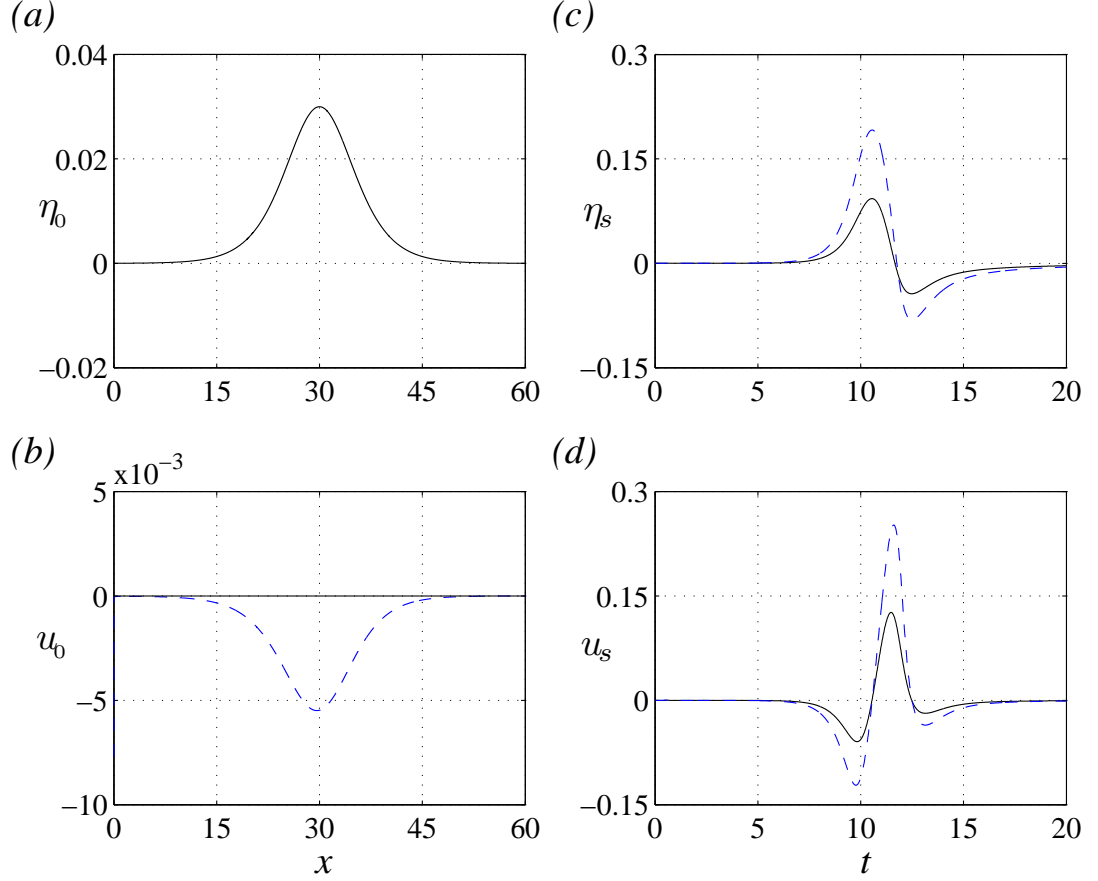


Figure 2.7: (a) The solitary wave with initial height  $H = 0.03$  located at  $x_1 = 30$ ; (b) the associated initial velocity distribution,  $u_0(x)$ . The corresponding temporal variations of the shoreline wave height  $\eta_s$  and the shoreline wave velocity  $u_s$  are presented in insets (c) and (d), respectively. Solid and dashed lines represent the cases  $u_0(x) \equiv 0$  and  $u_0(x) = 2\sqrt{x} - 2\sqrt{x + \eta_0(x)}$ , respectively.

#### 2.2.4 Generalized $N$ -wave

The other dipolar profile defined by Tadeipalli and Synolakis (1994), which produces uneven positive and negative disturbances, is the so-called generalized  $N$ -wave profile,

$$\eta_0(x) = \varepsilon H (x - x_2) \operatorname{sech}^2 \gamma_g (x - x_1), \quad (2.36)$$

with  $\gamma_g = \sqrt{3H/4}$ .  $\varepsilon$  is a scaling parameter which is used to ensure that the initial height of the wave is  $H$ . Eq. (2.36) is translated to the hodograph space as

$$\eta_0(\sigma) = H (\sigma^2 - \sigma_2^2) \operatorname{sech}^2 \gamma_g (\sigma^2 - \sigma_1^2). \quad (2.37)$$

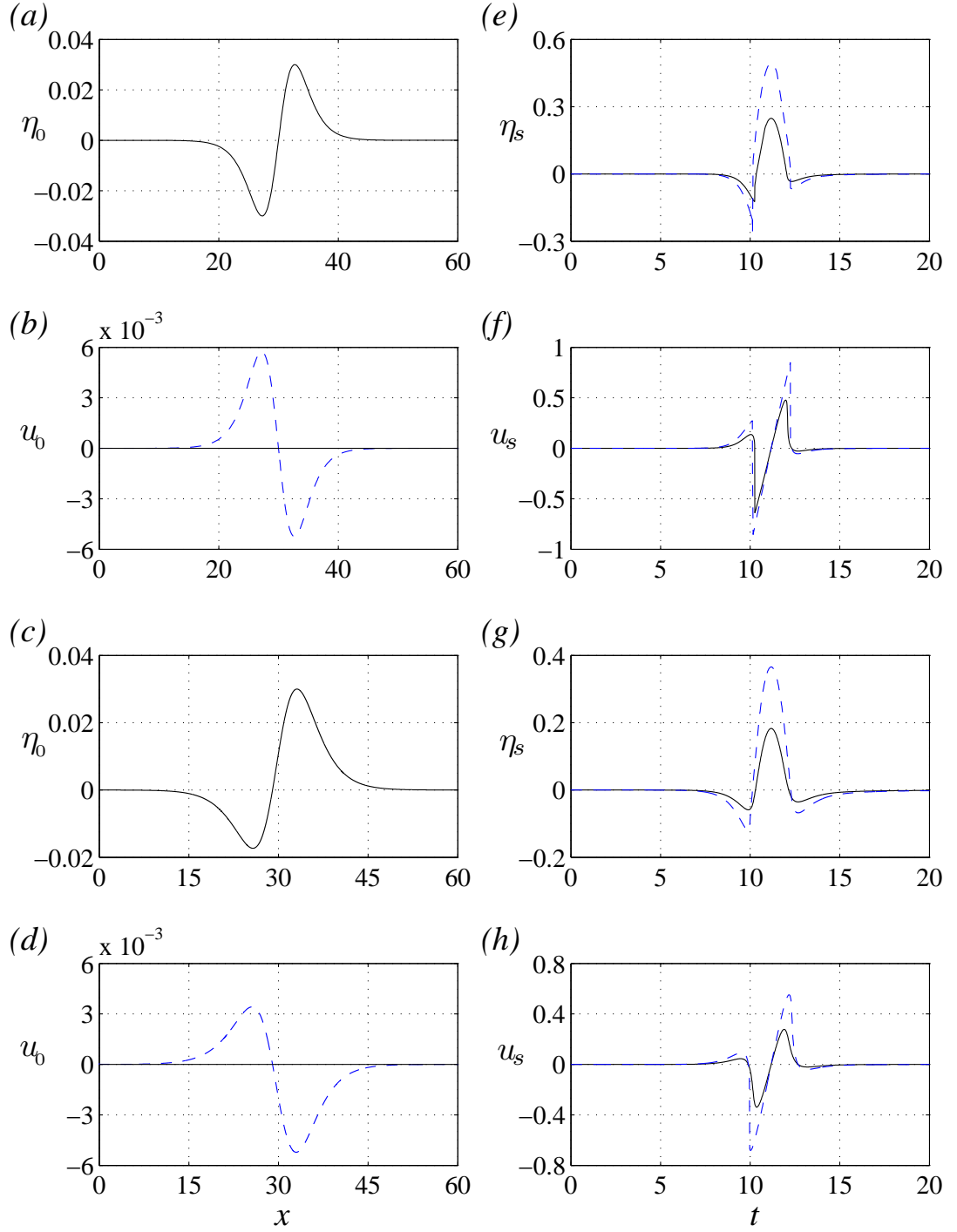


Figure 2.8: (a) The isosceles  $N$ -wave profile with  $H = 0.03$  and  $x_1 = 30$ ; (b) the associated initial velocity distribution,  $u_0(x)$ . The corresponding temporal variations of the shoreline wave height  $\eta_s$  and the shoreline wave velocity  $u_s$  are presented in insets (e) and (f), respectively. (c) The generalized  $N$ -wave profile with  $H = 0.06$ ,  $x_1 = 30$ , and  $x_2 = 29$ . The scaling parameter is chosen as  $\varepsilon = 0.1827$  so that the wave has a maximum initial height of 0.03. (d) The associated initial velocity distribution,  $u_0(x)$ . The corresponding temporal variations for  $\eta_s$  and  $u_s$  are presented in insets (g) and (h), respectively. Solid and dashed lines represent the cases  $u_0(x) \equiv 0$  and  $u_0(x) = 2\sqrt{x} - 2\sqrt{x + \eta_0(x)}$ , respectively.

Table 2.2: The corresponding parameters of Eqs. (2.32), (2.34), and (2.36) for which calculations are performed. The extreme wave height values for the cases with/without initial velocity are also tabulated. The exact initial velocity relation is considered in the calculations.

					Maximum runup / minimum rundown			
Wave parameters					without velocity		with velocity	
Case	$H$	$x_1$	$x_2$		$\eta_{max}$	$\eta_{min}$	$\eta_{max}$	$\eta_{min}$
1 Figure 2.7(a)	0.03	30.0	-		0.0930	-0.0437	0.1916	-0.0813
2 Figure 2.8(a)	0.03	30.0	-		0.2480	-0.1234	0.4939	-0.2659
3 Figure 2.8(c)	0.06	30.0	29.0		0.1829	-0.0589	0.3658	-0.1207

An LDN with parameters  $H = 0.06$ ,  $x_1 = 30$ , and  $x_2 = 29$  is given in Figure 2.8(c) for reference. The scaling parameter is chosen as  $\varepsilon = 0.1827$  so that the wave has a maximum initial height of 0.03. The temporal variations of the shoreline wave height and the wave velocity for Eq. (2.36) are given in Figures 2.8(g,h), respectively. The same effect of the initial velocity on the maximum wave height at the shoreline as in the solitary and isosceles  $N$ -wave cases can also be observed for the generalized  $N$ -wave (Table 2.2, case 3).

### 2.2.5 Application to near-shore earthquakes

Tinti and Tonini (2005) obtained an analytical solution for propagation and runup of long waves resulting from earthquakes that occur in the vicinity of the initial shoreline. They solved the NSW equations as an IVP after utilizing the hodograph and the Hankel integral transformations. Tinti and Tonini (2005) assumed zero initial velocity and an initial wave of the form

$$\eta_0(\sigma) = \sum_{k=0}^3 c_k (1 + \sigma^2)^{-(k+3/2)}, \quad (2.38)$$

in the hodograph space. First, they calculated the initial sea surface vertical displacement for a coastal earthquake with prescribed parameters from Okada's dislocation model (Okada, 1985, 1992). Then, they approximated the surface profile with Eq. (2.38) and computed the coefficients  $c_k$  using curve fitting.



Table 2.3: The corresponding parameters of Eq. (2.38) for which calculations are performed. The parameter set is taken from Tinti and Tonini (2005).

	Case	$c_0$	$c_1$	$c_2$	$c_3$
1	Figure 2.9	$2.00\text{e} - 03$	$-2.10\text{e} - 03$	$5.53\text{e} - 07$	$1.75\text{e} - 07$
2	Figure 2.10	$9.98\text{e} - 04$	$6.60\text{e} - 03$	$-1.58\text{e} - 02$	$8.20\text{e} - 03$
3	Figure 2.11	$7.40\text{e} - 04$	$9.60\text{e} - 03$	$-2.23\text{e} - 02$	$1.17\text{e} - 02$
4	Figure 2.12	$7.10\text{e} - 03$	$-1.44\text{e} - 02$	$2.80\text{e} - 04$	$6.90\text{e} - 03$

Tinti and Tonini (2005) produced spatial and temporal distributions for the subsequent waves in the form of Eq. (2.38), initiated from four different near-shore earthquake configurations. The first three configurations correspond to displacements from vertical dip-slip faults that are located inland (case 1), under the shoreline (case 2), and slightly offshore (case 3). The last configuration (case 4) is associated with a fault system consisting of oblique inverse and normal faults. The details can be found in Tinti and Tonini (2005). The parameter set for each case is taken from Tinti and Tonini (2005) and tabulated in Table 2.3. In Figures 2.9-2.12, the results of Tinti and Tonini (2005) are reproduced and compared with the results of the method presented in Section 2.1. Exact agreement is observed.

### 2.3 Conclusions

The analytical solution developed here provides accurate estimate for temporal variations of shoreline wave height and velocity distributions of shallow-water waves propagating over a sloping beach. The general initial-boundary value problem of the NSW equations, i.e., with and without initial velocity, is considered and a wide class of initial wave profiles are analyzed.

The eigenfunction expansion method presented here appears simpler than existing solution methods; unlike previous integral transform techniques, the present method does not involve evaluation of singular elliptic integrals and hence, it requires minimum computational effort. The method can serve as an analytical benchmark solution for numerical solutions in addition to the ones presented in Synolakis et al. (2008).

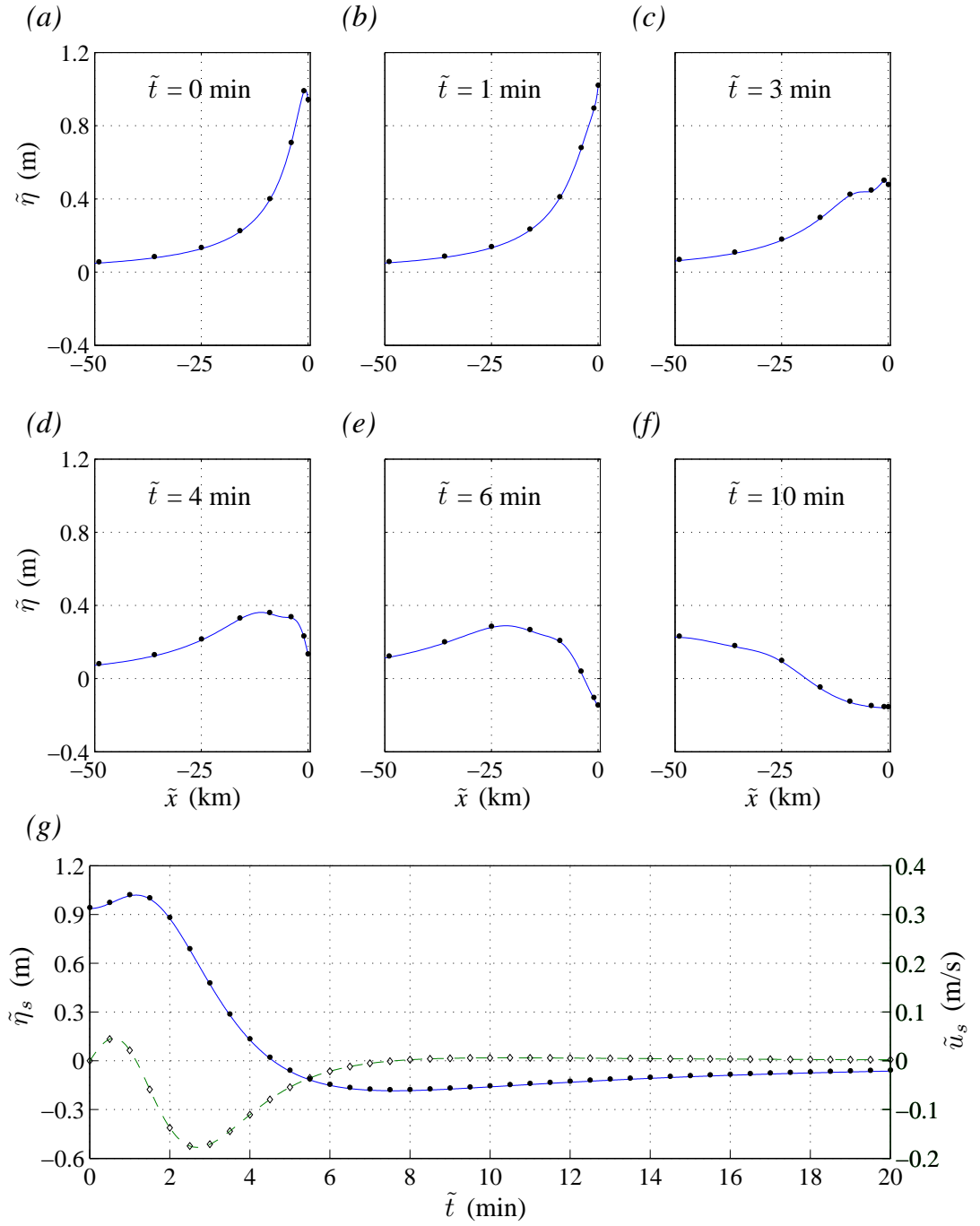


Figure 2.9: (a)-(f) Spatial variations of wave height for the case 1 of Tinti and Tonini (2005) at times  $\tilde{t} = 0, 1, 3, 4, 6$ , and 10 minutes. (g) Time variations of the shoreline position (solid line) and shoreline velocity (dashed line). Markers represent results of Tinti and Tonini (2005). Dimensional quantities are calculated and plotted using a characteristic length of  $l^* = 50 \text{ km}$  and a beach slope of  $\tan \beta = 1/25$  as in Tinti and Tonini (2005), so that the characteristic depth becomes  $l^* \tan \beta = 2000 \text{ m}$ .

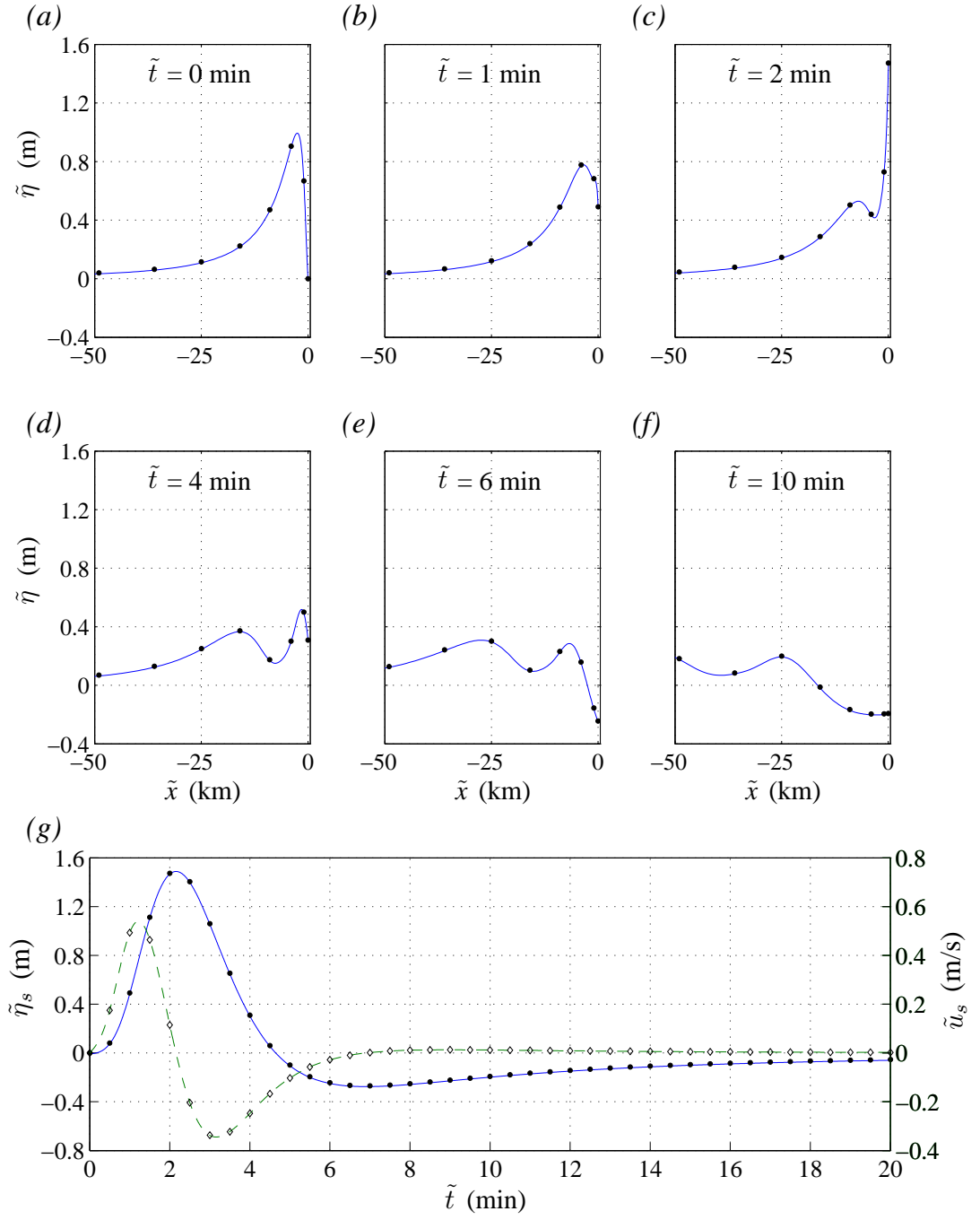


Figure 2.10: (a)-(f) Spatial variations of wave height for the case 2 of Tinti and Tonini (2005) at times  $\tilde{t} = 0, 1, 2, 4, 6$ , and 10 minutes. (g) Time variations of the shoreline position (solid line) and shoreline velocity (dashed line). Markers represent results of Tinti and Tonini (2005). Dimensional quantities are calculated and plotted using a characteristic length of  $l^* = 50 \text{ km}$  and a beach slope of  $\tan\beta = 1/25$  as in Tinti and Tonini (2005), so that the characteristic depth becomes  $l^* \tan\beta = 2000 \text{ m}$ .

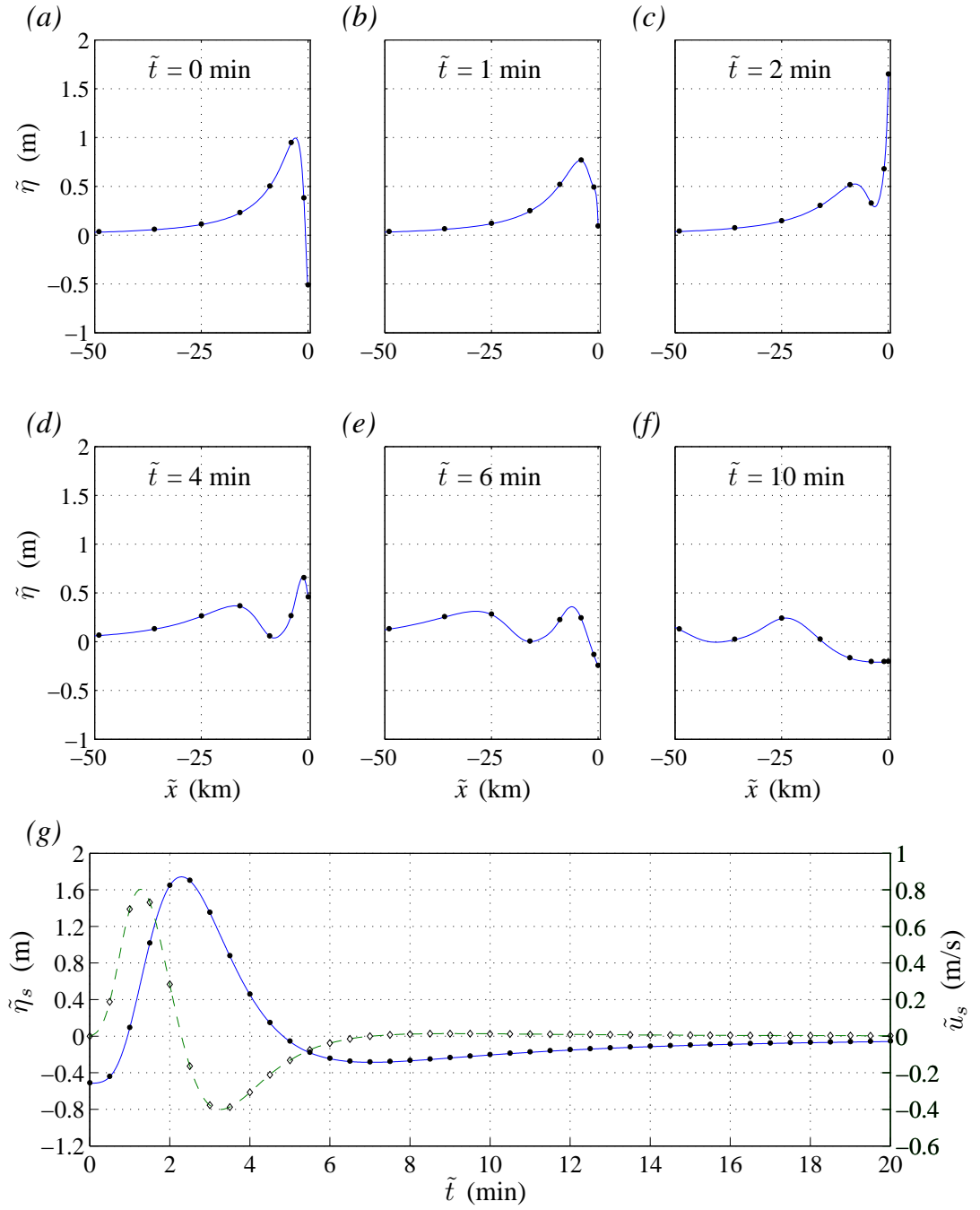


Figure 2.11: (a)-(f) Spatial variations of wave height for the case 3 of Tinti and Tonini (2005) at times  $\tilde{t} = 0, 1, 2, 4, 6$ , and  $10$  minutes. (g) Time variations of the shoreline position (solid line) and shoreline velocity (dashed line). Markers represent results of Tinti and Tonini (2005). Dimensional quantities are calculated and plotted using a characteristic length of  $l^* = 50 \text{ km}$  and a beach slope of  $\tan\beta = 1/25$  as in Tinti and Tonini (2005), so that the characteristic depth becomes  $l^* \tan\beta = 2000 \text{ m}$ .

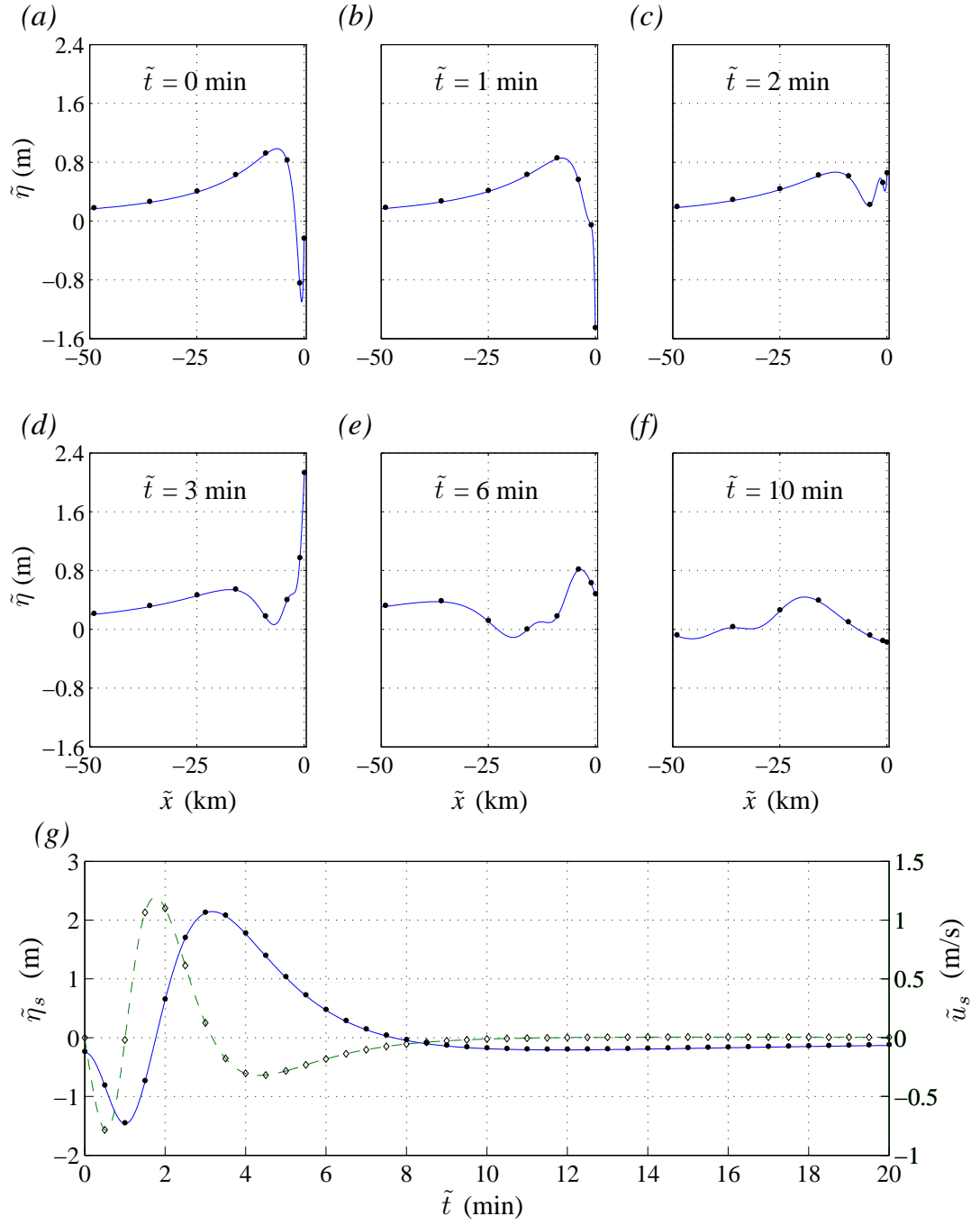


Figure 2.12: (a)-(f) Spatial variations of wave height for the case 4 of Tinti and Tonini (2005) at times  $\tilde{t} = 0, 1, 2, 3, 6$ , and 10 minutes. (g) Time variations of the shoreline position (solid line) and shoreline velocity (dashed line). Markers represent results of Tinti and Tonini (2005). Dimensional quantities are calculated and plotted using a characteristic length of  $l^* = 50 \text{ km}$  and a beach slope of  $\tan\beta = 1/25$  as in Tinti and Tonini (2005), so that the characteristic depth becomes  $l^* \tan\beta = 2000 \text{ m}$ .

## CHAPTER 3

### WIND SET-DOWN RELAXATION<sup>1</sup>

In Chapter 2, a solution technique utilizing the hodograph transformation is introduced for modeling of nonlinear shallow-water wave propagation over a beach having constant slope. As a coastal engineering application of this technique, in this chapter, the subsequent wave motion resulted by the relaxation of wind stress along a long-narrow basin is modeled analytically. The Gulf of Suez, Gulf of Elat (also known as the Gulf of Aqaba) or Baja California are examples of a such basin. Examination of their geometry suggests neglect of the wave dynamics in the cross-basin direction as well as the Coriolis force (Csanady, 1982).

In the presence of a moderate wind blowing in the seaward direction, the sea surface over the basin will assume a steady-state shape resulted by the balance of the wind stress at the top of the water column with the vertical pressure gradient. This is called the wind set-down. This sea surface state is preserved as long as the wind blows in the same direction. If the wind suddenly calms down, however, water accelerates in the shoreward direction under the pressure gradient since the wind stress is zero now, and water shows oscillatory behavior. This is the relaxation of the wind set-down.

Nof and Paldor (1992) solved the wind set-down problem governed by the balance described above and found an implicit analytical solution to this steady-state problem. They applied their solution to the Gulf of Suez at the northern end of the Red Sea. Later, Gelb et al. (1997) used the implicit analytical solution developed by Nof and Paldor (1992) as an initial condition for the nonlinear shallow-water wave (NSW) equations and they modeled the wind set-down relaxation problem numerically using

---

<sup>1</sup> The results presented in this chapter is published in Aydın and Kânoğlu (2007).

Chebyshev spectral and MacCormack finite-difference methods. The main difficulty in solving this problem is reported to be the moving singularity at the shoreline (Gelb et al., 1997).

Here, both the wind set-down and the wind set-down relaxation problems are solved analytically. The solution methodology yields an initial-boundary value problem (IBVP), even though long wave propagation problems are usually treated as initial- or boundary-value problems. First, the steady-state wind set-down problem is solved explicitly, employing the hodograph transformation for the spatial variable (Carrier et al., 2003). Then, the temporal transformation is incorporated into the solution in order to offer an analytical solution for the relaxation problem. At this stage, the NSW equations are reduced into a single second-order linear partial differential equation, as usually is the case for the hodograph transformation. It is observed that the application of the standard separation of variables technique to the final (reduced) equation yields a solution in the form of a Fourier-Bessel series, as in Chapter 2. The coefficients of the series are computed by imposing the wind set-down solution as an initial condition. After obtaining the complete solution in the transform space, the transformation is inverted for the physical space to evaluate physical quantities such as free-surface elevation and water velocity.

### 3.1 Mathematical Model

#### 3.1.1 The steady-state phase

Nonlinear response of the ocean to the wind blowing over a long-narrow basin (Figure 3.1) is governed by the nondimensional nonlinear equation (Csanady, 1982)

$$-(h + \eta) \frac{d\eta}{dx} + \gamma = 0. \quad (3.1)$$

in steady-state. Here  $h(x) = x$  and  $\eta = \eta(x)$  represent the undisturbed water of variable depth and the free-surface elevation, respectively. The origin of the coordinate system is chosen to be at the initial shoreline, with  $0 \leq x \leq 1$ , increasing in the seaward direction. Nondimensional variables in Eq. (3.1) are introduced as

$$x = \frac{\tilde{x}}{\tilde{L}}, \quad (h, \eta) = \frac{(\tilde{h}, \tilde{\eta})}{\tilde{D}}, \quad \gamma = \frac{\tilde{L}}{\tilde{D}^2} \frac{\tilde{\tau}_x}{g\tilde{\rho}_w}, \quad (3.2)$$

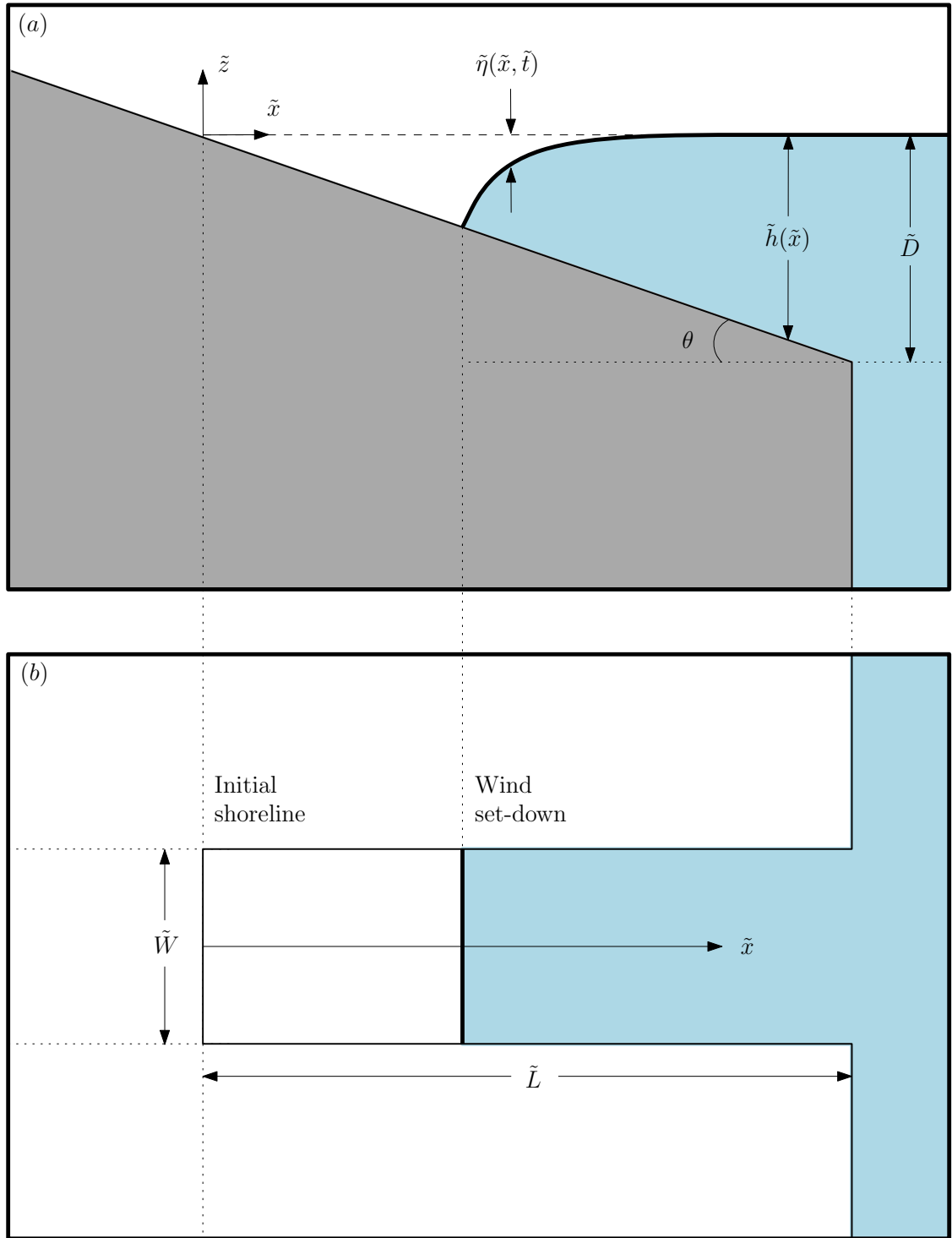


Figure 3.1: Definition sketch for a long-narrow ( $\tilde{W}/\tilde{L} \ll 1$ ) and shallow ( $\tilde{D}/\tilde{L} \ll 1$ ) basin: (a) cross section, (b) top view.



quantities with tilde being dimensional. Here, the length of the basin  $\tilde{L}$  and the depth at the toe of the slope  $\tilde{D}$  are chosen as the respective characteristic length and depth scales.  $\tilde{\tau}_x$ ,  $\tilde{\rho}_w$ , and  $g$  are the horizontal stress component induced by the wind, the density of the water, and the gravitational acceleration, respectively. Eq. (3.1) is subjected to the boundary condition

$$\eta(x = 1) = 0, \quad (3.3)$$

i.e., the wave height is zero at the mouth of the basin. The governing equation (3.1) is inverted by Nof and Paldor (1992) for  $dx/d\eta$ . This inversion converts the nonlinear governing equation in  $\eta(x)$  to a linear equation in  $x(\eta)$ . Nof and Paldor (1992) solved the resultant linear equation under the boundary condition (3.3) and determined the initial sea surface height  $\eta(x)$  implicitly. Their solution can be rearranged into the form

$$x = \eta(x) + (1 + \gamma)[1 - \exp(\frac{\eta(x)}{\gamma})], \quad (3.4)$$

which requires nonlinear iterations to obtain  $\eta(x)$ .

Using the wind set-down solution (3.4) as an initial condition, Gelb et al. (1997) solved the wind set-down relaxation problem numerically through spectral and finite-difference schemes. The implicit form of Eq. (3.4) does not possess a problem with the numerical solution. However, nonexistence of an explicit analytical solution for the wind set-down problem prevents proceeding with an analytical solution for the relaxation problem. Here, it is shown that an explicit solution of the steady-state problem is possible with application of the hodograph transformation to Eq. (3.1), which will allow analytical modeling of the relaxation problem.

The governing equation, Eq. (3.1), takes the form

$$(\sigma^2 + \gamma)\eta_\sigma - 2\gamma\sigma = 0, \quad (3.5)$$

in the hodograph transform space, after using the transformation for the spatial variable  $x$  as suggested by Carrier et al. (2003) to solve the NSW equations, i.e.,

$$x = \sigma^2 - \eta. \quad (3.6)$$

The boundary condition (3.3) can be translated into the following condition

$$\eta(\sigma = 1) = 0. \quad (3.7)$$

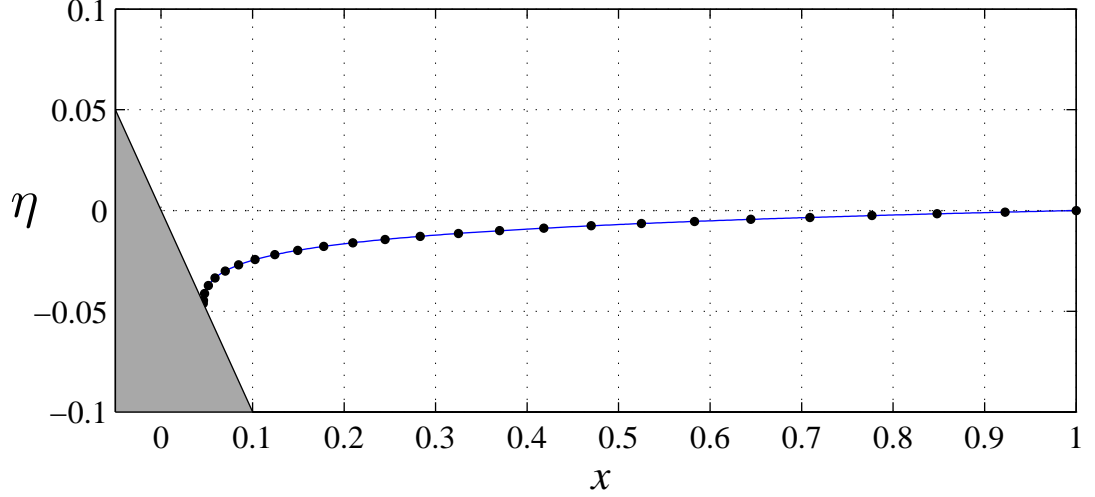


Figure 3.2: The steady-state wind set-down solution for  $\gamma = 0.01$ . Dots and solid line represent the explicit analytical solution, i.e., Eq. (3.8) versus Eq. (3.6), and the implicit analytical solution of Nof and Paldor (1992), respectively.

The transform governing equation (3.5) has the following exact solution together with the boundary condition (3.7);

$$\eta(\sigma) = \gamma \ln\left(\frac{\sigma^2 + \gamma}{1 + \gamma}\right). \quad (3.8)$$

Eq. (3.8) is an explicit transform solution for the steady-state wind set-down problem in terms of transform variable  $\sigma$ . It is straightforward to obtain the solution in the physical space using the combination of Eqs. (3.6) and (3.8); Eq. (3.8) can be evaluated for a specific  $\sigma$  to find  $\eta(\sigma)$  and resultant  $\eta(\sigma)$  together with  $\sigma$  give corresponding  $x$  through Eq. (3.6). One example of such solution is presented in Figure 3.2 for  $\gamma = 0.01$ . As seen in Figure 3.2, even though equal increments are chosen for  $\sigma$  in the hodograph transform space, conversion to the physical space generates unequal increments for  $x$  because of the nonlinear transformation given in Eq. (3.6).

### 3.1.2 Wind set-down relaxation

Once wind calms down, water accelerates under the pressure gradient since there is no balancing wind stress. It will be physically interesting to obtain the characteristics of the motion, especially shoreline motion, after the wind calms down. The NSW

equations defined in Chapter 2 can be used to describe the dynamics of the subsequent motion,

$$\eta_t + [(h + \eta)u]_x = 0, \quad (3.9a)$$

$$u_t + uu_x + \eta_x = 0. \quad (3.9b)$$

Once again, in Eqs. (3.9),  $\eta(x, t)$  represents the surface height above still water level and  $u(x, t)$  is the depth-averaged water velocity. Also,  $h(x)$  is the undisturbed water depth, as in the wind set-down problem (Figure 3.1).

Nondimensional variables are defined as in Eq. (3.2), with additional nondimensionalizations for the time and velocity variables,

$$t = \frac{\tilde{t} \sqrt{g\tilde{D}}}{\tilde{L}}, \quad u = \frac{\tilde{u}}{\sqrt{g\tilde{D}}}. \quad (3.10)$$

In order to solve Eqs. (3.9), the transformation for the spatial variable given in Eq. (3.6) is complemented with the transformation for the temporal variable,

$$t = \lambda + u, \quad (3.11)$$

(Carrier et al., 2003). Based on transformations (3.6) and (3.11), the system (3.9) is transformed into

$$(\sigma^2 u)_\sigma + 2\sigma \left( \eta + \frac{1}{2} u^2 \right)_\lambda = 0, \quad (3.12a)$$

$$2\sigma u_\lambda + \left( \eta + \frac{1}{2} u^2 \right)_\sigma = 0. \quad (3.12b)$$

Further, defining a potential function  $\varphi(\sigma, \lambda)$  as

$$\varphi = \eta + \frac{1}{2} u^2, \quad (3.13)$$

Eqs. (3.12) can be reduced into the following single second-order linear partial differential equation for  $\varphi$ , eliminating  $u$ ;

$$4\sigma \varphi_{\lambda\lambda} - (\sigma \varphi_\sigma)_\sigma = 0. \quad (3.14)$$

As described in Chapter 2, nonlinear hodograph transformation not only reduces the NSW equations into a single second-order linear partial differential equation, but also the moving shoreline is fixed to  $\sigma = 0$  in the transform space.

Now, the solution strategy introduced in Chapter 2 will be utilized and Eq. (3.14) will be solved as an IBVP. The initial conditions are the steady-state wind set-down solution (3.8), as the initial surface profile  $\eta(\sigma, 0)$ , with corresponding zero initial velocity,  $u(\sigma, 0) \equiv 0$ . Then, the following initial conditions in terms of the potential function  $\varphi$  can be derived through Eqs. (3.12a) and (3.13), respectively;

$$\varphi_\lambda(\sigma, 0) = 0, \quad (3.15a)$$

$$\varphi(\sigma, 0) = \eta(\sigma, 0). \quad (3.15b)$$

In addition to these initial conditions, bounded solution requires  $\varphi(\sigma, \lambda)$  to have a finite value at the shoreline ( $\sigma = 0$ ) and undisturbed sea surface at the toe of the slope,  $\eta(x = 1, t) = 0$ , implies that  $\eta(\sigma = 1, \lambda) = 0$  in the transform  $(\sigma, \lambda)$ -space. The importance of the requirement of an explicit solution  $\eta(\sigma, 0)$  for the steady-state wind set-down problem is now clear to proceed with the solution of the NSW equations.

After defining proper initial and boundary conditions in the transform  $(\sigma, \lambda)$ -space, the solution for Eq. (3.14) is now straightforward. The separation of variables technique introduced in Chapter 2 yields the Fourier-Bessel series given as

$$\varphi(\sigma, \lambda) = \sum_{n=1}^{\infty} K_n J_0(z_n \sigma) \cos\left(\frac{z_n}{2} \lambda\right), \quad (3.16)$$

where  $z_n$  are the positive zeros of the Bessel function of the first kind of order zero. The coefficients  $K_n$  will be determined by applying the steady-state wind set-down solution (3.8) as an initial condition for Eq. (3.14). Considering Eq. (3.15b) and Eq. (3.16), the initial condition can be written as

$$\sum_{n=1}^{\infty} K_n J_0(z_n \sigma) = \gamma \ln\left(\frac{\sigma^2 + \gamma}{1 + \gamma}\right), \quad (3.17)$$

where  $K_n$  are the Bessel coefficients. Multiplication of both sides with  $\sigma J_0(z_m \sigma)$  and integration from  $\sigma = 0$  to  $\sigma = 1$  gives (Watson, 1944)

$$K_n = \frac{2\gamma}{J_1^2(z_n)} \int_0^1 \sigma \ln\left(\frac{\sigma^2 + \gamma}{1 + \gamma}\right) J_0(z_n \sigma) d\sigma. \quad (3.18)$$

Finally, insertion of Eq. (3.18) into Eq. (3.16) gives the complete analytical solution for the wind set-down relaxation problem,

$$\varphi(\sigma, \lambda) = \sum_{n=1}^{\infty} \frac{2\gamma}{J_1^2(z_n)} \int_0^1 \omega \ln\left(\frac{\omega^2 + \gamma}{1 + \gamma}\right) J_0(z_n \omega) J_0(z_n \sigma) \cos\left(\frac{z_n}{2} \lambda\right) d\omega. \quad (3.19)$$

After obtaining the solution of the IBVP for the wind set-down relaxation problem, the whole flow field can now be resolved. Importance is given to the physical characteristics of shoreline motion.

Combination of Eq. (3.12a) with Eq. (3.16) can be used to compute the water velocity  $u(\sigma, \lambda)$  as

$$u(\sigma, \lambda) = \frac{1}{\sigma} \sum_{n=1}^{\infty} K_n J_1(z_n \sigma) \sin\left(\frac{z_n}{2} \lambda\right). \quad (3.20)$$

Once  $u(\sigma, \lambda)$  is known,  $\eta(x, t)$  can be evaluated through Eq. (3.13). Since  $\sigma = 0$  at the shoreline, Eq. (3.20) takes the form

$$u_s(\lambda) = u(0, \lambda) = \frac{1}{2} \sum_{n=1}^{\infty} z_n K_n \sin\left(\frac{z_n}{2} \lambda\right), \quad (3.21)$$

considering Eq. (2.21), i.e.,  $\lim_{\sigma \rightarrow 0} \frac{1}{\sigma} J_1(z_n \sigma) = \frac{1}{2} z_n$ . Shoreline position is now given as

$$x_s(\lambda) = x(0, \lambda) = \frac{u_s(\lambda)^2}{2} - \varphi(0, \lambda), \quad (3.22)$$

with respective time

$$t_s(\lambda) = t(0, \lambda) = \lambda + u_s(\lambda). \quad (3.23)$$

### 3.2 Results and Discussions

As an application of the solution developed in Section 3.1, the Gulf of Suez is considered as in Nof and Paldor (1992). The gulf has a basin length of  $\tilde{L} = 350 \text{ km}$  with a transition depth of  $\tilde{D} = 70 \text{ m}$ . A typical wind blowing with the speed  $7 \text{ m/s}$  gives a stress value of  $\tilde{\tau}_x/\tilde{\rho}_w = 10^{-4} \text{ m}^2/\text{s}^2$  for which  $\gamma = 7.28 \cdot 10^{-4}$  (Csanady, 1982; Nof and Paldor, 1992). On the other hand, an interval of  $0.01 \leq \gamma \leq 0.02$  is suggested in Gelb et al. (1997) for the nondimensional parameter  $\gamma$ . Since it gives a chance of comparison between the proposed analytical solution and the existing numerical solution of Gelb et al. (1997), the value  $\gamma = 0.01$  is used for evaluation of some physical properties of the relaxation problem.<sup>2</sup>

The wave profile at some specific time values  $t^*$  is obtained using the Newton-Raphson iterations, which is proposed by Synolakis (1987) and recently used by Kânoğlu

---

<sup>2</sup> Although not clearly stated in their paper, it is verified here that Gelb et al. (1997) performed the calculations for  $\gamma = 0.01$  corresponding to the wind stress  $\tilde{\tau}_x/\tilde{\rho}_w = 1.37 \cdot 10^{-3} \text{ m}^2/\text{s}^2$ .

(2004). The recursive relation

$$\lambda_{i+1} = \lambda_i - \frac{t^* - t(\sigma, \lambda_i)}{1 + u_\lambda(\sigma, \lambda_i)}, \quad (3.24)$$

determines the value  $\lambda^*$  for which  $t(\sigma, \lambda^*) - t^* = 0$ . A number of spatial distributions of the water surface elevation and the depth-averaged velocity for different values of  $t^*$  are given in Figures 3.3(a,b), respectively. The same procedure can be utilized to get the solution at a specific location  $x^*$  as well (Synolakis, 1987).

Shoreline position is presented in Figure 3.4(a) and it exactly compares with Gelb et al. (1997). Gelb et al. (1997) further analyzed the oscillatory behavior of the shoreline position with the help of the power spectral density. Power spectral density is defined by  $d_k = |f_k|^2$  where  $f_k$  is the discrete Fourier transform of the time averaged shoreline position data,

$$f_k = \sum_{j=0}^{N-1} (\eta_{s,j} - \eta_{s,\text{average}}) e^{-i2\pi jk/N}; \quad k = 0, 1, \dots, N-1. \quad (3.25)$$

The corresponding nondimensional frequency is  $k/N\Delta t$  with  $\Delta t = T/N$  ( $N = 2^m$ ,  $m$  being a positive integer, and  $T$  is the total time). Exact agreement with Gelb et al. (1997) is obtained as presented in Figure 3.4(b).

### 3.3 Conclusions

The governing equation for the wind set-down problem is first transformed by using the hodograph transformation for the spatial variable and an explicit analytical solution is obtained. This explicit solution is crucial to proceed with the analytical solution of the wind set-down relaxation problem since the existing steady-state solution was an implicit one. Then, the hodograph transformation is complemented with the transformation for the temporal variable in order to reduce the NSW equations, which govern the relaxation phase, into a single second-order linear partial differential equation. An IBVP solution rather than the existing IVP and BVP solutions is presented for the reduced linear equation as in Chapter 2. The nonhomogeneous initial condition is extracted from the wind set-down solution. Certain physical flow-field properties such as wave heights and velocities at specific times as well as the

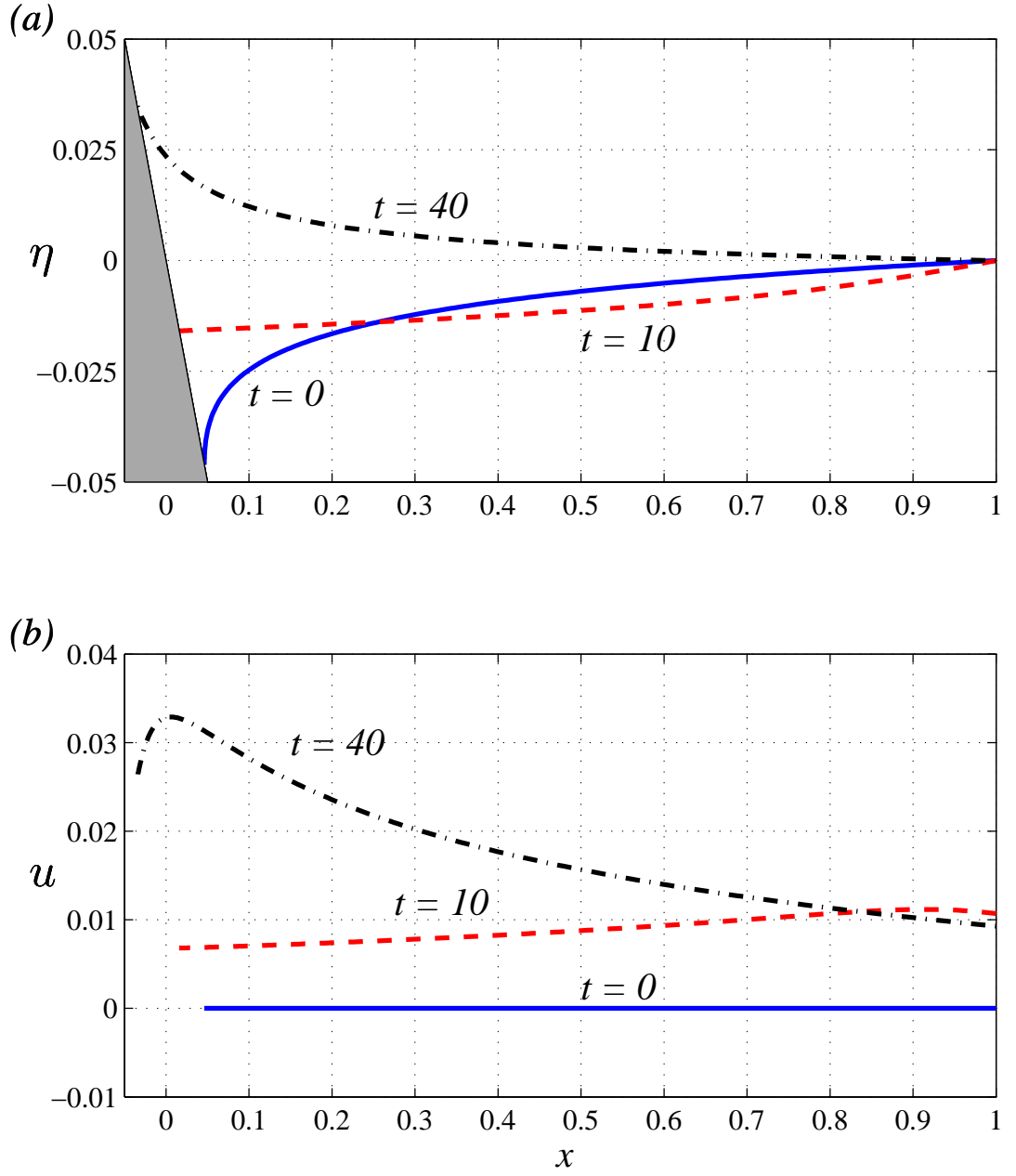


Figure 3.3: Spatial and temporal variation of (a) the free-surface elevation and (b) the velocity at  $t = 0$  (solid line),  $t = 10$  (dashed line), and  $t = 40$  (dash-dotted line) for  $\gamma = 0.01$ . Insets (a) and (b) correspond to the Figure 8 for  $t^* = 10$  and to the Figure 9 for  $t^* = 40$  of Gelb et al. (1997), respectively.

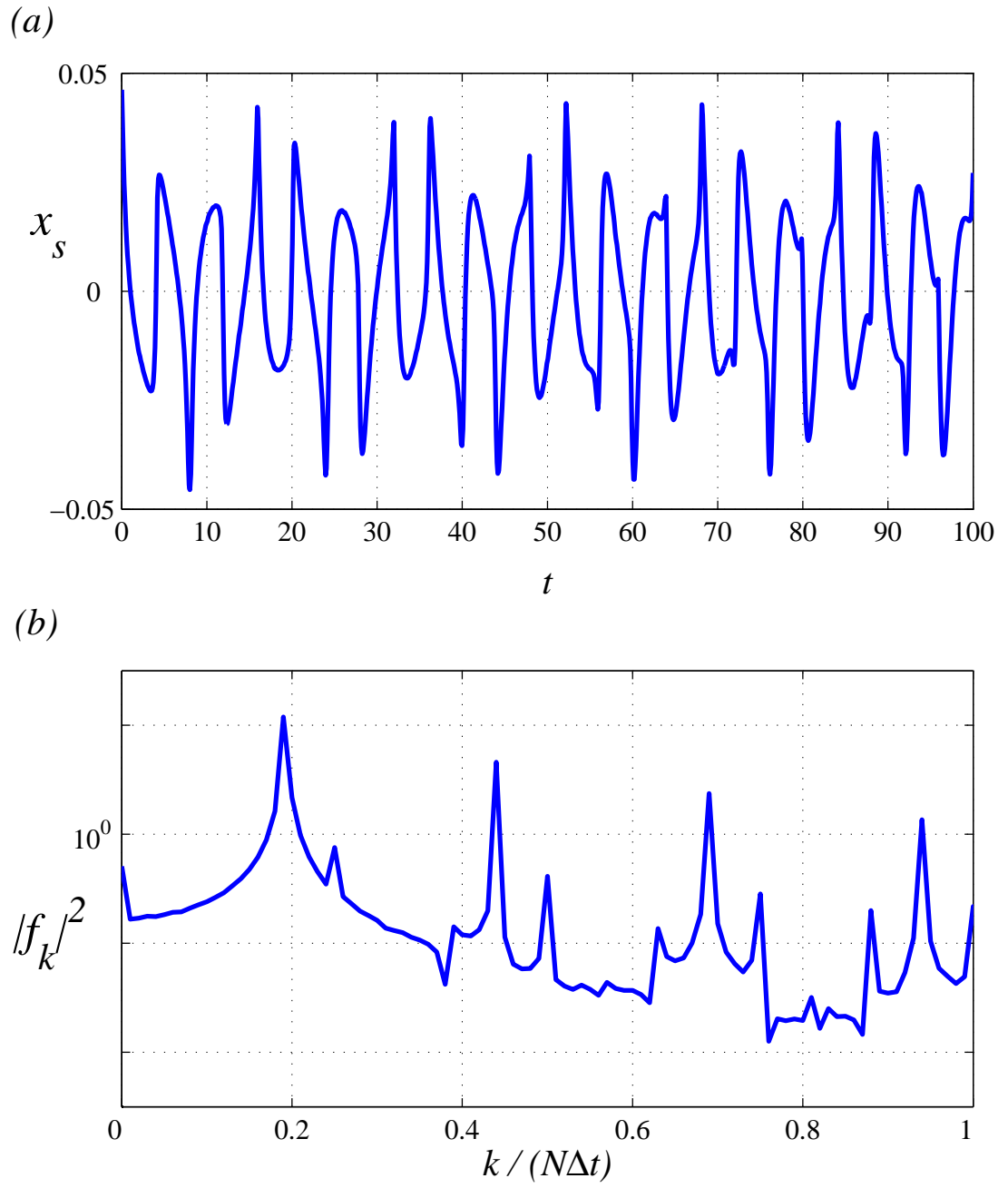


Figure 3.4: (a) Temporal variation and (b) power spectral density of the shoreline position  $x_s$  for  $\gamma = 0.01$ . Note that  $x_s = -\eta_s$ . Insets (a) and (b) correspond to the Figures 3 and 4 of Gelb et al. (1997), respectively.



temporal variation of the free-surface and the depth-averaged velocity at the shoreline are evaluated. The results are compared with the numerical solution of Gelb et al. (1997) and exact agreement is obtained.

## CHAPTER 4

### PROPAGATION OF A FINITE SOURCE OVER A FLAT BASIN<sup>1</sup>

Once generated, tsunamis evolve substantially through two-dimensional spatial spreading as they propagate over ocean bathymetry. Titov et al. (2005) revealed wave amplitudes, directionality, and global propagation patterns of the 26 December 2004 tsunami. They presented a global figure showing energy propagation –maximum wave height observed at each computational grid point– of the 2004 Indian Ocean tsunami calculated from the Method of Splitting Tsunamis (MOST) model (Titov, 1997; Titov and Synolakis, 1995, 1996, 1998), which was validated through extensive series of benchmark analytical solutions, experimental results, and field observations identified by Synolakis et al. (2008). Titov et al. (2005) observed two main factors affecting tsunami wave directionality: the focusing configuration of the source region (Marchuk and Titov, 1989) and the waveguide structure of mid-ocean ridges (Koshimura et al., 1999). Continental shelves also act as waveguides (González et al., 1995) and are apparently responsible for alongshore propagation and persistent ringing for the Pacific coasts of South and North America.

Tsunami initiated from an underwater earthquake has a finite-crest (strip) length where boundaries of the displaced portion of the crust can roughly be estimated from the parent earthquake parameters (Okada, 1985). The spatial and temporal evolution of the finger-like pattern radiated from a tsunami source of finite length is referred to as its directivity. Ben-Menahem (1961) recognized it and defined a directivity function generated by the source length and the rupture velocity. Later, Ben-Menahem

---

<sup>1</sup> The results presented in this chapter is in the process of submission as a journal article (Kânoğlu et al., in preparation).

and Rosenman (1972) used the linear theory to calculate the two-directional radiation pattern from a moving source. They showed that tsunami energy radiates primarily at a right angle to a rupturing fault. They also verified dependence of directivity on the sea-floor rupture and wave celerity and they applied their theory to sample the path of the 1964 Great Chilean tsunami. Okal (2003a) discussed the details of the analysis of Ben-Menahem (1961) and the distinct difference between the directivity patterns of earthquake- and landslide-generated tsunamis. Okal (2003a) then considered the field observation of the 1946 Aleutian earthquake and tsunami and concluded that a large slow earthquake and a landslide must have occurred concurrently to yield the far-field distribution of the reported runup. One example of his work is presented in Synolakis and Bernard (2006) for the 2004 Indian Ocean tsunami. Okal (2005, personal communication) quickly eliminated the shorter earthquake source proposed in the immediate aftermath of the 2004 tsunami, in favor of the larger source, based on qualitative assessment of the radiation field on the basis of the directivity of the source.

In addition to the two-dimensional analytical shallow-water wave models summarized in Chapter 1, Kervella et al. (2007) numerically compared propagation of initial waveforms resulted from two different generation mechanisms, i.e., the sea-floor deformation is directly translated to the ocean surface (passive approach) and the time scale of the sea-floor deformation is taken into account (active approach). They showed that both generation mechanisms do not always produce equivalent far-field waveforms. Berry (2007) showed that shallower regions in the oceans can focus the energy of tsunamis and could make tsunamis more destructive where focal regions include sections of coasts.

One of the two-dimensional models introduced in Chapter 1 was the analytical solution of Carrier and Yeh (2005) for propagation and directivity of finite-crest length sources over a flat bathymetry, based on Carrier (1990)'s methodology. However, Carrier and Yeh (2005)'s solution has two drawbacks. One, their solution involves computation of elliptic integrals, as in Carrier et al. (2003). Elliptic integrals have singularities; therefore, Carrier and Yeh (2005) were not able to evaluate the solution integrals for the far-field. In order not to conserve the difficulty, they developed an approximate solution using the self-similar behavior of the solution, as briefly explained

in Section 4.3.1. Two, the analytical model proposed by Carrier and Yeh (2005) is restrictive on the initial waveform, i.e., it can only be used to analyze finite-crested wave profiles defined through a Gaussian (exponential) shape. However, plus-minus sources, i.e., sources having both depression (negative displacement) and elevation (positive displacement), are accepted as more realistic initial waveforms for tsunamis (Tadepalli and Synolakis (1994) presented a paradigm change from solitary wave to *N*-wave as discussed in Chapter 1). Even though solution for a plus-minus wave can be obtained by combining positive and negative Gaussian waves, the difficulties mentioned above will persist. Therefore, analytical solution of Carrier and Yeh (2005) is not general and generalization to more realistic waveforms is not straightforward since it includes ad-hoc approximation.

Marchuk and Titov (1989) presented a study on the process of tsunami wave generation by rectangular plus-minus initial displacements numerically during the 1989 International Tsunami Symposium, Novosibirsk, Russia. They showed existence of a focusing point for a combined plus-minus initial ocean surface displacement where abnormal tsunami wave height can be registered.

In this chapter, the linear shallow-water wave (LSW) equation will be solved for an initial wave having finite transverse crest length. First, a new general analytical solution is developed for propagation of a finite-crest length source. The proposed solution is first applied to the cases presented by Carrier and Yeh (2005). Then, flexibility of the solution method in terms of initial wave profile is shown; initial profiles having different cross-sections, i.e., Gaussian, solitary, or *N*-wave, can be incorporated. Lastly, the analytical solution is applied to the cases of 17 July 1998 Papua New Guinea and the 17 July 2006 Java Island, Indonesia tsunamis to explain some extreme runup observations.

#### **4.1 General Analytical Solution**

The two-dimensional propagation problem over an ocean basin of constant depth  $d$  can be described by the LSW equation, given in terms of free-surface elevation  $\eta =$

$\eta(x, y, t)$  as

$$\eta_{tt} - \eta_{xx} - \eta_{yy} = 0, \quad (4.1)$$

in nondimensional form (Carrier and Noiseux, 1983). The nondimensional variables are introduced as

$$(x, y) = \frac{(\tilde{x}, \tilde{y})}{l_0}, \quad \eta = \frac{\tilde{\eta}}{d_0}, \quad t = \frac{\tilde{t}}{t_0}, \quad (4.2)$$

where  $l_0 = d_0 = d$  and  $t_0 = l_0 / \sqrt{g d_0} = \sqrt{d/g}$  are the characteristic length, depth, and time scales, respectively (Figure 4.1), and  $g$  is the gravitational acceleration.

The initial conditions of the propagation problem are prescribed initial surface profile with zero initial velocity;

$$\eta(x, y, 0) = \eta_0(x, y), \quad (4.3a)$$

$$\eta_t(x, y, 0) = 0. \quad (4.3b)$$

The governing equation (4.1) transforms into

$$\hat{\eta}_{tt} + (k^2 + l^2) \hat{\eta} = 0, \quad (4.4)$$

under the Fourier transform pair over the space variables  $(x, y)$ ,

$$\hat{\eta}(k, l, t) = \int_{-\infty}^{\infty} \int_{-\infty}^{\infty} \eta(x, y, t) e^{-i(kx+ly)} dx dy, \quad (4.5a)$$

$$\eta(x, y, t) = \frac{1}{(2\pi)^2} \int_{-\infty}^{\infty} \int_{-\infty}^{\infty} \hat{\eta}(k, l, t) e^{i(kx+ly)} dk dl, \quad (4.5b)$$

where  $k$  and  $l$  are the wave numbers in the  $x$ - and  $y$ -directions, respectively. Then, the initial conditions given in Eqs. (4.3) transform to

$$\hat{\eta}(k, l, 0) = \hat{\eta}_0(k, l), \quad (4.6a)$$

$$\hat{\eta}_t(k, l, 0) = 0. \quad (4.6b)$$

In the Fourier space, the solution of Eq. (4.4) under the conditions given in Eqs. (4.6) is now straightforward;

$$\hat{\eta}(k, l, t) = \hat{\eta}_0(k, l) \cos t \sqrt{k^2 + l^2}, \quad (4.7)$$

and the solution in the physical  $(x, y)$ -space is given through the back-transformation formula (4.5b) as

$$\eta(x, y, t) = \frac{1}{(2\pi)^2} \int_{-\infty}^{\infty} \int_{-\infty}^{\infty} \hat{\eta}_0(k, l) e^{i(kx+ly)} \cos t \sqrt{k^2 + l^2} dk dl. \quad (4.8)$$

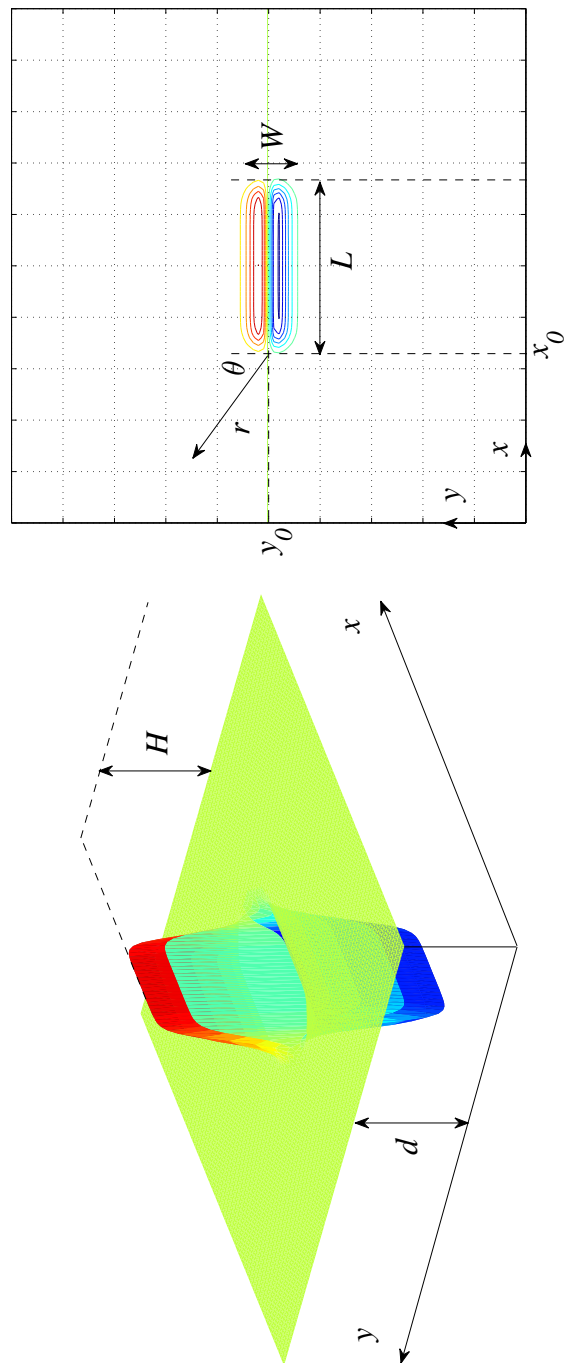


Figure 4.1: Definition sketch (not to scale): two-dimensional view (left inset) and top view (right inset).

## 4.2 Solution for Finite-crested Initial Waves

The finite-crested initial waveform considered here is defined as product of two independent functions,

$$\eta_0(x, y) = f(x) g(y), \quad (4.9)$$

as in Carrier and Yeh (2005). In Eq. (4.9), while  $g(y)$  represents the lateral cross-section of the source, such as a Gaussian, solitary, or an  $N$ -wave,  $f(x)$  describes the transverse extend of the initial wave profile (Figure 4.1). Representation of the initial wave as in Eq. (4.9) is advantageous because it allows evaluation of the Fourier transforms of  $f(x)$  and  $g(y)$  separately;

$$\begin{aligned} \hat{\eta}_0(k, l) &= \int_{-\infty}^{\infty} \int_{-\infty}^{\infty} f(x) g(y) e^{-i(kx+ly)} dx dy \\ &= \left[ \int_{-\infty}^{\infty} f(x) e^{-ikx} dx \right] \left[ \int_{-\infty}^{\infty} g(y) e^{-ily} dy \right] = \hat{f}(k) \hat{g}(l). \end{aligned} \quad (4.10)$$

Two typical examples for realistic cross-section profiles  $g(y)$  are the solitary wave and the generalized  $N$ -wave introduced in Chapter 2, the Fourier transforms of which are given in Synolakis (1987) and Tadepalli and Synolakis (1994), respectively. For the sake of clarity, the equations for the solitary wave and the generalized  $N$ -wave profiles, i.e., Eqs. (2.32) and (2.36), are recalled here. A solitary wave with initial amplitude  $H$  located at  $y = y_0$  is described by

$$g_s(y) = H \operatorname{sech}^2 \gamma_s (y - y_0), \quad (4.11)$$

with  $\gamma_s = \sqrt{3H/4}$ . Its Fourier transform is evaluated by Synolakis (1987) as

$$\hat{g}_s(l) = \frac{4\pi}{3} l e^{-il y_0} \operatorname{cosech} \alpha_s l, \quad (4.12)$$

with  $\alpha_s = \pi/(2\gamma_s)$ . A generalized  $N$ -wave profile is defined by Tadepalli and Synolakis (1994) as

$$g_n(y) = \varepsilon H (y - y_2) \operatorname{sech}^2 \gamma_n (y - y_1), \quad (4.13)$$

where  $\varepsilon$  is a scaling parameter which ensures that the initial wave amplitude is  $H$ . The points  $y_1$  and  $y_2$  are used to control the locations of the depression and elevation parts of the  $N$ -wave. The steepness parameter is defined as  $\gamma_n = \sqrt{3Hp_0/4}$ , where  $p_0$  is a parameter included to be able to change the steepness of the wave. The Fourier

transform of the generalized  $N$ -wave is evaluated by Tadepalli and Synolakis (1994) as

$$\hat{g}_n(l) = \frac{4\varepsilon H}{\pi} \alpha_n^2 e^{-i/y_1} [(y_1 - y_2)l + i(1 - \alpha_n l \coth \alpha_n l)] \operatorname{cosech} \alpha_n l, \quad (4.14)$$

with  $\alpha_n = \pi/(2\gamma_n)$ .

The finite-crest length profile will be given here by

$$f(x) = \frac{1}{2} [\tanh \gamma(x - x_0) - \tanh \gamma(x - (x_0 + L))], \quad (4.15)$$

unlike Carrier and Yeh (2005) who preferred the error function (erf). The source elongates from point  $x_0$  to  $x_0 + L$  along the  $x$ -axis; so  $L$  is the transverse length of the source, as shown in Figure 4.1. The parameter  $\gamma$  in Eq. (4.15) is dictated by the lateral cross-section  $g(y)$  of the initial wave, i.e., either as  $\gamma = \gamma_s$  (solitary wave) or as  $\gamma = \gamma_n$  ( $N$ -wave). The factor  $1/2$  is included so that the amplitude of  $f(x)$  is equal to the unity in the limit  $L \rightarrow +\infty$ ; in this case, the number of space variables reduces to one and Eq. (4.9) represents an infinitely long source.

Now, the Fourier transform of  $f(x)$  is required. Given

$$\int_{-\infty}^{\infty} \tanh \gamma x e^{-ikx} dx = -2i\alpha \operatorname{cosech} \alpha k, \quad (4.16)$$

$\alpha = \pi/(2\gamma)$ , derivation of which is presented in Appendix A, the Fourier transform of Eq. (4.15) takes the form

$$\hat{f}(k) = i\alpha (e^{-ikL} - 1) e^{-ikx_0} \operatorname{cosech} \alpha k. \quad (4.17)$$

Combining Eqs. (4.11) and (4.15), a two-dimensional finite-crested initial wave with solitary wave cross-section can be given as

$$\eta_s(x, y) = \frac{H}{2} \operatorname{sech}^2 \gamma_s(y - y_0) [\tanh \gamma_s(x - x_0) - \tanh \gamma_s(x - x_0 - L)], \quad (4.18)$$

with  $\gamma_s = \sqrt{3H/4}$ , and its Fourier transform is obtained by combining Eqs. (4.12) and (4.17) as

$$\hat{\eta}_s(k, l) = i \frac{4\pi}{3} \alpha_s l (e^{-ikL} - 1) e^{-i(kx_0 + ly_0)} \operatorname{cosech} \alpha_s k \operatorname{cosech} \alpha_s l, \quad (4.19)$$

with  $\alpha_s = \pi/(2\gamma_s)$ . Similarly, combination of Eqs. (4.13) and (4.15) gives a finite-crested source with  $N$ -wave cross-section,

$$\eta_n(x, y) = \frac{\varepsilon H}{2} (y - y_2) \operatorname{sech}^2 \gamma_n(y - y_1) [\tanh \gamma_n(x - x_0) - \tanh \gamma_n(x - x_0 - L)], \quad (4.20)$$



with  $\gamma_n = \sqrt{3Hp_0/4}$ , and its Fourier transform is obtained by combination of Eqs. (4.14) and (4.17) as

$$\begin{aligned}\hat{\eta}_n(k, l) = & i \frac{4 \varepsilon H}{\pi} \alpha_n^3 (e^{-ikL} - 1) e^{-i(kx_0 + ly_1)} [(y_1 - y_2) l + \\ & + i(1 - \alpha_n l \coth \alpha_n l)] \operatorname{cosech} \alpha_n k \operatorname{cosech} \alpha_n l,\end{aligned}\quad (4.21)$$

with  $\alpha_n = \pi/(2\gamma_n)$ .

### 4.3 Results and Discussions

In this section, first, the so-called axisymmetric water wave problem analyzed by Carrier and Yeh (2005) is revisited and some issues in their solution are addressed. Then, geophysical implications of the solution proposed in Section 4.1 is discussed in view of the 17 July 1998 Papua New Guinea and the 17 July 2006 Java Island tsunamis.

#### 4.3.1 Comparison with Carrier and Yeh (2005) solution<sup>2</sup>

In order to analyze the directivity of finite strip sources, Carrier and Yeh (2005) first developed analytical solution for axisymmetric waves (single Gaussian hump). They chose the characteristic length, depth, and time scales to be

$$l_0 = W, \quad d_0 = H, \quad t_0 = \frac{W}{\sqrt{gH}}, \quad (4.22)$$

in which  $W$  is the initial source breadth and  $H$  is the source amplitude, respectively (Figure 4.1). The nondimensional form of the two-dimensional LSW equation is again as in Eq. (4.1) with these scaling parameters. Introducing the change of variables  $r = \sqrt{x^2 + y^2}$ , the so-called axisymmetric governing equation is obtained from Eq. (4.1) as

$$\eta_{tt} - \frac{1}{r}(r\eta_r)_r = 0, \quad (4.23)$$

and the initial conditions (4.3) turn into

$$\eta(r, t = 0) = P(r), \quad (4.24a)$$

$$\eta_t(r, t = 0) = 0. \quad (4.24b)$$

---

<sup>2</sup> Eqs. (4.22) through (4.32) are taken from Carrier and Yeh (2005) and Figures (4.2) through (4.4) are reproductions of the corresponding figures of Carrier and Yeh (2005) using the methodology described in Section 4.1.

Using a Gaussian hump,

$$P(r) = 2 e^{-r^2}, \quad (4.25)$$

(Figure 4.2(a)), Carrier and Yeh (2005) first developed a Hankel integral transform solution to the governing equation (4.23);

$$\eta(r, t) = \int_0^\infty \rho J_0(\rho r) e^{-\rho^2/4} \cos \rho t d\rho. \quad (4.26)$$

However, they observed that the resultant integral of the axisymmetric solution becomes inconvenient to compute at large distances  $r$  or times  $t$ , although it is well behaved for small values of them. Hence, following Carrier et al. (2003), Carrier and Yeh (2005) expressed the solution in terms of the complete elliptic integral, i.e.,

$$\eta(r, t) = \frac{\partial}{\partial t} \int_0^\infty P(\rho) G(\rho, r, t) d\rho, \quad (4.27)$$

where

$$G(\rho, r, t) = \begin{cases} \frac{2\rho}{\pi \sqrt{t^2 - (r-\rho)^2}} K\left(\frac{4r\rho}{t^2 - (r-\rho)^2}\right) & \text{for } t > r + \rho, \\ \frac{1}{\pi} \sqrt{\frac{\rho}{r}} K\left(\frac{t^2 - (r-\rho)^2}{4r\rho}\right) & \text{for } |r - \rho| < t < r + \rho, \\ 0 & \text{for } t < |r - \rho|. \end{cases} \quad (4.28)$$

Here,  $K$  is the complete elliptic integral of the first kind defined by

$$K(\lambda) = \int_0^{\pi/2} \frac{dv}{\sqrt{1 - \lambda \sin^2 v}}. \quad (4.29)$$

Carrier and Yeh (2005) showed that the solution (4.27) of Eq. (4.23) exhibits a self-similar behavior, i.e.,  $t \sim r$  (Figure 4.2(b)). They used the self-similarity property to extend their axisymmetric solution to the elongated source defined as

$$\eta_0(x, y) = [\operatorname{erf}(x_0 + L - x) - \operatorname{erf}(x_0 - x)] e^{-y^2}, \quad (4.30)$$

replacing the complete elliptic integral with the modified Bessel functions through trial-and-error, i.e.,

$$\eta(x, y, t) \cong \frac{1}{\sqrt{\pi}} \int_{x_0}^{x_0+L} (50t)^{1/2} \varphi\left(\frac{y^2 - t^2}{4t} + \frac{x^2 - x'^2}{4t}\right) dx', \quad (4.31)$$

where

$$\varphi(s) \approx -0.0238 \frac{d}{ds} \begin{cases} (2s^2)^{1/4} K_{1/4}(2s^2) e^{-2s^2} & \text{for } s > 0, \\ (2s^2)^{1/4} [K_{1/4}(2s^2) + \pi \sqrt{2} I_{1/4}(2s^2)] e^{-2s^2} & \text{for } s < 0. \end{cases} \quad (4.32)$$

Here,  $I_{1/4}$  and  $K_{1/4}$  are the modified Bessel functions of first and second kind of order  $1/4$ , respectively. The drawbacks of the Carrier and Yeh (2005) solution arise at this point. First, their solution for elongated source is applicable only to the specific initial condition given in Eq. (4.30) since it involves trial-and-error procedure. Second, due to the approximation introduced in Eq. (4.32), their solution is approximate.

In contrast to Carrier and Yeh (2005), the exact solution of the axisymmetric problem is possible with the method presented in Section 4.1. Given the Gaussian hump

$$P(r) = 2 e^{-r^2} = 2 e^{-(x^2+y^2)} = \eta_0(x, y), \quad (4.33)$$

its Fourier transform is computed as

$$\hat{\eta}_0(k, l) = 2 \pi e^{-(k^2+l^2)/4}, \quad (4.34)$$

and the axisymmetric wave solution becomes

$$\eta(x, y, t) = \frac{1}{2\pi} \int_{-\infty}^{\infty} \int_{-\infty}^{\infty} e^{-(k^2+l^2)/4} e^{i(kx+ly)} \cos t \sqrt{k^2 + l^2} dk dl, \quad (4.35)$$

through Eq. (4.8). The temporal evolution given in Figure 4.2(b) is obtained from Eq. (4.35). Results not only show exact comparison with Carrier and Yeh (2005), but also no difficulty is experienced in direct numerical integration of Eq. (4.35). In addition, Figure 4.2(b) exposes the self-similarity ( $t \sim r$ ) of the axisymmetric wave solution, a property used by Carrier and Yeh (2005) to approximate the solution for the elongated source (4.30), as described above.

The extension of the solution to a strip source is also straightforward. The Fourier transform of the elongated source, Eq. (4.30), defined by Carrier and Yeh (2005) is

$$\hat{\eta}_0(k, l) = i \frac{2\sqrt{\pi}}{k} e^{-ikx_0} (e^{-ikL} - 1) e^{-(k^2+l^2)/4}, \quad (4.36)$$

and the associated solution through Eq. (4.8) is given by

$$\eta(x, y, t) = \frac{i}{2\pi^{3/2}} \int_{-\infty}^{\infty} \int_{-\infty}^{\infty} \frac{(e^{-ikL} - 1)}{k} e^{-(k^2+l^2)/4} e^{i[k(x-x_0)+ly]} \cos t \sqrt{k^2 + l^2} dk dl. \quad (4.37)$$

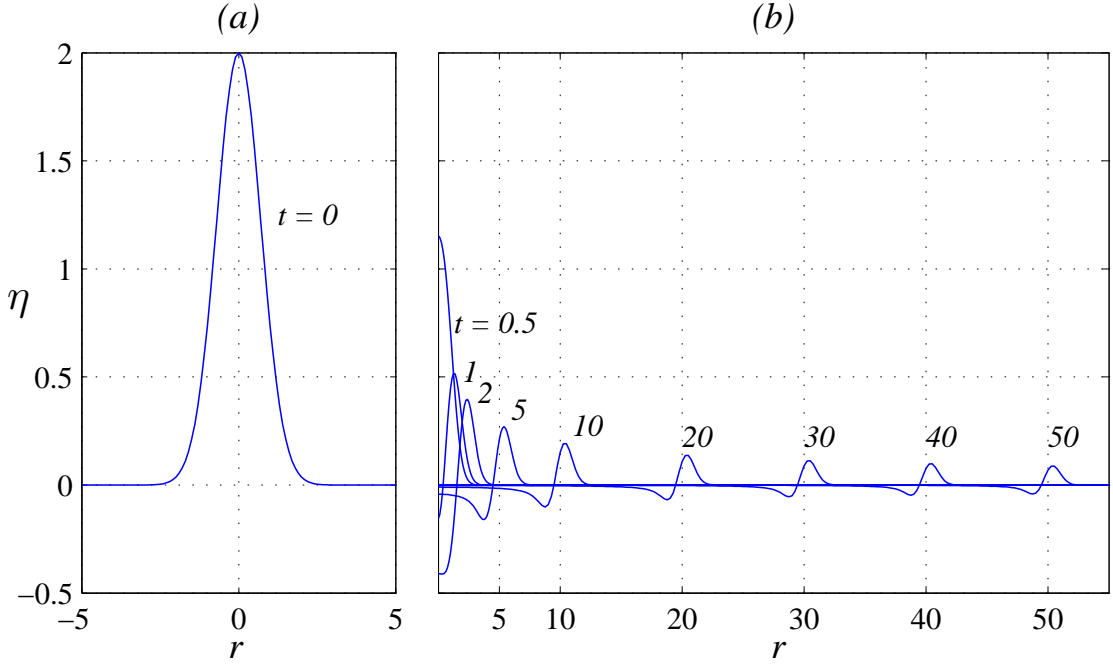


Figure 4.2: (a) The Gaussian hump defined by Eq. (4.25). (b) Evolution of the Gaussian hump at times  $t = 0.5, 1, 2, 5, 10, 20, 30, 40$ , and  $50$ . The self-similarity ( $t \sim r$ ) of the solution (4.35) can be observed for  $t > 5$ .

Comparison of the solutions (4.31) and (4.37) reveals the simplicity of the solution presented in Section 4.1. In Figure 4.3, an elongated source with fixed length  $L = 20$  is considered as in Carrier and Yeh (2005). Time series of water surface elevation is evaluated along different angular directions ( $\theta = 0^\circ, 45^\circ, 90^\circ$ ) by direct numerical integration of Eq. (4.37).

The effect of the source length  $L$  on wave height distribution is demonstrated in Figure 4.4. Time series along directions normal ( $\theta = 0^\circ$ ) and parallel ( $\theta = 90^\circ$ ) to the transverse  $x$ -axis are computed for varying  $L$ , as in Carrier and Yeh (2005).

#### 4.3.2 Propagation of an $N$ -wave over a constant depth

Now propagation of an  $N$ -wave defined by

$$\eta_0(x, y) = [\text{erf}(x_0 + L - x) - \text{erf}(x_0 - x)] (e^{-(y-y_1)^2} - e^{-(y-y_2)^2}), \quad (4.38)$$

over a constant depth is considered. This wave is constructed by adding a depression (negative) wave in front the elevation (positive) one. As it starts propagating, this

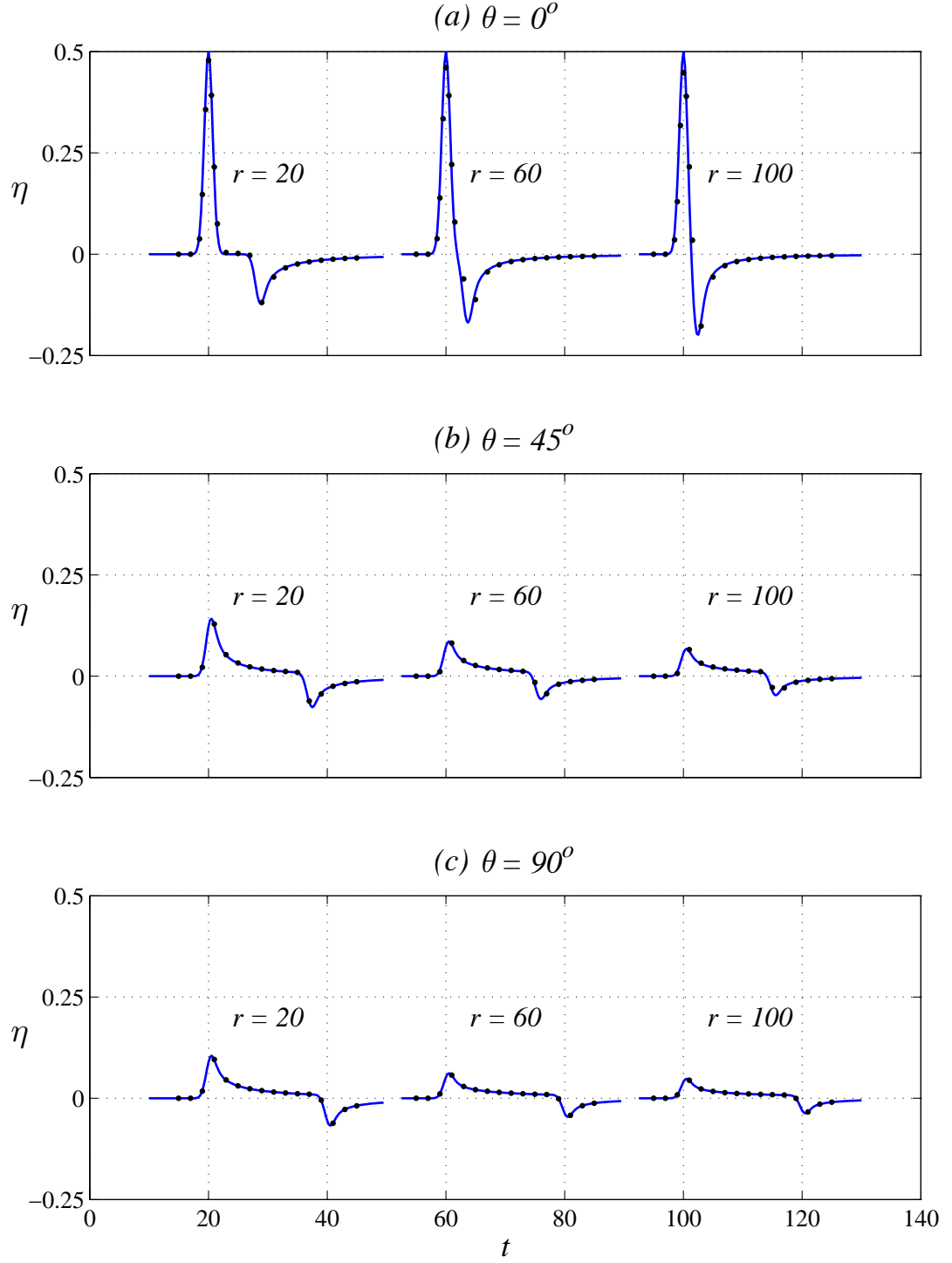


Figure 4.3: Temporal variations of the water surface elevation of the elongated Gaussian source, Eq. (4.30), with crest length  $L = 20$  are evaluated through Eq. (4.37) at distances  $r = 20, 60$ , and  $100$  along the directions (a)  $\theta = 0^\circ$ , (b)  $\theta = 45^\circ$ , and (c)  $\theta = 90^\circ$ . Solid lines show the present analytical solution while dots show Carrier and Yeh (2005)'s solution. The initial source Eq. (4.30) is located at  $(x_0, y_0) = (-L/2, 0)$  to have one-to-one comparison with the Figure 7 of Carrier and Yeh (2005).

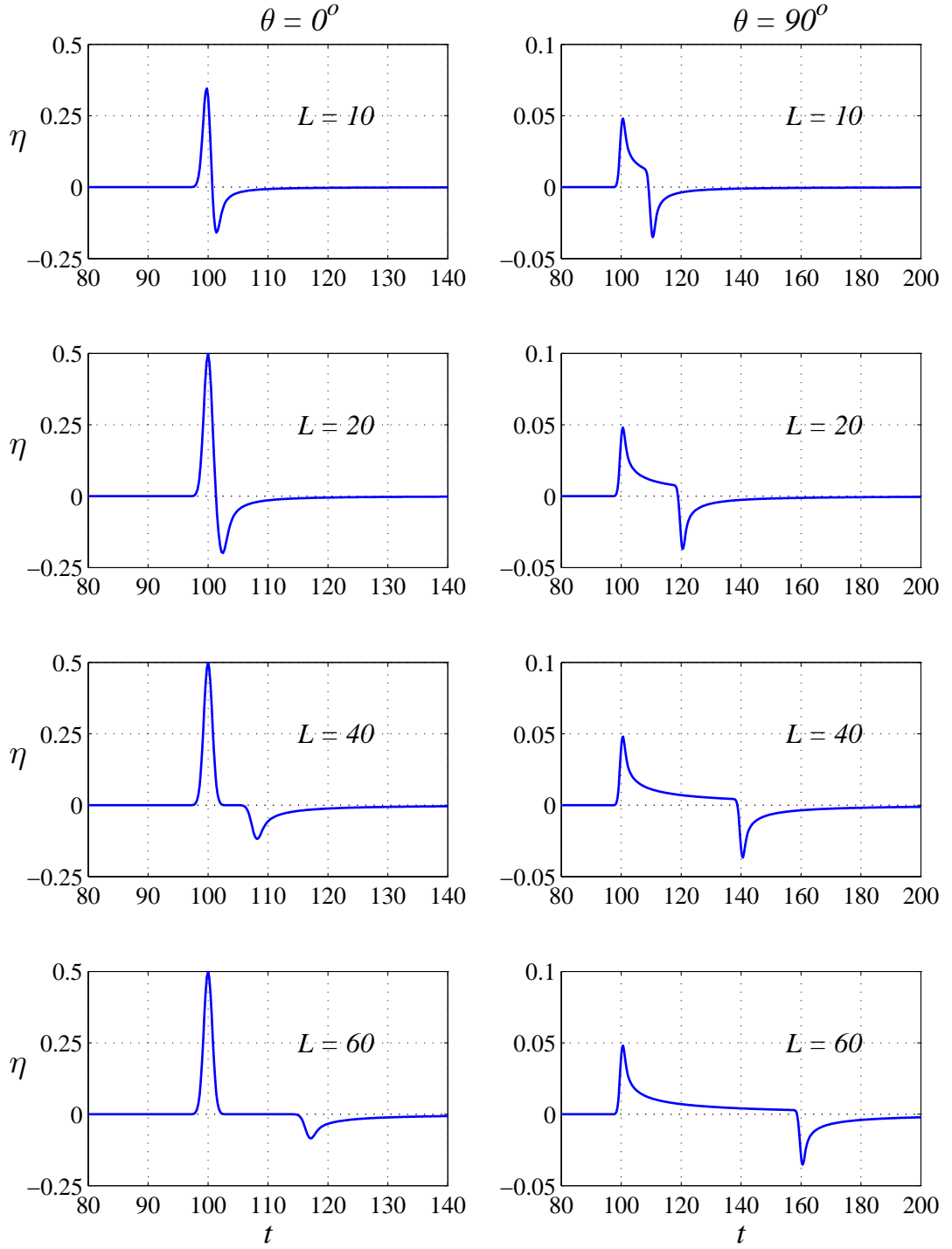


Figure 4.4: Time histories of the water surface elevation are evaluated through Eq. (4.37) for different source lengths ( $L = 10, 20, 40$ , and  $60$ ) along the directions normal ( $\theta = 0^\circ$ ) and parallel ( $\theta = 90^\circ$ ) to the major axis ( $x$ -axis) of the source. The source is initially located at  $(x_0, y_0) = (0, 0)$  and the water surface variations are recorded at the distance  $r = 100$ . This figure is a reproduction of the Figure 8 of Carrier and Yeh (2005).

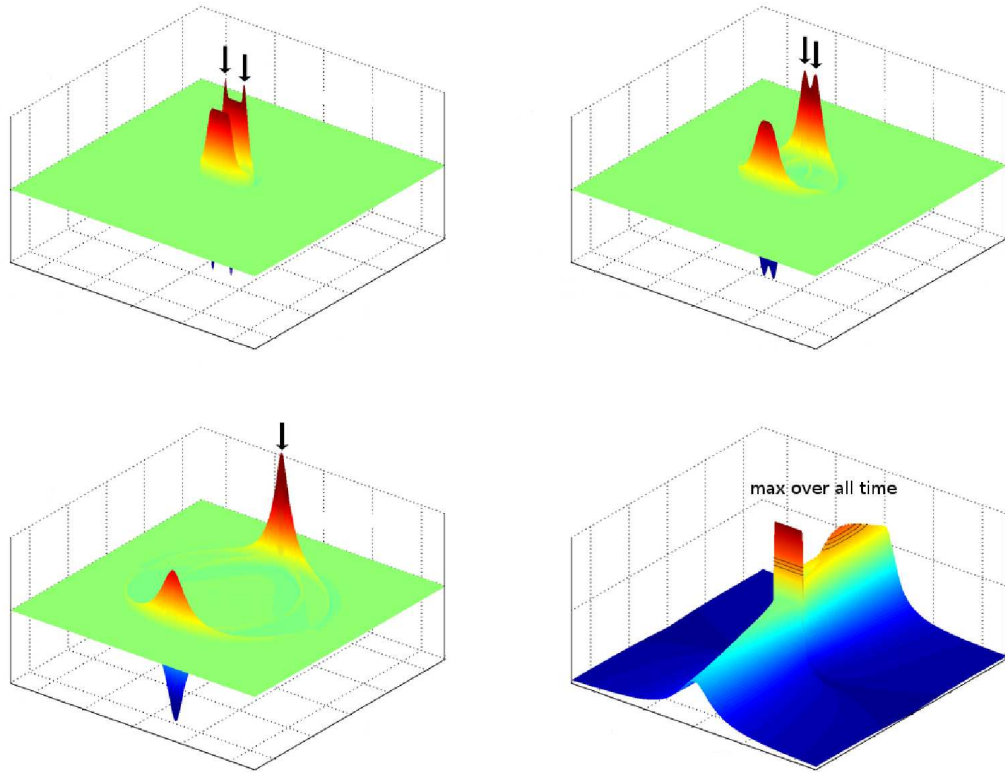


Figure 4.5: Propagation of a plus-minus source over a constant ocean basin showing focusing. (Lower right inset) Overall maximum amplitude for each grid point having extreme maximum wave height (focusing point) on the leading depression side of the propagation (Moore, personal communication).

plus-minus initial wave splits into leading depression (LDN) and leading elevation (LEN)  $N$ -waves propagating in opposite directions.

Interesting phenomena can be observed on both sides. Elevation part of the LDN and depression part of the LEN overshoot on sides (arrows in Figure 4.5). Overshooting sides propagate towards the bisector line as the wave front propagates. Side waves and the wave front then merge together on the bisector line along  $x$ -axis and create a region in which abnormal wave height could be observed such as the region shown in the lower right inset of Figure 4.5. In this region, there is a point along the bisector line where wave heights reaches to a maximum. This point is called focusing point. Focusing might explain some of the extreme runup observations in the field.

Now, two examples, the 17 July 1998 Papua New Guinea and the 17 July 2006 Java Island, Indonesia tsunamis will be discussed in view of focusing phenomenon.

### 4.3.3 The 17 July 1998 Papua New Guinea Tsunami

As mentioned in Chapter 1, the tsunami community has long discussed unexpected high localized tsunami runup values after the 17 July 1998 Papua New Guinea (PNG) tsunami. The magnitude  $M_w$  7.0 earthquake with the epicenter approximately 25 km off the north coast of Aitape struck PNG at 08:49 UTC (18:19 local time). The earthquake triggered a larger-than-expected tsunami which caused more than 2,200 casualties. Leaving the detailed discussion of the event to Synolakis et al. (2002), another possible explanation for high tsunami runup is discussed here, i.e., the focusing effect.

The initial landslide source suggested by Synolakis et al. (2002) is a generalized  $N$ -wave with approximately  $-18\text{ m}$  leading-depression followed by a  $+16\text{ m}$  elevation, as in Figure 4.6(a). Evolution of this initial wave profile over a constant depth through Eq. (4.8) is given in Figures 4.6(b–d). In Figure 4.7, one- and two-dimensional propagation results are compared. In both cases, a leading-depression  $N$ -wave (LDN) propagates in one direction while a leading-elevation  $N$ -wave (LEN) propagates in the other direction. This is consistent to the field observations such as the one after the 26 December 2004 tsunami, i.e., while in Male, Maldives, the tsunami manifested itself as an LEN, as elsewhere to the west of the Sumatran subduction zone. In Phuket, Thailand, it manifested itself as an LDN, as elsewhere to the east of the subduction zone (Satake, 2007). This is also consistent to the inferences of Tadepalli and Synolakis (1994, 1996). However, while one-dimensional propagation results show that the initial wave splits into two waves which propagate with the same elevation and depression heights in both directions, two-dimensional propagation results into a propagation with different elevation and depression heights.

Figure 4.8 presents the observed maximum wave height for entire time along the bisector line at each spatial location -maximum wave height envelope- including time snapshots along the bisector line for the times  $t = 0, 5, 25$ , and 40. As seen from the maximum wave height envelope, there is an increase in the maximum wave height along the bisector line before reaching its final propagation wave height, i.e., there is focusing on the leading-depression side.

The effects of crest length  $L$  and steepness  $p_0$  over the location of the focusing point



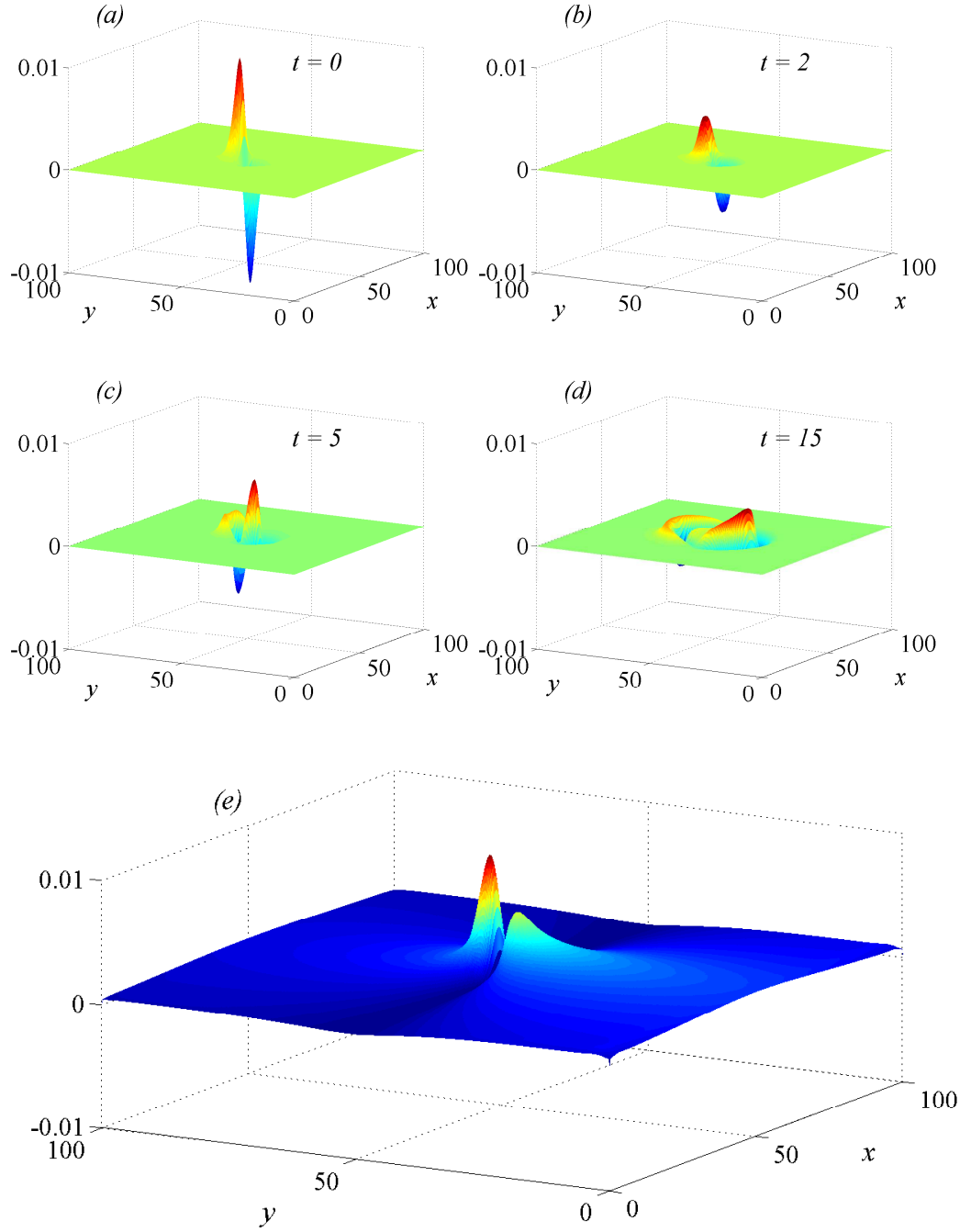


Figure 4.6: Evolution of the PNG wave over a constant depth at (a)  $t = 0$ , (b)  $t = 2$ , (c)  $t = 5$ , and (d)  $t = 15$ . PNG initial wave is defined as  $\eta_n(x, y) = f(x)g_n(y) = \frac{1}{2}\varepsilon H[\tanh \gamma_n(x - x_0) - \tanh \gamma_n(x - (x_0 + L))](y - y_2) \operatorname{sech}^2 \gamma_n(y - y_1)$  with parameters  $H = 0.01$ ,  $p_0 = 15$ ,  $L = 1$ ,  $\gamma_n = 0.34$ ,  $y_1 = 50$ ,  $y_2 = y_1 + 0.2 = 50.2$ ,  $x_0 = 49.5$ , and  $\varepsilon = 4.93$ . (e) Overall maximum wave height at each grid point computed through the numerical model MOST (from Kânoğlu et al., in preparation).

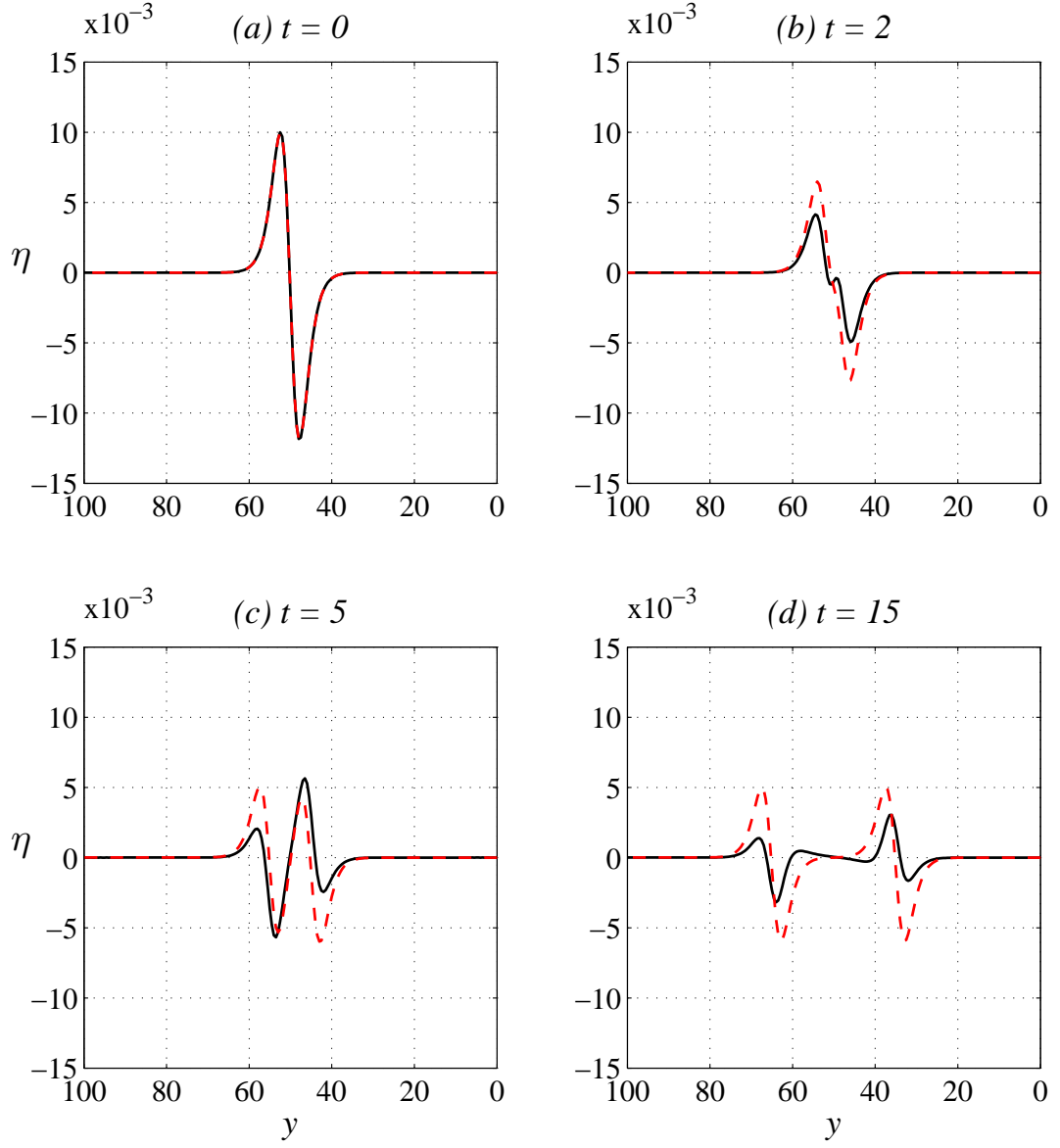


Figure 4.7: Two-dimensional  $N$ -wave surface profile  $\eta_n(x, y) = f(x)g_n(y)$  (solid line) is compared with one-dimensional  $N$ -wave defined by  $\eta_n(y) = \epsilon H(y - y_2) \text{sech}^2 \gamma_n(y - y_1)$  (dashed line) at (a)  $t = 0$ , (b)  $t = 2$ , (c)  $t = 5$ , and (d)  $t = 15$ . Note that the slice of the two-dimensional surface is plotted along the bisector line in  $x$ -direction. The scaling parameter  $\epsilon$  for one dimensional  $N$ -wave is  $\epsilon = 0.82$ . Refer to the caption of Figure 4.6 for the other parameters.

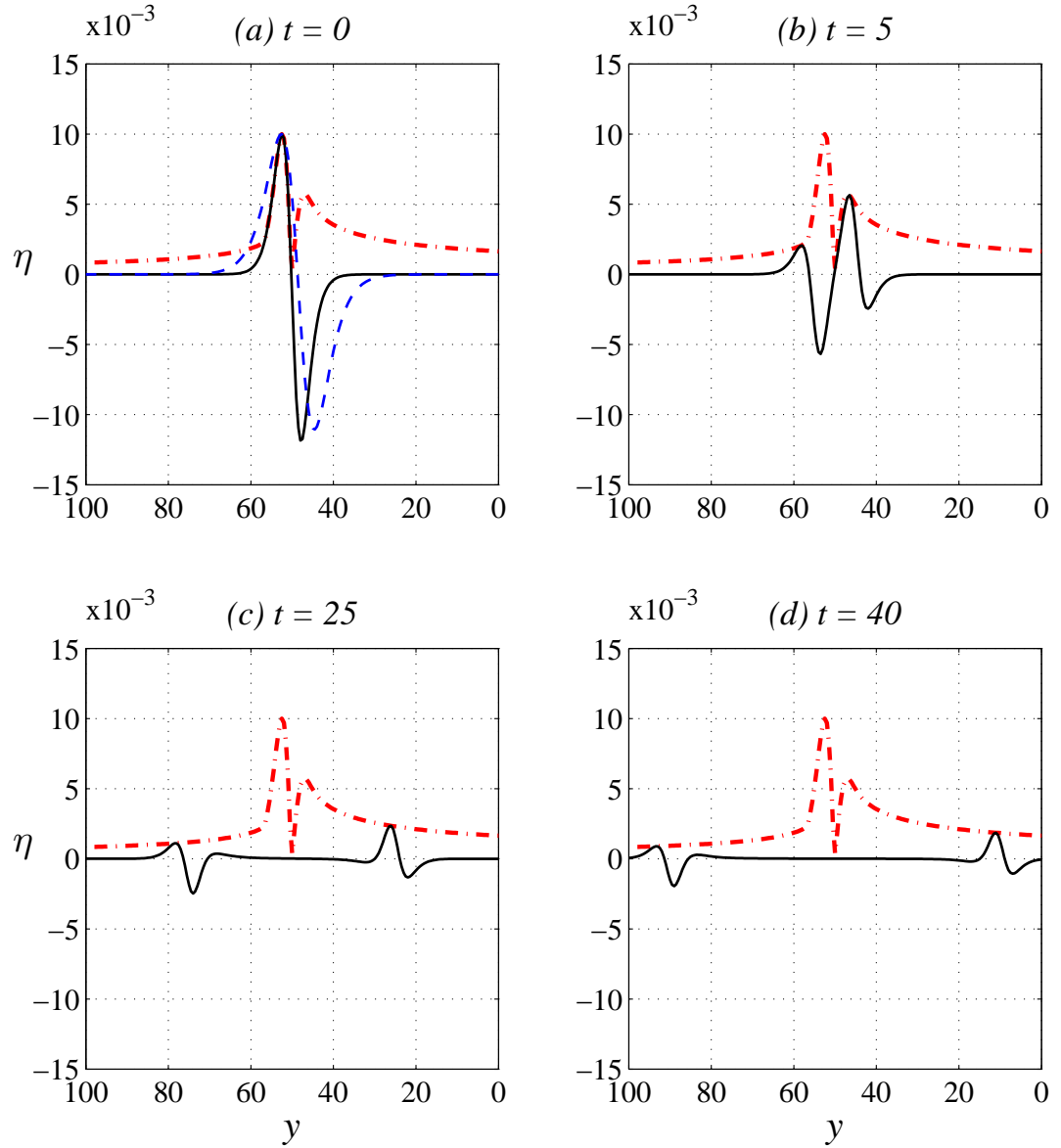


Figure 4.8: Spatial variations of water surface elevations (solid line) are plotted at (a)  $t = 0$ , (b)  $t = 5$ , (c)  $t = 25$ , and (d)  $t = 40$  including maximum wave height envelope (dash-dotted line). The dashed line in inset (a) is the initial wave profile with steepness  $p_0 = 5$ . Refer to the caption of Figure 4.6 for the other parameters.

are also investigated. As the crest length  $L$  increases, the focusing point moves further away with increasing maximum wave height, as expected (Figure 4.9(a)). Also, final wave heights in the leading-elevation and -depression sides are different, the latter being higher, which is attributed to the nature of the two-dimensional propagation. When the steepness parameter  $p_0$  decreases, i.e., the initial wave becomes less steep, the focusing point moves forward and maximum wave height decreases slightly (Figure 4.9(b)).

Further analysis of the PNG event suggests that shoreline would face almost a factor of 1.5 offshore wave height compared to the case if the shoreline was  $r = 50 \text{ km}$  away, as indicated in Figure 4.10(a). It should be noted that the runup law (Synolakis, 1987),  $R \sim H^{5/4}$ , results in a runup increase by factor of 1.7.

During the PNG event, Sissano Lagoon was where maximum number of casualties were reported. The lagoon is approximately  $r = 25 \text{ km}$  away from the source location, along  $\beta = 45^\circ$  direction, as indicated in Figure 4.10(b). The focusing point locations for two different steepness parameters,  $p_0 = 15$  and  $p_0 = 5$  are shown in Figure 4.10(b) by dots and triangles, respectively. The contours of the initial source of the event defined by Synolakis et al. (2002) is also reconstructed in that figure. Figure 4.10(b) indicates that, if the source proposed by Synolakis et al. (2002) had different steepness, i.e.,  $p_0 = 5$  instead of 15, the focusing would occur approximately  $8.7 \text{ km}$  closer to the lagoon.

#### 4.3.4 The 17 July 2006 Java Island Tsunami

The magnitude  $M_w$  7.7 earthquake with epicenter approximately  $225 \text{ km}$  northeast of Christmas Island ( $355 \text{ km}$  south of Jakarta) hit Java, Indonesia on 17 July 2006 at 08:19 UTC (15:19 local time) and generated a tsunami. Fritz et al. (2007) surveyed the area covering  $600 \text{ km}$  of coastline. The tsunami affected over  $300 \text{ km}$  of coastline and caused more than 600 casualties. Although overall runup values were changing from  $5 \text{ m}$  to  $7 \text{ m}$  at surrounding areas, a locally focused runup peak exceeding  $20 \text{ m}$  was measured at Permisan. Fritz et al. (2007) infer, following the invariants presented by Okal and Synolakis (2004), that the focused runup height suggests a possible local submarine slump or mass movement. Here, another possible explanation for a such

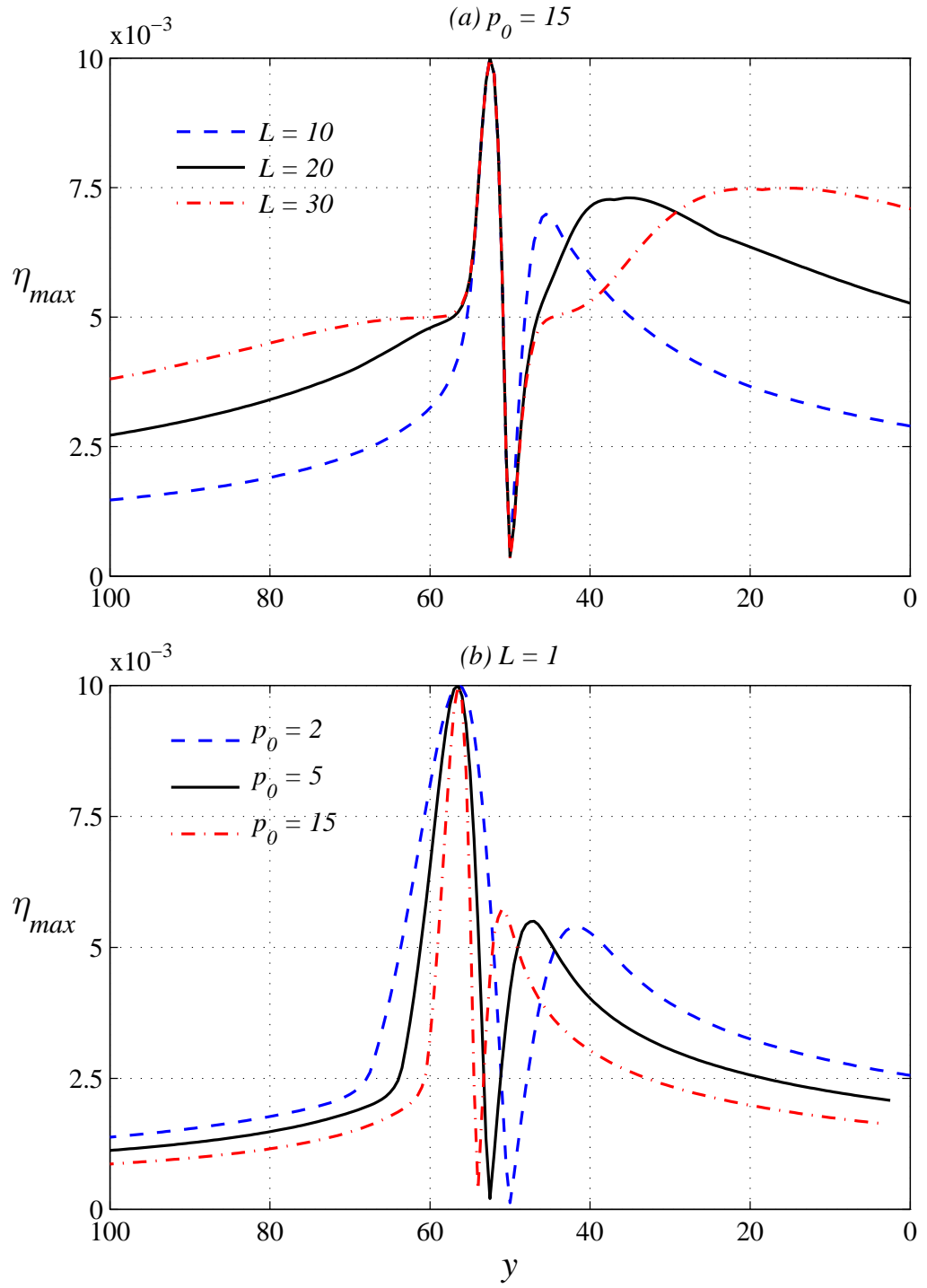


Figure 4.9: The effect of (a) the source length ( $L$ ), (b) the wave steepness ( $p_0$ ) on the location of the focusing point for the PNG initial wave. The maximum wave heights are recorded along the bisector line, i.e., line perpendicular to the source strip. The steepness parameter is  $p_0 = 15$  for inset (a) and the source length is  $L = 1$  for inset (b). Parameters other than  $p_0$  and  $L$  are the same as in the caption of Figure 4.6.

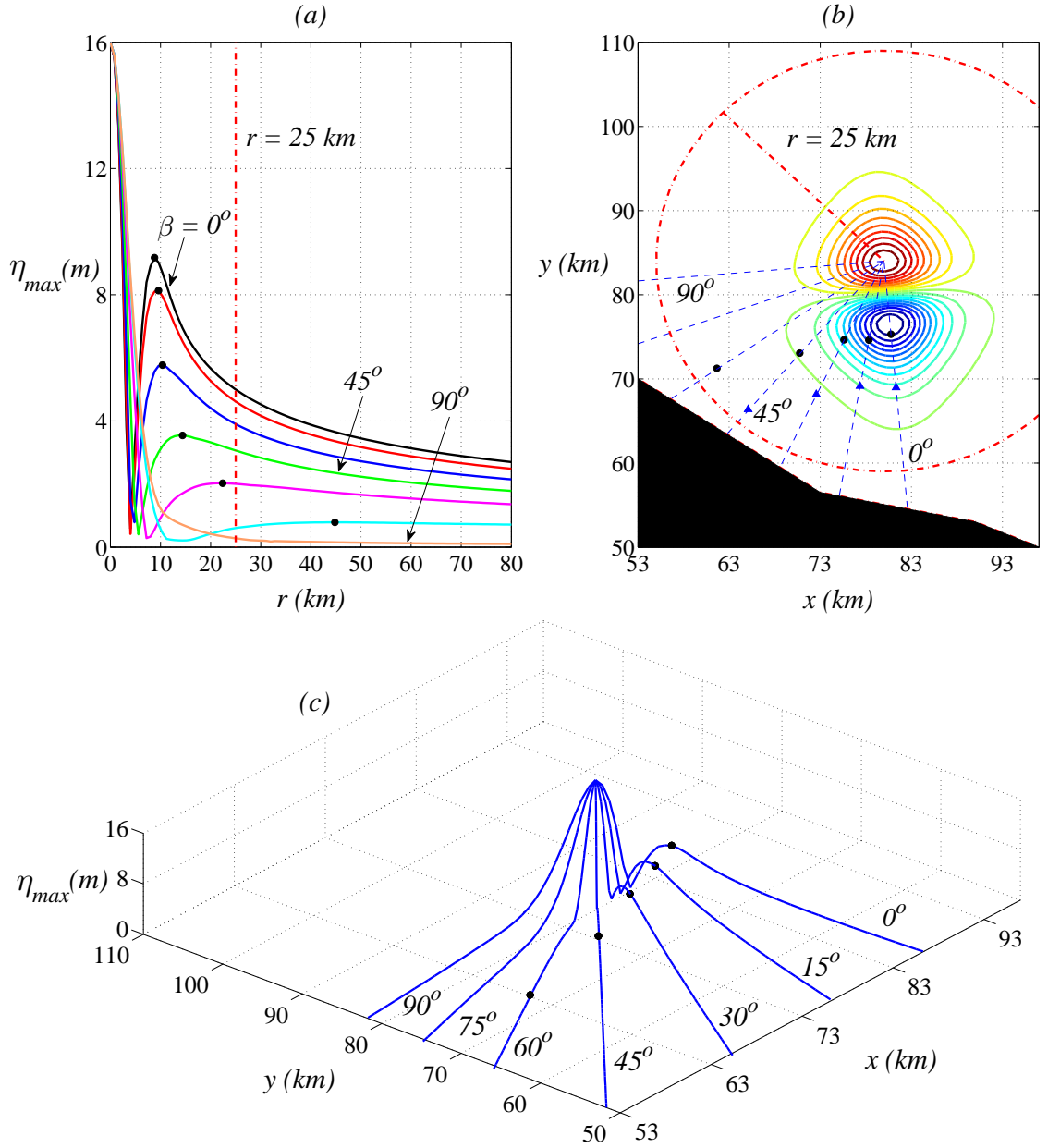


Figure 4.10: (a) Maximum wave amplitude variations along different directions ( $\beta$ -lines) are plotted over a distance  $r$  from the nondimensional point  $(x, y) = (50, 52.5)$ , which is the approximate location of the PNG initial source proposed by Synolakis et al. (2002). The nondimensional wave height  $H = 0.01$  corresponds to a dimensional  $16 m$  for the reference depth  $d = 1600 m$ . (b) The maximum wave amplitudes along each  $\beta$ -line (black dots) are plotted on the contours of the PNG initial source. The  $r = 25 km$  radius circle shows the approximate location of the Sissano area over the  $\beta = 45^\circ$  line. Triangles show the maximum wave amplitude locations for the initial wave with  $p_0 = 5$ , which is plotted in Figure 4.8(a). (c) Three-dimensional view of the maximum wave amplitude variation of the PNG source along different directions  $\beta$ . Refer to the caption of Figure 4.6 for the parameters.

pronounced runup is proposed.

Marchuk and Titov (1989) explained an existence of tsunami focusing for sources having elevation and depression. As explained in Section 4.3.2, focusing point is a point where a wave from the center of the elevation side and from sides of the depression arrives simultaneously. For the 17 July 2006 Java event, Permisan can be considered as the location of focusing, i.e., focal point. In Figure 4.11, reverse tsunami travel time (RTTT) contours representing time it will take for a source over a contour to reach the shoreline point are presented (Kânoğlu et al., in preparation). Unit tsunami source functions from the propagation database of the NOAA (National Oceanic and Atmospheric Administration) Center for Tsunami Research (NCTR) of the United States are plotted over the RTTT contours. The United States Geological Survey (USGS) finite source solution for the event is also included for reference.

Detailed explanation of the tsunami propagation database of the NCTR and application of it can be found in Wei et al. (2008). Briefly, the NCTR is developing real time forecasting system for the use in the Pacific and the West Coast and Alaska Tsunami Warning Centers. Ocean base propagation is evaluated for tsunami source functions, also called unit sources, using the Method of Splitting Tsunamis (MOST) numerical model, which is extensively validated and verified (Synolakis et al., 2008). Tsunami source function represents propagation from a 100 km by 50 km block source with 1 m slip (displacement) which corresponds a 7.5 magnitude earthquake. Linearity of the propagation in deep ocean allows linear combination of unit sources to set up larger magnitude scenario events.

Here, among scenario events (combination of the sources), a scenario is identified for which focusing occurs close to Permisan. Combination of the three unit sources shown in Figure 4.11 fits the RTTT contours well, i.e., the 45-minute contour passes approximately through the maximum elevation point and sides of the depression and generates focusing around Permisan. The propagation of the proposed source of the Java event over constant depth through the MOST model is presented in Figure 4.12. In Figure 4.13, the maximum wave height contours calculated from the solution over constant depth using the MOST model are included together with the propagation of the proposed source over the real bathymetry. The maximum amplitude contours are

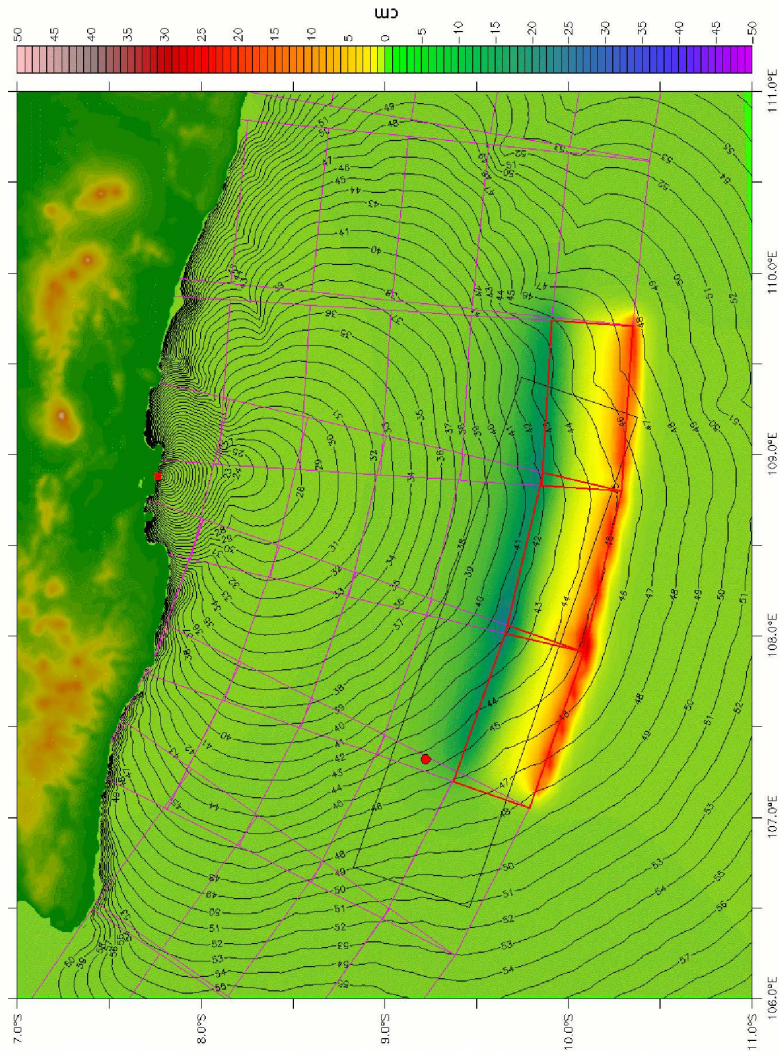


Figure 4.11: Reverse tsunami travel time (RTTT) contours are shown for Permisan (red filled square; Spillane, personal communication). Magenta grid represents the NCTR's  $100\text{ km} \times 50\text{ km}$  unit sources. Considering tsunami travel time and focusing, the source configuration including three unit sources (red rectangles) are proposed as a possible source mechanism of the 17 July 2006 Java tsunami (Moore, personal communication). Black rectangle is the USGS source for the event. Red dot shows the earthquake epicenter location.



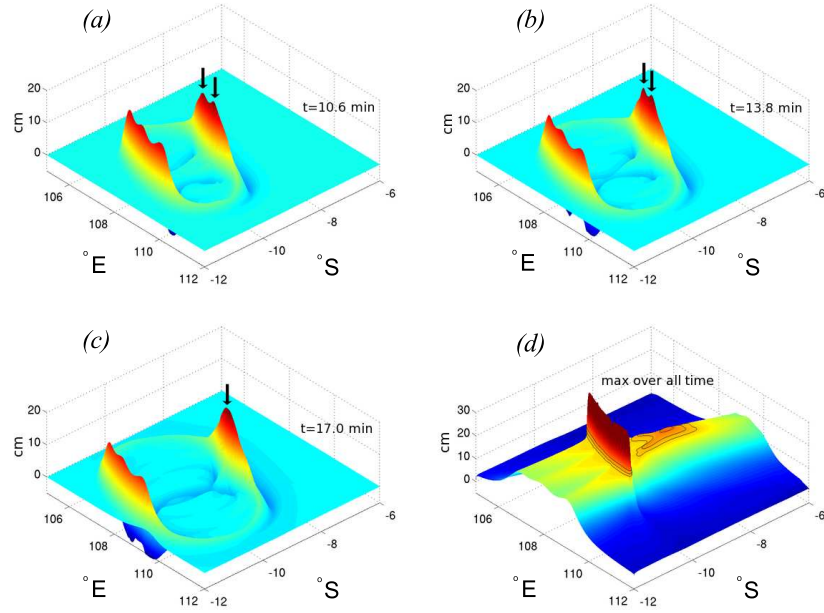


Figure 4.12: Propagation of the proposed source of the Java event (Figure 4.11) over a constant depth using the numerical model MOST at times (a)  $t = 10.6$  minute, (b)  $t = 13.8$  minute, and (c)  $t = 17.0$  minute. (d) Overall maximum amplitude for each grid point (from Kânoğlu et al., in preparation).

included in order to indicate the potential focusing locations for the area.

It should be noted here that limited bathymetric and topographic data exist for the region. Therefore, it was not possible to make satisfactory computations to evaluate the runup distribution along the shoreline. Present model results suggested approximately  $5\text{ m}$  runup at Permisan. Arrival time is approximately 45 minutes after the event which is consistent with the eyewitnesses accounts (Fritz et al., 2007). The computations performed here clearly show that Permisan is close to the focusing point and hence it is possible that the high runup resulted due to focusing. Therefore, it could be suggested that the methodology presented above can be used to identify tsunami source mechanisms considering focusing location and tsunami travel time.

#### 4.4 Conclusions

The two-dimensional long wave propagation problem over a constant-depth basin is solved analytically using the LSW equation. The double Fourier transform is applied

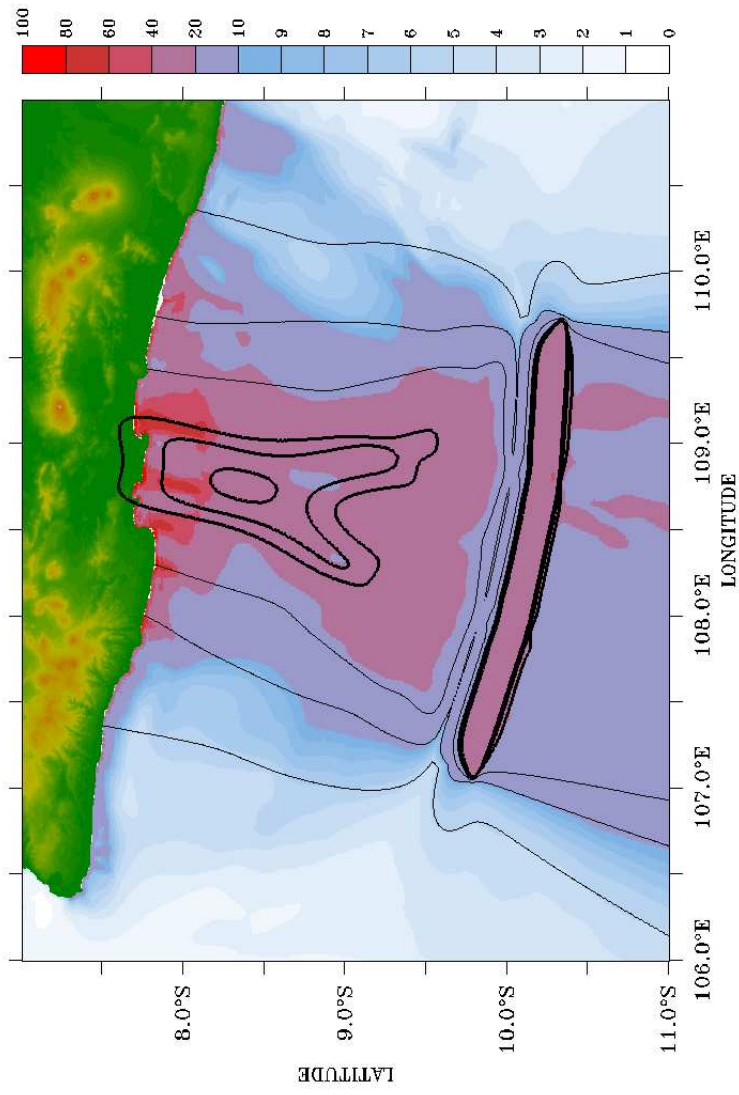


Figure 4.13: Propagation of the proposed source over the real bathymetry off Java, Indonesia. Maximum wave amplitude contours for the propagation over the constant depth are also incorporated to point out potentially dangerous locations because of focusing (from Kânoğlu et al., in preparation).

to the governing LSW equation. The transformed equation is solved as an IVP for realistic initial waveforms. The subsequent wave motion is analyzed and results of the two-dimensional problem are compared with the one-dimensional case. Existence of focusing point for a combined elevation and depression source is shown analytically and extreme runup observations reported from the field surveys of the 17 July 1998 Papua New Guinea and the 17 July 2006 Java tsunamis are explained in view of focusing. The analytical solution developed here could be used as benchmark solution, in addition to the other analytical solutions presented in Synolakis et al. (2008). Also, it could be used to identify or to refine possible source mechanisms as it is done for the PNG and Java events.

## CHAPTER 5

### CONCLUSIONS

In this study, several analytical solutions for the linear and nonlinear shallow-water wave equations are developed over one- and two-dimensional bathymetry.

First, brief introduction of analytical solutions for the shallow-water wave equations is presented in Chapter 1.

In Chapter 2, an analytical solution for the one-dimensional nonlinear shallow-water wave (NSW) equations is developed for computation of shoreline motion and runup of long waves propagating on a linearly sloping beach. The solution is given in terms of a Fourier-Bessel series after transforming the equations with the so-called hodograph transformation suggested by Carrier and Greenspan (1958). First, propagation of Gaussian waves are analyzed under general initial conditions, i.e., a prescribed initial wave profile and nonzero initial velocity distribution, and compared with the existing integral transform solution of Carrier et al. (2003). The shoreline motion characteristics of three different initial velocity assumptions, namely the exact nonlinear (Kânoğlu and Synolakis, 2006), the linearized (Carrier et al., 2003), and the asymptotic (Prichard and Dickinson, 2007) initial velocity distributions are also compared. Then, the solitary wave, the isosceles and the generalized  $N$ -wave initial profiles are imposed and the results are analyzed for the cases with and without initial velocity. Finally, surface profiles produced by near-shore earthquakes are obtained with the proposed method and the results are compared with the solution of Tinti and Tonini (2005). The solution method presented here appears advantageous over the existing methods mentioned above, as it does not involve evaluation of singular elliptic integrals and also initial profiles with nonzero velocity distribution can be incorporated

easily.

In Chapter 3, the solution methodology developed in Chapter 2 is used in order to obtain the subsequent evolution of wave oscillations and shoreline motion generated in a long narrow basin after relaxation of wind stress. The problem is analyzed in two phases: the steady-state phase in which the sea surface state under wind stress is calculated explicitly using an appropriate balance equation, and the (unsteady) relaxation phase in which the resultant wave oscillations in the absence of wind are calculated solving the NSW equations with the hodograph transformation. Successful comparison with existing numerical solution of Gelb et al. (1997) is obtained.

In the framework of the NSW theory in one space dimension, an approximate analytical solution for propagation of landslide-generated waves is also derived (Appendix B). Evolution of the waves resulting from a time-dependent Gaussian bottom forcing is obtained and compared with the linear analytical solution given by Liu et al. (2003) for certain geometric parameters. The drawback of the solution, preventing further nonlinear analysis of the problem, is described.

In Chapter 4, an initial value problem solution for the linear shallow-water wave equation over a two-dimensional flat ocean bottom is presented by using the Fourier integral transform technique. The key advance is the incorporation of initial waves having finite transverse length. Analytical verification of a phenomenon called source focusing is provided. The role of focusing in unexpectedly high tsunami runup observations of the 17 July 1998 Papua New Guinea and the 17 July 2006 Java Island, Indonesia tsunamis are investigated.

The analytical solutions developed here could be used as benchmark solutions for validation of numerical models in addition to the analytical solutions presented in Synolakis et al. (2008).

## REFERENCES

- Antuono, M. and Brocchini, M. (2007). The boundary value problem for the nonlinear shallow water equations. *Studies in Applied Mathematics*, 119:73–93.
- Antuono, M. and Brocchini, M. (2010). Solving the nonlinear shallow-water equations in physical space. *Journal of Fluid Mechanics*, 643:207–232.
- Aydın, B. and Kânoğlu, U. (2007). Wind set-down relaxation. *CMES: Computer Modeling in Engineering and Sciences*, 21(2):149–155.
- Ben-Menahem, A. (1961). Radiation of seismic surface waves from finite moving sources. *Bulletin of Seismological Society of America*, 51:401–435.
- Ben-Menahem, A. and Rosenman, M. (1972). Amplitude patterns of tsunami waves from submarine earthquakes. *Journal of Geophysical Research*, 77:3097–3128.
- Bernard, E. N. and Robinson, A. R. (2009). Chapter 1, Introduction: Emergent Findings and New Directions in Tsunami Science. In Bernard, E. N. and Robinson, A. R., editors, *The Sea, Volume 15: Tsunamis*, pages 1–22. Harvard University Press.
- Berry, M. V. (2007). Focused tsunami waves. *Proceedings of the Royal Society of London A*, 463:3055–3071.
- Brocchini, M. and Peregrine, D. H. (1996). Integral flow properties in the swash zone and averaging. *Journal of Fluid Mechanics*, 317:241–273.
- Carrier, G. F. (1966). Gravity waves of water of variable depth. *Journal of Fluid Mechanics*, 24:641–659.
- Carrier, G. F. (1990). Tsunami propagation from a finite source. In Brennan, A. M. and Lander, J. F., editors, *Proceedings of the 2nd UJNR Tsunami Workshop*, pages 101–115. National Geophysical Data Center.

- Carrier, G. F. and Greenspan, H. P. (1958). Water waves of finite amplitude on a sloping beach. *Journal of Fluid Mechanics*, 4:97–109.
- Carrier, G. F. and Noiseux, C. F. (1983). The reflection of obliquely incident tsunamis. *Journal of Fluid Mechanics*, 133:147–160.
- Carrier, G. F., Wu, T. T., and Yeh, H. (2003). Tsunami run-up and draw-down on a plane beach. *Journal of Fluid Mechanics*, 475:79–99.
- Carrier, G. F. and Yeh, H. (2005). Tsunami propagation from a finite source. *CMES: Computer Modeling in Engineering and Sciences*, 10(2):113–121.
- Csanady, G. T. (1982). *Circulation in the Coastal Ocean*. D. Reidel Publishing Company.
- Dutykh, D. and Dias, F. (2007). Water waves generated by a moving bottom. In Kundu, A., editor, *Tsunami and Nonlinear Waves*, pages 63–94. Springer.
- Fritz, H. M., Kongko, W., Moore, A., McAdoo, B., Goff, J., Harbitz, C., Uslu, B., Kalligeris, N., Suteja, D., Kalsum, K., Titov, V., Gusman, A., Latifet, H., Santoso, E., Sujoko, S., Djulkarnaen, D., H., S., and Synolakis, C. E. (2007). Extreme runup from the 17 July 2006 Java tsunami. *Geophysical Research Letters*, 34:L12602.
- Gelb, A., Gottlieb, D., and Paldor, N. (1997). Wind set-down relaxation on a sloping beach. *Journal of Computational Physics*, 138:644–664.
- González, F. I., Satake, K., Boss, E. F., and Mofjeld, H. O. (1995). Edge wave and non-trapped modes of the 25 April 1992 Cape-Mendocino tsunami. *Pure and Applied Geophysics*, 144:409–426.
- Gusiakov, V. K. (2009). Chapter 2, Tsunami History: Recorded. In Bernard, E. N. and Robinson, A. R., editors, *The Sea, Volume 15: Tsunamis*, pages 23–53. Harvard University Press.
- Gustafsson, B. and Kreiss, H. O. (1979). Boundary conditions for time dependent problems with an artificial boundary. *Journal of Computational Physics*, 30:333–351.

- Hall, J. V. and Watts, J. W. (1953). Laboratory investigation of the vertical rise of solitary waves on impermeable slopes. Tech. Memo. 33, Beach Erosion Board, USACE.
- Kânoğlu, U. (1998). *The runup of long waves around piecewise linear bathymetries*. PhD thesis, University of Southern California.
- Kânoğlu, U. (2004). Nonlinear evolution and runup-rundown of long waves over a sloping beach. *Journal of Fluid Mechanics*, 513:363–372.
- Kânoğlu, U. and Synolakis, C. E. (1998). Long wave runup on piecewise linear topographies. *Journal of Fluid Mechanics*, 374:1–28.
- Kânoğlu, U. and Synolakis, C. E. (2006). Initial value problem solution of nonlinear shallow water-wave equations. *Physical Review Letters*, 97. article no. 148501.
- Kânoğlu, U., Titov, V. V., Aydın, B., Moore, C., Spillane, M., and Synolakis, C. E. Propagation of long waves with finite-crest length over a flat bottom. In preparation.
- Keller, J. B. and Keller, H. B. (1964). Water wave run-up on a beach. ONR Research Report NONR-3828(00), Department of the Navy, Washington, DC.
- Kervella, Y., Dutykh, D., and Dias, F. (2007). Comparison between three-dimensional linear and nonlinear tsunami generation models. *Theoretical and Computational Fluid Dynamics*, 21(4):245–269.
- Koshimura, S., Imamura, F., and Shuto, N. (1999). Propagation of obliquely incident tsunamis on a slope, Part 1: Amplification of tsunamis on a continental slope. *Coastal Engineering Journal*, 41:151–164.
- Liu, P. L.-F., Lynett, P. J., and Synolakis, C. E. (2003). Analytical solutions for forced long waves on a sloping beach. *Journal of Fluid Mechanics*, 478:101–109.
- Lynett, P. J., Borrero, J. C., Liu, P. L.-F., and Synolakis, C. E. (2003). Field survey and numerical simulations: a review of the 1998 Papua New Guinea earthquake and tsunami. *Pure and Applied Geophysics*, 160:2119–2146.



- Marchuk, A. G. and Titov, V. V. (1989). The effect of tsunami focusing. In *Proceedings of IUGG/IOC International Tsunami Symposium*, pages 11–17, Novosibirsk, USSR.
- Nof, D. and Paldor, N. (1992). Are there oceanographic explanations for Israelites' crossing of the Red Sea? *Bulletin of American Meteorological Society*, 73:305–314.
- Okada, Y. (1985). Surface deformation due to shear and tensile faults in a half-space. *Bulletin of Seismological Society of America*, 75:1135–1154.
- Okada, Y. (1992). Internal deformation due to shear and tensile faults in a half-space. *Bulletin of Seismological Society of America*, 82:1018–1040.
- Okal, E. A. (2003a). Normal mode energetics for far-field tsunamis generated by dislocations and landslides. *Pure and Applied Geophysics*, 160:2189–2221.
- Okal, E. A. (2003b). T waves from the 1998 Papua New Guinea earthquake and its aftershocks: timing the tsunamigenic slump. *Pure and Applied Geophysics*, 160:1843–1863.
- Okal, E. A. and Synolakis, C. E. (2004). Source discriminants for nearfield tsunamis. *Geophysical Journal International*, 158(3):899–912.
- Pedersen, G. and Gjevik, B. (1983). Runup of solitary waves. *Journal of Fluid Mechanics*, 135:283–299.
- Peregrine, D. H. (1966). Calculations of the development of an undular bore. *Journal of Fluid Mechanics*, 25:321–330.
- Peregrine, D. H. (1967). Long waves on a beach. *Journal of Fluid Mechanics*, 27:815–827.
- Prichard, D. and Dickinson, L. (2007). The near-shore behaviour of shallow-water waves with localized initial conditions. *Journal of Fluid Mechanics*, 591:413–436.
- Renzi, E. and Sammarco, P. (2010). Landslide tsunamis propagating around a conical island. *Journal of Fluid Mechanics*, 650:251–285.

- Sammarco, P. and Renzi, E. (2008). Landslide tsunamis propagating along a plane beach. *Journal of Fluid Mechanics*, 598:107–119.
- Satake, K. (2007). Tsunamis. In Schubert, G., editor, *Treatise on Geophysics*, volume 4. Elsevier.
- Stein, S. and Okal, E. A. (2005). Speed and size of the Sumatra earthquake. *Nature*, 434:581–582.
- Stoker, J. J. (1948). The formation of breakers and bores. *Communications on Pure and Applied Mathematics*, 1:1–87.
- Synolakis, C. E. (1986). *The runup of long waves*. PhD thesis, California Institute of Technology.
- Synolakis, C. E. (1987). The runup of solitary waves. *Journal of Fluid Mechanics*, 185:523–545.
- Synolakis, C. E., Bardet, J. P., Borrero, J. C., Davies, H. L., Okal, E. A., Silver, E. A., Sweet, S., and Tappin, D. R. (2002). The slump origin of the 1998 Papua New Guinea Tsunami. *Proceedings of the Royal Society of London A*, 458:763–789.
- Synolakis, C. E. and Bernard, E. N. (2006). Tsunami science before and beyond Boxing Day 2004. *Philosophical Transactions of the Royal Society A*, 364:2231–2265.
- Synolakis, C. E., Bernard, E. N., Titov, V. V., Kânoğlu, U., and González, F. I. (2008). Validation and verification of tsunami numerical models. *Pure and Applied Geophysics*, 165(11-12):2197–2228.
- Synolakis, C. E. and Kânoğlu, U. (2009). Chapter 8, Tsunami Modeling: Development of Benchmarked Models. In Bernard, E. N. and Robinson, A. R., editors, *The Sea, Volume 15: Tsunamis*, pages 237–294. Harvard University Press.
- Tadepalli, S. and Synolakis, C. E. (1994). The run-up of *N*-waves on sloping beaches. *Proceedings of the Royal Society of London A*, 445:99–112.
- Tadepalli, S. and Synolakis, C. E. (1996). Model for the leading waves of tsunamis. *Physical Review Letters*, 77:2141–2144.

- Tinti, S. and Tonini, R. (2005). Analytical evolution of tsunamis induced by near-shore earthquakes on a constant-slope ocean. *Journal of Fluid Mechanics*, 535:33–64.
- Titov, V. V. (1997). *Numerical modeling of long wave runup*. PhD thesis, University of Southern California.
- Titov, V. V., Rabinovich, A. B., Mofjeld, H. O., Thomson, R. E., and González, F. I. (2005). The global reach of the 26 December 2004 Sumatra tsunami. *Science*, 309:2045–2048.
- Titov, V. V. and Synolakis, C. E. (1995). Modeling of breaking and nonbreaking long-wave evolution and runup using VTCS-2. *Journal of Waterways, Port, Coastal and Ocean Engineering, ASCE*, 121(6):308–316.
- Titov, V. V. and Synolakis, C. E. (1996). Numerical modeling of long wave runup using VTCS-3. In Yeh, H., Liu, P. L.-F., and Synolakis, C. E., editors, *Long Wave Runup Models*, pages 242–248. World Scientific.
- Titov, V. V. and Synolakis, C. E. (1998). Numerical modeling of tidal wave runup. *Journal of Waterways, Port, Coastal and Ocean Engineering, ASCE*, 124(4):157–171.
- Todorovska, M. I. and Trifunac, M. D. (2001). Generation of tsunamis by a slowly spreading uplift of the sea-floor. *Soil Dynamics and Earthquake Engineering*, 21:151–167.
- Trifunac, M. D. and Todorovska, M. I. (2002). A note on differences in tsunami source parameters for submarine slides and earthquakes. *Soil Dynamics and Earthquake Engineering*, 22:143–155.
- Tuck, E. O. and Hwang, L. S. (1972). Long wave generation on a sloping beach. *Journal of Fluid Mechanics*, 51:449–461.
- Ward, S. N. (2001). Landslide tsunami. *Journal of Geophysical Research*, 106:11201–11215.
- Watson, G. N. (1944). *A Treatise on the Theory of Bessel Functions*. Cambridge University Press.

- Wei, Y., Bernard, E. N., Tang, L., Weiss, R., Titov, V. V., Moore, C., Spillane, M., Hopkins, M., and Kânoğlu, U. (2008). Real-time experimental forecast of the Peruvian tsunami of August 2007 for U.S. coastlines. *Geophysical Research Letters*, 35:L04609.
- Whitham, G. B. (1958). On the propagation of shock waves through regions of nonuniform area of flow. *Journal of Fluid Mechanics*, 4:337–360.
- Wiegel, R. L. (1955). Laboratory studies of gravity waves generated by the movement of a submerged body. *Transactions of AGU*, 36:759–774.

## APPENDIX A

### FOURIER TRANSFORM OF THE FUNCTION $\tanh$

To show that the relation

$$\int_{-\infty}^{\infty} \tanh \gamma x e^{-ikx} dx = -2i \alpha \operatorname{cosech} \alpha k, \quad (\text{A.1})$$

$\alpha = \pi/(2\gamma)$ , holds, the integral on the left-hand side is first splitted into real and imaginary parts as

$$\int_{-\infty}^{\infty} \tanh \gamma x e^{-ikx} dx = \int_{-\infty}^{\infty} \tanh \gamma x \cos kx dx - i \int_{-\infty}^{\infty} \tanh \gamma x \sin kx dx. \quad (\text{A.2})$$

The first integral on the right-hand side vanishes since the integral of an odd function over a symmetric interval is zero. The second integral has an even integrand, hence Eq. (A.2) reduces to

$$\int_{-\infty}^{\infty} \tanh \gamma x e^{-ikx} dx = -2i \int_0^{\infty} \tanh \gamma x \sin kx dx. \quad (\text{A.3})$$

The right-hand side of this equality represents the Fourier sine integral of the function  $\tanh \gamma x$  and it is available in the integral tables, or it can easily be evaluated by using a computer algebra system such as Mathematica.<sup>®</sup> It reads

$$\int_0^{\infty} \tanh \gamma x \sin kx dx = \frac{\pi}{2\gamma} \operatorname{cosech} \frac{\pi}{2\gamma} k, \quad (\text{A.4})$$

under the general condition that  $\operatorname{Re} \gamma > 0$ , which is satisfied for the present problem.

Hence,

$$\int_{-\infty}^{\infty} \tanh \gamma x e^{-ikx} dx = -i \frac{\pi}{\gamma} \operatorname{cosech} \frac{\pi}{2\gamma} k. \quad (\text{A.5})$$

## APPENDIX B

### AN APPROXIMATE SOLUTION FOR THE FORCED NONLINEAR SHALLOW-WATER WAVE EQUATIONS

In this part, an approximate nonlinear analytical solution is developed for calculation of the flow field generated by a volume of mass sliding over a linearly sloping beach. The model is a generalization of the linear analytical solution developed by Liu et al. (2003).

#### B.1 Mathematical Analysis

The surface response resulting from a time-dependent bottom disturbance on a linearly sloping beach can be described by the forced nonlinear shallow-water wave (NSW) equations. The bottom perturbation is implemented into the continuity equation as a forcing term and the subsequent equations are in the form of

$$(\eta - h)_t + \left[ \left( \frac{\tan \beta}{\mu} x - h + \eta \right) u \right]_x = 0, \quad (\text{B.1a})$$

$$u_t + u u_x + \eta_x = 0, \quad (\text{B.1b})$$

where  $\beta$  represents the beach angle with horizontal,  $\mu$  is the slide mass ratio, and  $h(x, t)$  is the time-dependent ocean-floor forcing (Figure B.1). The parameter  $\mu$  represents the ratio of the maximum vertical thickness of the slide to its maximum horizontal extend. Liu et al. (2003) consider slides with  $\mu \ll 1$  so that  $\tan \beta / \mu \sim O(1)$ , as the shallow-water wave theory requires.

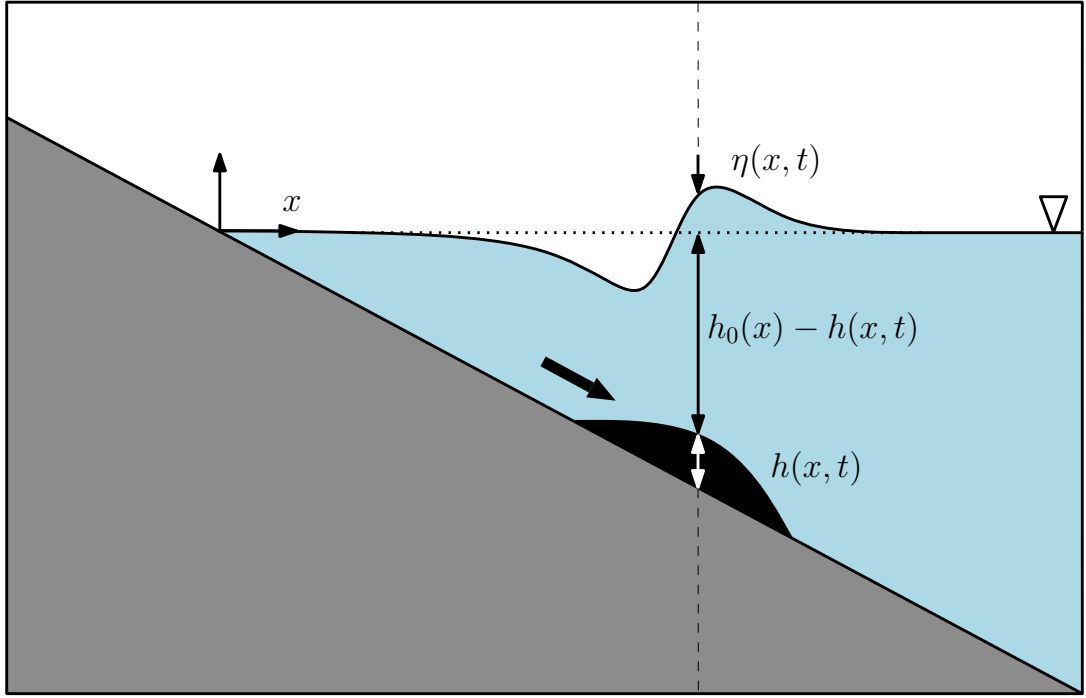


Figure B.1: Definition sketch. The undisturbed water depth is defined to be  $h_0(x) = x \tan \beta / \mu$  and the time-dependent bottom perturbation is represented by  $h(x, t)$ .

An undisturbed initial sea surface and zero initial velocity yield the conditions

$$\eta(x, t = 0) = 0, \quad (\text{B.2a})$$

$$\eta_t(x, t = 0) = -h_t(x, t = 0). \quad (\text{B.2b})$$

Below, a solution of the initial-value problem (IVP) given in Eqs. (B.1)-(B.2) will be attempted through the Carrier-Greenspan (CG) transformation. The transform pair

$$q = \frac{\tan \beta}{\mu} x - h + \eta, \quad (\text{B.3a})$$

$$\lambda = \frac{\tan \beta}{\mu} t - u, \quad (\text{B.3b})$$

is adopted, which transforms Eqs. (B.1) into

$$\eta_\lambda - h_\lambda + (qu)_q + u u_\lambda = 0, \quad (\text{B.4a})$$

$$u_\lambda + u u_q + \eta_q = u_\lambda h_q + u_q h_\lambda, \quad (\text{B.4b})$$

or, in more convenient form,

$$(qu)_q + \left(\frac{u^2}{2} + \eta - h\right)_\lambda = 0, \quad (\text{B.5a})$$

$$u_\lambda + \left(\frac{u^2}{2} + \eta - h\right)_q = -2h_q + u_\lambda h_q + u_q h_\lambda. \quad (\text{B.5b})$$

Further defining

$$\sigma = 2\sqrt{q} = 2\sqrt{\frac{\tan\beta}{\mu}x - h + \eta}, \quad (\text{B.6})$$

Eqs. (B.5) can be rewritten as

$$(\sigma^2 u)_\sigma + 2\sigma\left(\frac{u^2}{2} + \eta - h\right)_\lambda = 0, \quad (\text{B.7a})$$

$$\sigma u_\lambda + 2\left(\frac{u^2}{2} + \eta - h\right)_\sigma = 2(u_\lambda h_\sigma + u_\sigma h_\lambda - h_\sigma). \quad (\text{B.7b})$$

Introducing the potential function

$$\varphi(\sigma, \lambda) = \frac{u^2(\sigma, \lambda)}{2} + \eta(\sigma, \lambda) - h(\sigma, \lambda), \quad (\text{B.8})$$

and denoting

$$f = u_\lambda h_\sigma + u_\sigma h_\lambda, \quad (\text{B.9})$$

Eqs. (B.7) can be written in the form

$$(\sigma^2 u)_\sigma + 2\sigma\varphi_\lambda = 0, \quad (\text{B.10a})$$

$$\sigma u_\lambda + 2\varphi_\sigma = 2(f - h_\sigma). \quad (\text{B.10b})$$

In the present form, Eqs. (B.10) do not have a closed form solution; the unknowns of the problem appear on both sides of Eq. (B.10b). In order to proceed with an analytical solution, the term  $f$  is omitted, leaving

$$(\sigma^2 u)_\sigma + 2\sigma\varphi_\lambda = 0, \quad (\text{B.11a})$$

$$\sigma u_\lambda + 2\varphi_\sigma \approx -2h_\sigma, \quad (\text{B.11b})$$

which is an approximate set of differential equations derived for nonlinear modeling of the subsequent motion of landslide-generated waves.

Eliminating the velocity component  $u$  after cross differentiation, the following second-order linear equation can be obtained;

$$\sigma\varphi_{\lambda\lambda} - (\sigma\varphi_\sigma)_\sigma \approx (\sigma h_\sigma)_\sigma. \quad (\text{B.12})$$

Linearity of the new governing equation allows a solution by standard techniques.

The initial conditions (B.2) transform under Eqs. (B.3) and (B.8) to

$$\varphi(\sigma, \lambda = 0) = -h(\sigma, \lambda = 0), \quad (\text{B.13a})$$

$$\varphi_\lambda(\sigma, \lambda = 0) = 0. \quad (\text{B.13b})$$



To obtain Eqs. (B.13), Eq. (B.8) is first written at  $\lambda = 0$ , since  $t = 0$  corresponds to  $\lambda = 0$  in the absence of initial velocity. Then, the use of

$$\eta_\lambda(\sigma, \lambda = 0) = h_\lambda(\sigma, \lambda = 0), \quad (\text{B.14})$$

obtained from Eq. (B.4a) by substituting  $u(q, \lambda = 0) \equiv 0$ , gives the desired initial conditions in the transform space.

Consequently, the IVP of interest now consists Eqs. (B.12)-(B.13). Since Eq. (B.12) is nonhomogeneous, its particular and homogeneous solutions need to be evaluated separately.

Following Liu et al. (2003), a particular solution of the form

$$\varphi_p(\sigma, \lambda) = -\frac{1}{3}[2h(\sigma, \lambda) + \sigma h_\sigma(\sigma, \lambda)], \quad (\text{B.15})$$

can be identified, provided that  $h_{\sigma\sigma} = h_{\lambda\lambda}$ . In particular, the Gaussian sea-floor deformation defined by

$$h(\sigma, \lambda) = e^{-(\mu/\tan\beta)^2(\sigma-\sigma_0-\lambda)^2}, \quad (\text{B.16})$$

satisfies this condition, and hence serves as a particular solution for Eq. (B.12). In this definition,  $\sigma_0$  is a parameter included to specify the initial location of the slide center ( $\sigma = \sigma_0$  corresponds to  $x = x_0$  in the physical  $(x, t)$ -space). In other words, this parameter allows to locate the slide as a subaerial (partly submerged) or submarine (fully submerged) slide initially. It should be noted here that the solution in Liu et al. (2003) does not include this parameter, i.e., they confine to subaerial landslides, although it is straightforward to add  $x_0$  (initial location of the slide) to their solution.

The homogeneous problem, on the other hand, can be defined as

$$\sigma\varphi_{h,\lambda\lambda} - (\sigma\varphi_{h,\sigma})_\sigma = 0, \quad (\text{B.17})$$

subject to

$$\varphi_h(\sigma, \lambda = 0) = -h(\sigma, \lambda = 0) - \varphi_p(\sigma, \lambda = 0), \quad (\text{B.18a})$$

$$\varphi_{h,\lambda}(\sigma, \lambda = 0) = -\varphi_{p,\lambda}(\sigma, \lambda = 0), \quad (\text{B.18b})$$

where  $\varphi(\sigma, \lambda) = \varphi_h(\sigma, \lambda) + \varphi_p(\sigma, \lambda)$ . Eqs. (B.18) are obtained from Eqs. (B.13) by substituting  $\varphi = \varphi_h + \varphi_p$ .

Introducing the Hankel transform,

$$\bar{\varphi}_h(\omega, \lambda) = \int_0^\infty \sigma J_0(\omega\sigma) \varphi_h(\sigma, \lambda) d\sigma, \quad (\text{B.19})$$

Eq. (B.17) transforms to

$$\bar{\varphi}_{h,\lambda\lambda} + \omega^2 \bar{\varphi}_h = 0, \quad (\text{B.20})$$

which has the general solution

$$\bar{\varphi}_h(\omega, \lambda) = \bar{A}(\omega) \cos(\omega\lambda) + \bar{B}(\omega) \sin(\omega\lambda). \quad (\text{B.21})$$

The coefficients  $\bar{A}(\omega)$  and  $\bar{B}(\omega)$  will be determined from the initial conditions (B.18a) and (B.18b), respectively. Eq. (B.18a) yields

$$\bar{A}(\omega) = - \int_0^\infty s J_0(\omega s) [h(s, \lambda = 0) + \varphi_p(s, \lambda = 0)] ds, \quad (\text{B.22})$$

and Eq. (B.18b) yields

$$\bar{B}(\omega) = -\frac{1}{\omega} \int_0^\infty s J_0(\omega s) \varphi_{p,\lambda}(s, \lambda = 0) ds. \quad (\text{B.23})$$

The complete solution of the problem (B.12)-(B.13) in the hodograph space then becomes

$$\begin{aligned} \varphi(\sigma, \lambda) &= \varphi_p(\sigma, \lambda) + \varphi_h(\sigma, \lambda) \\ &= \varphi_p(\sigma, \lambda) + \int_0^\infty \omega J_0(\omega\sigma) \bar{\varphi}_h(\omega, \lambda) d\omega, \end{aligned} \quad (\text{B.24})$$

after inverting the Hankel transform.

The velocity component  $u(\sigma, \lambda)$  is evaluated from Eq. (B.11a). Integrating with respect to  $\sigma$  and differentiating with respect to  $\lambda$ ,

$$u(\sigma, \lambda) = \frac{2}{3} h_\lambda(\sigma, \lambda) + \frac{2}{\sigma} \int_0^\infty \omega J_1(\omega\sigma) [\bar{A}(\omega) \sin(\omega\lambda) - \bar{B}(\omega) \cos(\omega\lambda)] d\omega. \quad (\text{B.25})$$

After obtaining  $\varphi$  and  $u$ , the free-surface elevation  $\eta$  can be calculated from Eq. (B.8) as

$$\eta = \varphi + h - \frac{u^2}{2}, \quad (\text{B.26})$$

and the corresponding physical coordinates can be given by inverting Eqs. (B.3) for  $(x, t)$ ;

$$x = \frac{\mu}{\tan\beta} \left( \frac{\sigma^2}{4} + h - \eta \right), \quad (\text{B.27a})$$

$$t = \frac{\mu}{\tan\beta} (\lambda + u). \quad (\text{B.27b})$$

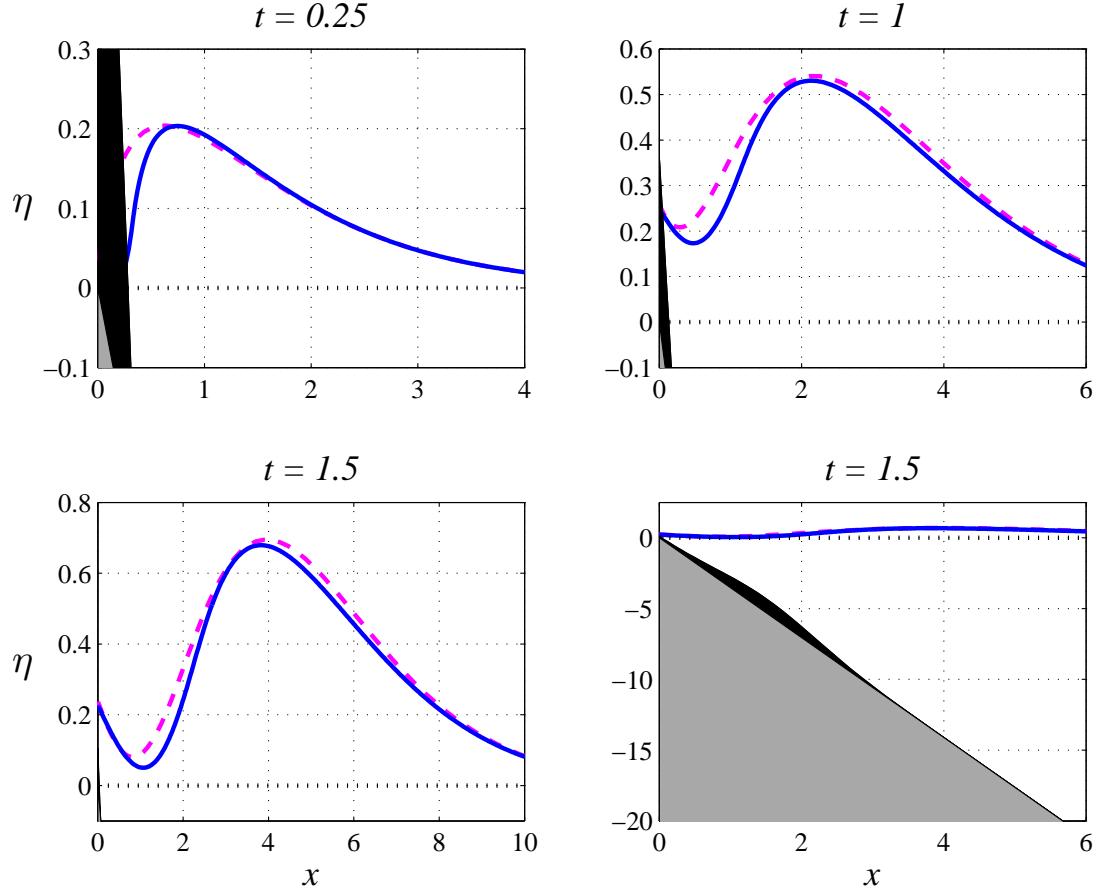


Figure B.2: Spatial distribution of the free-surface for  $\beta = 10^\circ$ ,  $\mu = 0.05$ , ( $\tan\beta/\mu = 3.53$ ). Solid lines show the approximate nonlinear model results while dashed lines show the linear analytical solution of Liu et al. (2003). Black and gray regions represent the sliding mass and the sloping beach, respectively, and dots represent the undisturbed water level.

As described in Chapters 2 and 3, spatial distribution at  $t = t^*$  or temporal variation at  $x = x^*$  can be computed with the help of the Newton-Raphson iterations.

## B.2 Results and Discussions

A comparison of spatial distribution of water surfaces are presented in Figure B.2 for parameters  $\beta = 10^\circ$  and  $\mu = 0.05$  ( $\tan\beta/\mu = 3.53$ ). Even though the approximate nonlinear analytical solution seems close to the linear solution (see Liu et al. 2003), it allows evaluation of shoreline motion following the shoreline tip unlike the linear so-

lution, i.e., the linear solution does not provide shoreline motion. However, it should be noted that the stability of the nonlinear model highly depends on the geometrical parameters of the problem, i.e., the nonlinear solution can be unstable (multi-valued) for certain values of  $\beta$  and  $\mu$ . Stability issues are experienced in the nonlinear solution even for some of the parameters that the linear solution of Liu et al. (2003) is calculated for. This is resulted since the slide moves with a velocity proportional to the square root of the distance to the shoreline, causing the slide to accelerate unphysically.

### **B.3 Conclusions**

An approximate one-dimensional nonlinear analytical model is developed for long waves propagating over a linearly sloping beach due to time-dependent ocean bottom displacement, which is assumed to be in the form of a Gaussian wave.

The shallow-water wave theory is used together with the Carrier-Greenspan (CG) transformation for the nonlinear analysis of the problem. The two nonlinear equations are combined into a single linear equation ignoring some nonlinear terms, and the resulting nonhomogeneous IVP is analyzed separately for particular and homogeneous solutions. While a particular solution is adopted from the analogous linear problem (Liu et al., 2003), a homogeneous solution is deduced by means of the Hankel integral transform technique. However, the proposed solution is not valid for every parameter set because of the unphysical acceleration of the Gaussian bottom movement. It should be noted that the same problem can also be solved with the methodology presented in Chapter 2 with less computational effort.

## VITA

### PERSONAL INFORMATION

Surname, Name : Aydın, Baran  
Nationality : Turkish (TC)  
Date and Place of Birth : 22 February 1979, Ankara  
Marital Status : Married  
e-mail : barann.aydinn@gmail.com

### EDUCATION

Degree	Institution	Year of Graduation
BS	Hacettepe University, Department of Mathematics	2002
High School	Fatih Sultan Mehmet High School, Ankara	1997

### WORK EXPERIENCE

Year	Place	Enrollment
September 2002 - Present	METU Dept. of Engineering Sciences	Research Assistant
August 2007 - May 2008	Texas A&M University (USA)	Visiting Scholar

### FOREIGN LANGUAGES

English (fluent)

### PUBLICATIONS

#### 1. Journal Papers

1.1. **Aydın, B.** and Kânoğlu, U. *A basic solution for nonlinear shallow-water wave equations*. (In preparation).

1.2. Kânoğlu, U., Titov, V. V., **Aydın, B.**, Moore, C., Spillane, M., and Synolakis, C. E. *Propagation of long waves with finite-crest length over a flat bottom*. (In preparation).

1.3. **Aydın, B.** and Kânoğlu, U. *Wind set-down relaxation*. Computer Modeling in Engineering and Sciences (CMES) **21(2)** 149–155 (2007).

## 2. Conference Proceedings

### 2.1. International Conference Proceedings

2.1.1. **Aydın, B.** and Kânoğlu, U. *A new analytical solution for nonlinear shallow-water wave equations*. International Union of Geodesy and Geophysics (IUGG) XXV General Assembly, 28 June–7 July 2011, Melbourne, Australia.

2.1.2. Kânoğlu, U., Kalligeris, N., Flouri, E., Dougalis, V., **Aydın, B.**, Yalçiner, A. C., and Synolakis, C. E. *Preliminary modeling of tsunami generation, propagation, and inundation in the Aegean Sea*. International Union of Geodesy and Geophysics (IUGG) XXV General Assembly, 28 June–7 July 2011, Melbourne, Australia.

2.1.3. Spillane, M., Titov, V. V., Moore, C., **Aydın, B.**, Kânoğlu, U., and Synolakis, C. E. *Tsunami focusing*. American Geophysical Union (AGU) 2010 Fall Meeting, 13–17 December 2010, San Francisco, California, USA.

2.1.4. Moore, C., Şen, C., **Aydın, B.**, Tang, L., Titov, V. V., and Kânoğlu, U. *Assessing the source of the 2010 Chilean tsunami using DART data*. American Geophysical Union (AGU) 2010 Fall Meeting, 13–17 December 2010, San Francisco, California, USA.

2.1.5. **Aydın, B.**, Kânoğlu, U., and Synolakis, C. E. *Nonlinear analytical solution for landslide generated tsunamis*. American Geophysical Union (AGU) 2010 Fall Meeting, 13–17 December 2010, San Francisco, California, USA.

2.1.6. Kânoğlu, U., Titov, V. V., **Aydın, B.**, and Synolakis, C. E. *Propagation of finite strip sources over a flat bottom*. 24<sup>th</sup> International Tsunami Symposium, 14–17 July 2009, Novosibirsk, Russia.

2.1.7. Kânoğlu, U., Titov, V. V., **Aydın, B.**, and Synolakis, C. E. *Analytical solution for long wave directivity*. International Union of Geodesy and Geophysics (IUGG) XXIV General Assembly, 2–13 July 2007, Perugia, Italy.

2.1.8. **Aydın, B.** and Kânoğlu, U. *Analytical solution for wind set-down relaxation problem*. Mathematical Methods in Engineering, International Symposium, 27–29 April 2006, Çankaya University, Ankara, Turkey.

## 2.2. National Conference Proceedings

2.2.1. **Aydın, B.** and Kânoğlu, U. *Ege Denizi'nde tsunami oluşumu, yayılımı ve kıyı tırmanmasının modellenmesi*. 7. Kıyı Mühendisliği Sempozyumu, 21–23 Kasım 2011, Trabzon (Submitted).

2.2.2. **Aydın, B.** and Kânoğlu, U. *Sabit eğimli bir kıyıdaki dalga tırmanmasının özfonksiyon açılımı ile analizi*. XVII. Ulusal Mekanik Kongresi, 5–9 Eylül 2011, Elazığ (Accepted).

2.2.3. **Aydın, B.** and Kânoğlu, U. *Sabit derinlikli basen üzerinde sonlu uzunluktaki tsunami dalgasının analitik modellenmesi*. XVI. Ulusal Mekanik Kongresi, 22–26 Haziran 2009, Kayseri.